University of Alberta

Block Copolymer Templated Patterning of Silicon Surfaces and their Applications

by

Yinghong Qiao

A thesis submitted to the Faculty of Graduate Studies and Research
in partial fulfillment of the requirements for the degree of

Doctor of Philosophy

Department of Chemistry

Edmonton, Alberta
Fall 2008

Library and
Archives Canada

Published Heritage
Branch

395 Wellington Street
Ottawa ON K1A 0N4
Canada

Bibliothèque et
Archives Canada

Direction du
Patrimoine de l'édition

395, rue Wellington
Ottawa ON K1A 0N4
Canada

Your file Votre référence
ISBN: 978-0-494-46406-9
Our file Notre référence
ISBN: 978-0-494-46406-9

NOTICE:
The author has granted a non-exclusive license allowing Library and Archives Canada to reproduce, publish, archive, preserve, conserve, communicate to the public by telecommunication or on the Internet, loan, distribute and sell theses worldwide, for commercial or non-commercial purposes, in microform, paper, electronic and/or any other formats.

The author retains copyright ownership and moral rights in this thesis. Neither the thesis nor substantial extracts from it may be printed or otherwise reproduced without the author's permission.

AVIS:
L'auteur a accordé une licence non exclusive permettant à la Bibliothèque et Archives Canada de reproduire, publier, archiver, sauvegarder, conserver, transmettre au public par télécommunication ou par l'Internet, prêter, distribuer et vendre des thèses partout dans le monde, à des fins commerciales ou autres, sur support microforme, papier, électronique et/ou autres formats.

L'auteur conserve la propriété du droit d'auteur et des droits moraux qui protège cette thèse. Ni la thèse ni des extraits substantiels de celle-ci ne doivent être imprimés ou autrement reproduits sans son autorisation.

In compliance with the Canadian Privacy Act some supporting forms may have been removed from this thesis.

While these forms may be included in the document page count, their removal does not represent any loss of content from the thesis.

Conformément à la loi canadienne sur la protection de la vie privée, quelques formulaires secondaires ont été enlevés de cette thèse.

Bien que ces formulaires aient inclus dans la pagination, il n'y aura aucun contenu manquant.

Canada

For Dong and Si-Ning

Abstract

The use of self-assembled polymer structures to direct the formation of mesoscopic (1-100 nm) features on silicon could provide a fabrication-compatible means to produce nanoscale patterns on silicon, supplementing conventional lithographic techniques. In the beginning of this thesis, we demonstrate nanoscale etching of silicon, using standard aqueous-based fluoride etchants, to produce three dimensional nanoscale features. The amphiphilic block copolymers, polystyrene-*block*-poly(4-vinyl pyridine), denoted as PS-*b*-P4VP with different molecular weights, serve to direct the silicon surface chemistry by controlling the spatial location of the reaction, as well as concentration of reagents. Controllable shapes, sizes, average spacing, and chemical functionalities of the patterned nanostructures are obtained through the modulation of the experimental conditions, such as crystallographic orientation of the used silicon wafer, concentration of the etchant, etching time, and *et al*. This etching method is not limited exclusively to flat surfaces: patterning on curved surfaces through the same etching recipe is also demonstrated in the thesis.

One unique feature of the patterned silicon surface is that the interiors of etch pits are hydride terminated, while the exteriors of the etched structures remain covered by the native oxide. The interiors of the resulting etch pits can be selectively functionalized with organic monolayers, metal nanoparticles, and other materials, leading to ordered arrays on silicon. In the second part of this thesis, we demonstrate the construction of metal nanoparticle arrays with a controlled spatial distribution on surfaces, utilizing both galvanic displacement and hydrosilylation reactions on hydride-terminated silicon

surfaces by taking advantage of the distinct functionalities between the etch pit interior and the flat top surface, hydride versus oxide.

As one of many possibilities, we also demonstrate in this thesis the fabrication of ordered arrays of gold nanoparticle aggregations on this nanopatterned surface. The interiors of etch pits are functionalized with an α,ω-mercaptoalkene to "capture" gold colloids into the etch pits. Due to the spatial restriction of the etch pits, controlled aggregation behaviours were achieved for nanoparticles of different sizes. The nanoparticle arrays display aggregation-dependent surface enhanced Raman scattering effects. The nanoparticle arrays with controllable aggregations are expected to be useful for trace biological and chemical analysis.

Acknowledgements

There are so many people I would like to thank for a huge variety of reasons. First and foremost, is my supervisor Dr. Jillian M. Buriak. With her enthusiasm, her passion, her inspiration, and her huge efforts to explain things clearly and simply, she helped to make chemistry fun and interesting for me. She was always available to help me out from the research frustration. She could not even realize how much I have learned from her. I would never have finished this dissertation without her knowledge, perceptiveness, encouragement and support. Besides of being an excellent supervisor, Jillian is also as close as a good friend to me. It was a lot of fun to talk life, family, and the future with her. I also appreciate for the excellent example she has provided as a successful woman chemist and professor. Her dedication and enthusiasm of doing good science will continue to be a great motivation for my career.

I would like to thank all other members of my Ph. D. committee who took efforts in reading the thesis and providing me with valuable comments and insightful questions on this dissertation: Prof. Steven Bergens (Chemistry), Dr. Martin Cowie (Chemistry), Dr. Jed Harrison (Chemistry), Dr. Michael Brett (Electrical and Computer Engineering), and Dr. Michael O. Wolf (External Examiner, UBC).

I am very fortunate to work in the Buriak group. The Buriak group is a source of friendships as well as scientific support and collaboration. I am very grateful to my good friend and colleague Jennifer Bruce who worked on the synthesis of α,ω-mercaptoalkene which is a critical compound in my SERS project. Thanks for her hard work, I was able to smoothly complete the project in Chapter 4. I also want to express my great thanks to

Dr. Masato Aizawa, Yunhui Li, Xiangning Fan, and Yuan Gao for their support and helpful advice in my research, as well as invaluable friendship. I would also like to acknowledge the people who spent their precious time to correct grammar mistakes in my dissertation and suggest valuable improvements: Dr. Brian Daly, Dr. Anastasia Elias, Dr. David Rider, and Dr. Vincent Wright. I thank you all. I am also very grateful to other past and present group members that I have had the pleasure to work with in the Buriak Group are Steven Chai, Anne Cooper, Nicole Dehm, Dr. Kenneth Harris, Dr. Sang Sub Kim, Sean McClure, Hidenori Mizuno, Dr. Kavithaa Loganathan, Sayed Nagy, Greg Nilsson, Kyle Park, Jie Ru, Xiao Xing, Dr. Lina Xu, Xiaojiang Zhang, and Dr. Jiguang Zhang.

Last, but not least, I am forever indebted to my beloved husband Dong for his love, endless patience, encouragement, and understanding. All I can say is that words can't describe my gratitude to him. He is not only my husband, but also my best friend in my life and my closest co-worker. He took every responsibility and did everything he can to take care of me. I would not be able to finish this dissertation without his unselfish and consistent support from work and life. I owe my every achievement to him. One of the best experiences we lived through during this period is the birth of our lovely daughter Si-Ning Emma Wang. She is the best thing that has ever happened to us in our life.

Table of Contents

Chapter 1 Nanoscale Surface Patterning by Block Copolymer Nanolithography 1

1.1 Introduction..... 1

1.2 Review of Nanopatterning Techniques..... 3

1.2.1 Electron Beam Lithography.....3

1.2.2 Scanning Probe Lithography.....4

1.2.3 Soft Lithography 6

1.3 Block Copolymer Nanolithography..... 8

1.3.1 Introduction.....8

1.3.2 Block Copolymer Template.....12

1.3.3 Nanolithography 19

1.4 Applications of Block Copolymer Nanolithography 26

1.5 Scope of the Thesis..... 32

References..... 34

Chapter 2 Block Copolymer Templated Etching on Silicon.....41

2.1 Introduction..... 41

2.2 Results and Discussion 44

2.2.1 Geometric Shape Control of the Etch pits on Silicon Surfaces of Different Orientations.....46

2.2.2 Effect of Etching Time and Etchant Concentration.....51

2.2.3 Inter-distance Control of Etch Pits.....60

2.2.4 Effect of Silicon Doping 62

2.2.5 Nanopattern on Curved Surfaces 64

2.3 Conclusions 67

2.4 Experimental Section 67

References 70

Chapter 3 Chemical Bifunctionality of Patterned Arrays of Nanoscale Pits and their Application for Selective Metal Deposition 75

3.1 Introduction 75

3.2 Results and Discussion 76

3.2.1 Fabrication of Ordered Etch Pits 76

3.2.2 Chemical Functionality of Patterned Surface 77

3.2.3 Fabrication of Nanocrystal Arrays from Etch Pits 89

3.3 Conclusions 92

3.4 Experimental Section 92

References 96

Chapter 4 Fabrication of Ordered Nanoparticle Arrays on Silicon and their Surface Enhanced Raman Scattering Applications 100

4.1 Introduction 100

4.2 Results and Discussion 103

4.2.1 Fabrication of Nanoparticle Arrays 103

4.2.2 SERS Effect of Nanoparticle Arrays 109

4.3 Conclusions 120

4.4 Experimental Section 120

References 125

Chapter 5 Conclusions and Future Work 128

References 137

List of Tables

Table 2.1. Film thickness of the block copolymer monolayer 59

Table 4.1. Assignment of Raman vibration modes of 4-ATP in the solid state and on the 30 nm Au nanoparticle array 113

Table 4.2. Assignment of Raman vibration modes of 4-MBA in the solid state and on the 30 nm Au nanoparticle array 115

List of Figures

Figure 1.1. Schematic diagram for the procedure of e-beam lithography. (a) Resist coating. (b) E-beam lithography. (c) Develop. (d) Etching. (e) Resist removing (lift-off). 4

Figure 1.2. Schematic diagram for dip-pen nanolithography. 5

Figure 1.3. Schematic diagram for soft lithography procedure. (a) Master. (b) Pouring PDMS precursor on the master. (c) Curing and peeling off of the PDMS stamp. (d) Applying inking solution on the stamp. (e) Ink loaded stamp. (f) Making conformal contact of stamp with substrate. (g) Patterned ink molecules on the substrate. 7

Figure 1.4. Mean-field phase diagram for conformationally symmetric diblock copolymer melts. Phases are labeled L (lamellar), H (hexagonal cylinders), $Q_{la\bar{3}d}$ (bicontinuous cubic), $Q_{lm\bar{3}m}$ (bcc spheres), CPS (close-packed spheres), and DIS (disordered). 9

Figure 1.5. Schematic diagram for the block copolymer nanolithography. (A) Schematic of PS-*b*-PB template for nanolithography. (B) and (C) Schematic of the processing flow to produce holes and dots in silicon nitride, respectively. 11

Figure 1.6. (a,b) Tapping-mode SFM phase images of thin SBS films on Si substrates after annealing in chloroform vapour. Contour lines are superimposed to indicate the domain boundaries. (c) Schematic height profile of the phase images shown in (a,b). (d) Simulated film structures of the *ABA* block copolymer with different film thickness. 13

Figure 1.7. SEM top (A) and side view (B) of PS-*b*-PMMA film orientated perpendicularly to the surface. 14

Figure 1.8. Scanning force micrographs of Fe/Si ceramic lines on a silicon substrate obtained by deposition of polyferrocene copolymer cylindrical micelles into pre-patterned grooves followed by lift-off and hydrogen plasma treatment. 16

Figure 1.9. AFM phase image of a PS-*b*-PEO film spin coated on Si (A) and after benzene vapour annealing (B). 17

Figure 1.10. Scanning electron micrographs of annealed and plasma-treated PS-*b*-PFS films on lithographically defined nanochannels with different width. (a) 500-nm-wide, (b) 320-nm-wide, (c) 240-nm-wide. The inset in (c) is the Fourier transform of the plan-view pattern showing six-fold symmetry. 19

Figure 1.11. A schematic representation of high-density nanowire fabrication in a polymer matrix. (A) PMMA cylinders oriented normal to the surface are obtained by annealing under an applied electric field. (B) Selective removal of the minor component affords a nanoporous PS film. (C) Nanowires can be grown in the porous template by electrodeposition. 21

Figure 1.12. AFM images of arrays of nanoparticles prepared from different elements. 23

Figure 1.13. (a) Schematic diagram of the block copolymer template mediated delivery of reagents to semiconductor surfaces (deposition methods 1 and 2). (b) Metal ions are associated with the pyridine groups of P4VP cores, and reduced by electrons from the semiconductor substrate via a galvanic displacement reaction.....25

Figure 1.14. Selective decoration of metal nanoparticles on copolymer templates. (a) Aggregation of as-deposited Au metal into a PS-*b*-PMMA copolymer film. (b) Selective wetting of Au metal to PS domains is achieved by brief annealing. (c) Formation of Au nanochains after repeated deposition and annealing. Large-scale (d) and close-up (e) TEM micrographs of self-assembled Ag nanowires.. 27

Figure 1.15. (a) Schematic process flow for decoupling capacitor fabrication. (b) Top-down SEM image of porous oxide hardmask. (c) SEM image of the capacitor bottom Si electrode.....28

Figure 1.16. Si Nanowire FET array fabrication. (a) Schematic of nanowire array fabrication. (b) SEM of self-aligned PS-*b*-PMMA film of eight periods formed by graphoepitaxy. (c) Completed silicon nanowire array after plasma etch using a self-aligned polymer film as a mask. 29

Figure 1.17. Fabrication process of the cobalt dot array via block copolymer lithography. 31

Figure 2.1. Schematic diagram for the fabrication of the etch pits on a Si(100) surface using PS-*b*-P4VP as the template. (a) The polymer micelles formed in toluene solution were spin-coated onto a native oxide-coated silicon surface, and the micelles spontaneously self-assembled into a quasi-hexagonal close-packed monolayer array on the surface. Next, the polymer thin film-coated silicon shard was dipped into an HF (aq) solution for the designated time. The etch pit array (squares shown here) was obtained after removal of the polymer. (b) Chemical structure of the PS-*b*-P4VP block copolymer. 43

Figure 2.2. Morphology of the copolymer template coated surface after immersion into HF (aq) solution. Top (a) and side (b) view SEM images of PS-*b*-P4VP (M_n=128400-*b*-33500 g/mol)-coated Si(111) surface etched in 0.01% HF (aq) for 40 min, with the polymer left intact; the polymer removal step was omitted. 45

Figure 2.3. Geometric shape evolution of the patterned etch pits on different orientations of single crystalline silicon. Top (a-d) and side (e-h) view SEM images showing the etch pit arrays on silicon. (a+e) etching of Si(100), in 0.01% HF (aq) for 50 min, in air. (b+f) Si(100) etched in Ar sparged 0.01% HF (aq) for 50 min. (c+g) Si(111) etched in Ar sparged 0.01% HF (aq) for 40 min. (d+h) Si(110) etched in Ar sparged 0.01% HF (aq) for 40 min. 48

Figure 2.4. (a-d) Close-up SEM images of the etch pits obtained on silicon with different crystallographic orientations. Scale bar is 20 nm. These images correspond to the SEM images in Figure 2.3a-d. (e-h) top view and (i-l) side view models showing the proposed assignments of the exposed planes of the etch pits. 49

Figure 2.5. Morphologies of the silicon surfaces of different crystallographic orientations, etched by the 56% pyridinium fluoride (aq) for 1 h. (a) SEM image of the etched surface on Si(100). (b) SEM image of the etched surface on Si(111). (c) SEM image of the etched surface on Si(110). (d+e+f) Close up of etch pits on Si(100), Si(111) and Si(110), respectively..... 52

Figure 2.6. SEM images of the etch pits obtained with different concentrations of HF (aq) solutions, keeping etching time constant (10 min). (a-d) SEM images of the etch pits on Si(100). (e-h) SEM images of the etch pits on Si(111). The HF solution concentrations are 10% for (a) and (e), 1% for (b) and (f), 0.1% for (c) and (g), and 0.01 % for (d) and (h). The copolymer used is PS-*b*-P4VP (M_n=128400-*b*-33500 g/mol)..... 53

Figure 2.7. Shape evolution of etch pits with increasing etching time. SEM images of the etch pits on Si(100) obtained at different etching times using PS-*b*-P4VP (M_n=128400-*b*-33500 g/mol) as templates. The etching time from (a-d) is 20 min, 30 min, 40 min and 50 min, respectively. 0.01% HF (aq) solution was used as etchant. 54

Figure 2.8. (a and b) Histogram representation of the width and depth distribution of the etch pits obtained with different etching times on Si(100). 55

Figure 2.9. Shape evolution of etch pits with increasing etching time. SEM images of the etch pits on Si(111) obtained at different etching times using PS-*b*-P4VP (M_n=128400-*b*-33500 g/mol) as templates and 0.01% HF (aq) as etchant. The etching time from (a-d) is 10 min, 20 min, 30 min, and 40 min, respectively. 56

Figure 2.10. AFM height and phase images of a PS-*b*-P4VP (M_n=128400-*b*-33500 g/mol)-coated Si(100) surface before (a-b) and after (c-d) immersion in 0.01% HF (aq) for 10 min without removal of the polymer. Scan area is 1 μm × 1 μm for all images. 58

Figure 2.11. Schematic diagram shows the swelling and inversion process of PS-*b*-P4VP in acidic solution....59

Figure 2.12. Modulation of etch pit periodicity by using block copolymers of different molecular weights. (a-c) AFM height images of PS-*b*-P4VP (x-*b*-y) thin films on a silicon (100) surface, where x and y designate the molecular weights of the PS and P4VP blocks, respectively. (d-f) AFM height images of the corresponding patterned etch pits obtained by etching with 1% HF (aq) for 3 min. Scan areas are 1 μm × 1 μm in all cases. 61

Figure 2.13. P-type silicon (100) with different resistivities etched in 0.01% HF (aq) for 50 min. (a) 6.4 Ω•cm; (b) 0.5 Ω•cm; (c) 0.001 Ω•cm. 63

Figure 2.14. Large scale SEM images of patterned etch pits on Si(100) (a), Si(111) (b), and Si(110) (c). The pattern is obtained using PS-*b*-P4VP (M_n=128400-*b*-33500 g/mol) as templates and 0.01% HF (aq) as etchant for 40 min. 65

Figure 2.15. Patterning the curved silicon wafer edge using block copolymer templated etching process. (a) SEM image of the silicon wafer edge. (b) and (c) SEM images of the etch pits obtained from different site on the silicon (111) wafer edge. PS-*b*-P4VP (M_n=128400-*b*-33500 g/mol) micelles were used as template. The etching time is 10 min. 66

Figure 3.1. Patterned etch pit array on Si(100) obtained using PS-*b*-P4VP (M_n=128400-*b*-33500 g/mol) templated etching. 77

Figure 3.2. GATR-FTIR spectra of etch pit array. (a) Freshly patterned Si surface. (b) After dipping the freshly patterned Si surface into the HF (aq) solution to

remove native oxide layer. (c) After functionalizing the fresh patterned surface through thermal hydrosilylation of 1-octadecyne. 79

Figure 3.3. Schematic diagram of the galvanic displacement reaction of metal on Si surfaces. The standard electrode potentials shown are with respect to normal hydrogen electrode. 81

Figure 3.4. Radical mechanism of thermohydrosilylation of alkene on hydride-terminated silicon surface. 82

Figure 3.5. Schematic diagram of selective metal deposition inside the etch pits. 83

Figure 3.6. SEM image of gold nanoparticles in the etch pit array through a galvanic displacement process. 83

Figure 3.7. Scanning Auger microscopy (SAM) images of Au nanocrystals on the etch pit array obtained by galvanic displacement. (a) SEM image. (b) Si KLL SAM. (c) Au MNN SAM. (d) The overlapping images of (a), (b) and (c). (e+f) SAM line profiles of Si KLL (top) and Au MNN (bottom) along the red line marked in the SEM image (e) shown in (f). The scale bars are 200 nm in (a-d) and 100 nm in (f), respectively.. 85

Figure 3.8. Schematic diagram for the controlled decoration of gold nanoparticles on the flat top surface of the etch pit array. 86

Figure 3.9. SEM image of selective decoration of the flat top surface of the etch pit array with gold nanoparticles. 87

Figure 3.10. Schematic diagram for the formation of gold nanoparticles over the entire etch pit array (on top flat surface and within the pits). 88

Figure 3.11. SEM image of gold nanoparticles decorating the entire etch pit array, following the experiment process outlined in Figure 3.10. 89

Figure 3.12. Gold nanoparticles grown from the etch pit array. 90

Figure 3.13. (a) Schematic diagram for the capture of Ag nanoprisms within the etch pits. (b) SEM image of capture of Ag nanoprisms into an etch pit array functionalized by hydrosilylation with 4-vinyl pyridine. (b) SEM image of the control experiment done on an etch pit array without the modification with 4-vinyl pyridine. 91

Figure 4.1. Schematic diagram for the fabrication of ordered array of nanoparticle aggregations from the etch pit array on silicon surface. (a) Fresh patterned etch pit array. (b) Thermal hydrosilylation of the fresh patterned surface with undec-10-ene-1-thiol. (c) Deposition of single particle per pit. (d) Deposition of several particles per pit. (e) Deposition of group of particles per pit. 104

Figure 4.2. An SEM image of etch pit array on a Si(100). 105

Figure 4.3. (a) Reaction of hydrogen-terminated silicon with mercapto-alkene to generate a thiol terminated surface. (b) High resolution X-ray photoelectron spectrum of a thiol terminated silicon surface showing a S 2s peak. 105

Figure 4.4. SEM images of the aggregations of different size gold colloidal nanoparticles in etch pit array. (a) 20 nm of gold nanoparticles. (b) 30 nm of gold nanoparticles. (c) 40 nm of gold nanoparticles. 107

Figure 4.5. Histograms of the number of nanoparticles per etch pit. (a) 20 nm nanoparticles. (b) 30 nm nanoparticles. (c) 40 nm nanoparticles. 108

Figure 4.6. Raman spectra of 4-ATP collected on the gold nanoparticle arrays. (a) 20 nm, (b) 30 nm, (c) 40 nm. Inset shows the typical aggregation behaviours of gold nanoparticles in etch pit array. Scale bar is 20 nm. 111

Figure 4.7. Raman spectra of 4-ATP (a) and 4-MBA (b) in solid state. The spectra are collected at 785 nm laser excitation. 112

Figure 4.8. Raman spectra of 4-MBA collected on the gold nanoparticle arrays. (a) 20 nm, (b) 30 nm, (c) 40 nm. Inset shows the typical aggregation behaviours of gold nanoparticles in etch pit array. Scale bar is 20 nm. 114

Figure 4.9. SEM images of nanoparticles on Si surfaces modified by 3-aminopropyl triethoxysilane. (a) 20 nm, (b) 30 nm, (c) 40 nm. 118

Figure 4.10. Raman spectra of 4-ATP on nanoparticles decorated Si surfaces in Figure 4.9. (a) 20 nm, (b) 30 nm, (c) 40 nm. 119

Figure 5.1. Block copolymer templated etching on Si using self-assembled PS-*b*-P2VP-*b*-PEO as a template. 132

Figure 5.2. Formation of etch pit array on GaAs using block copolymer templated etching. Scan size: 2 μm ×2 μm (Left) and 1 μm ×1 μm (Right). 133

Figue 5.3. Proposed procedure for the fabrication of a free-standing Si membrane using block copolymer templated etching on silicon-on-insulator (SOI) wafer. (a) Block copolymer PS-*b*-P4VP coated SOI wafer. (b) Dipping the wafer into HF solution. (c) The formation of a perforated Si membrane. 134

List of Abbreviations

AFM	Atomic force microscopy
aq	Aqueous
4-ATP	4-Aminothiophenol
CPU	Central Processing Unit
DPN	Dip-pen nanolithography
EBL	Electron-beam lithography
FET	Field effect transistor
FT-IR	Fourier Transform Infrared Spectroscopy
GATR	Germanium attenuated total reflection
GIXS	Grazing incidence X-ray scattering
HF	Hydrofluoric acid
4-MBA	4-Mercaptobenzoic acid
NIL	Nanoimprint lithography
PDI	Polydispersity index
PDMS	Polydimethylsiloxane
PS-*b*-P2VP	Polystyrene-*block*-poly(2-vinylpyridine)
PS-*b*-P2VP-*b*-PEO	Polystyrene-*block*-poly(2-vinylpyridine)-*block*-poly(ethylene oxide)
PS-*b*-P4VP	Polystyrene-*block*-poly(4-vinylpyridine)
PS-*b*-PAA	Polystyrene-*block*-poly(acrylic acid)
PS-*b*-PB	Polystyrene-*block*-poly(butadiene)
PS-*b*-PEO	Polystyrene-*block*-poly(ethylene oxide)

PS-*b*-PFS	Polystyrene-*block*-polyferrocenyldimethylsilane
PS-*b*-PI	Polystyrene-*block*-isoprene
PS-*b*-PMMA	Polystyrene-*blcok*-poly(methyl methacrylate)
RIE	Reactive ion etching
SAM	Self-assembled monolayer
SAM	Scanning Auger microscopy
SAXS	Small-angle X-ray scattering
SBS	Polystyrene-*block*-polybutadiene-*block*-polystyrene
SEM	Scanning electron microscopy
SERS	Surface enhanced Raman scattering
SOI	Silicon on insulator
SPM	Scanning probe microscopy
STM	Scanning tunnel microscopy
TEM	Transmission electron microscopy
UV	Ultraviolet
XPS	X-ray photoelectron spectroscopy

Chapter 1

Nanoscale Surface Patterning by Block Copolymer Nanolithography

1.1 Introduction

In 1959, Richard P. Feynman innovatively envisioned the possibility to directly manipulate matter at the atomic scale in his famous talk "there is plenty of room at the bottom".[1] Although this is widely regarded as the starting point of nanotechnology, it is only in past twenty years we have seen the booming development of nanoscience and nanotechnology. Broadly defined, nanotechnology is the area of science and engineering that deals with materials with typical dimensions of 1 to 100 nm.[2] The sizes of small aggregates of atoms, molecules, clusters, supramolecular assemblies all fit into this length scale. Due to the ultra small size of nano-objects, they often exhibit unique properties due to the size effects, surface and interface effects, and quantum effects. The development of nanotechnology will provide us the ability to synthesize, image, measure, and manipulate these nano-objects and build-up devices and materials utilizing their unique properties. Nanotechnology is expected to have a huge impact on virtually every sector of our life and society, and at the same time, requires broad input from physics, chemistry, biology and engineering.

The development of nanoscale patterning techniques is one of the fundamental research areas in nanotechnology.[3] Patterning is one of the most important steps in the modern semiconductor device fabrication process. So far, along with the development of

patterning techniques, we have seen the shrinkage of device size and an accompanying increased degree of integration and performance of semiconductor devices for more than 40 years. The latest photolithography technique is able to produce 45 nm patterning in the CPU (Central Processing Unit) fabrication process.[4,5] The persisting expectation for the shrinkage of the device sizes, however, will finally push photolithography to its inherit physical limitation, and the alternative strategies to obtain sub-100 nm patterning features are urgently needed.

In the development of nanopatterning techniques, there are two general approaches: top down and bottom up.[6,7] The top-down route is best represented by the continual extension of well-developed micro-patterning techniques such as photolithography. In photolithography, the geometric pattern is transferred on the substrate by exposing light to a light-sensitive chemical (photoresist, or simply "resist") through a photomask, followed by a series of development, etching, stripping steps to engrave the exposure pattern into the material underneath the photoresist. To overcome the diffraction limit of photolithography, electron-beam, extreme-UV light or hard X-rays are used as "light source" for the lithography.[3,5] The advantages of the top down route are high reproducibility and the ability to obtain complicated structures and orderliness. On the down side, the rapid increase of cost with the concomitant decrease of the pattern feature size and/or the limited productivity imposed by the series of operations is beginning to acutely limit their applicatio

On the other hand, taking advantage of the interactions between nanoscale objects, a bottom up approach relies on the self-organization of nano-objects to obtain desired structures. Highly ordered nanostructures with feature sizes ranging from several

nanometres to one hundred nanometres can be obtained utilizing bottom-up approaches. The main advantage of the bottom-up method is the ability to build up patterns in a parallel way and thus it is very cost-efficient, although it may be overwhelmed when the size and complexity of the pattern increases.

In this chapter, recent advances of patterning techniques for future device fabrication will be reviewed. Both bottom up and top down approaches have seen great progress in the past years. In particular, block-copolymer nanolithography will be discussed in detail. Finally, several examples to illustrate potential applications of patterned nanostructures will be demonstrated.

1.2 Review of Nanopatterning Techniques

1.2.1 Electron Beam Lithography

Electron beam lithography (EBL) is a mask-free patterning technique. The nanoscale pattern is obtained by scanning electron beams over photoresist in a pattern fashion to induce localized chemical reaction and followed by selective removal of exposed or unexposed area.[8] Figure 1.1 shows the typical fabrication process for EBL. As in photolithography, the resist, is first spun coated on the substrate (Figure 1.1a), followed by the introduction of a high energy electron beam over the desired area (Figure 1.1b). The resist undergoes either degradation or crosslinking, depending upon the choice of positive or negative tone resist. After developing in the selective solvent, the desired pattern is obtained on the resist (Figure 1.1c). The pattern can be further transferred down to the substrate (Figure 1.1d) through wet etching or reactive ion

etching (RIE), for instance. Stripping off the extra resist affords the patterned substrate (Figure 1.1e).

EBL is a very powerful technique in nanofabrication with high resolution. Feature sizes down to a couple of nanometres can be routinely obtained. The resolution is typically limited by forward scattering in the photoresist and secondary electrons traveling through the photoresist, rather than the beam size. EBL is also a low throughput process, which limits its applications in a high quality, low volume manufacturing process, such as making masks.

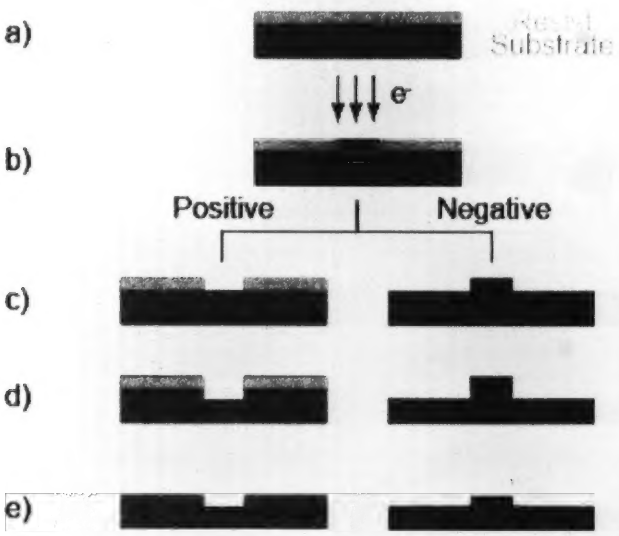

Figure 1.1. Schematic diagram for the procedure of e-beam lithography. (a) Resist coating. (b) E-beam lithography. (c) Develop. (d) Etching. (e) Resist removal.

1.2.2 Scanning Probe Lithography

The invention of scanning probe microscopy (SPM) was a great milestone in nanotechnology development.[9,10] SPM is a family of microscopy techniques that obtain surface images using a sharp tip, typically of nanometer size, by scanning over the

surface. Scanning tunnelling microscopy (STM) and atomic force microscopy (AFM) are two of the most widely used forms of the SPM family. SPM not only provides a great tool to visualize the surface structures with up to atomic resolution, and to study their physical and chemical properties, but also is a powerful lithography tool to build up nanostructures on the surface.

Dip-pen nanolithography (DPN) is a versatile SPM-based lithography technique.[11] In a typical process, the AFM tip inked with the desired molecules is scanned over the surface slowly at controlled atmosphere as shown in Figure 1.2. The molecules on the tip are transferred to the surface over the meniscus connecting the AFM tip and the surface. The patterned nanostructure can be easily visualized with AFM, even with the same tip. DPN technique is compatible with a large family of "ink", such as molecules, supramolecules, biomolecules and a variety of the solid surfaces.[12,13,14] Resolution up to tens of nanometres can be routinely obtained. Due to the advantage of AFM in both "writing" and "reading" of the patterned nanostructures, it is possible to carry out multiple pattern processing with precise registration control.[15]

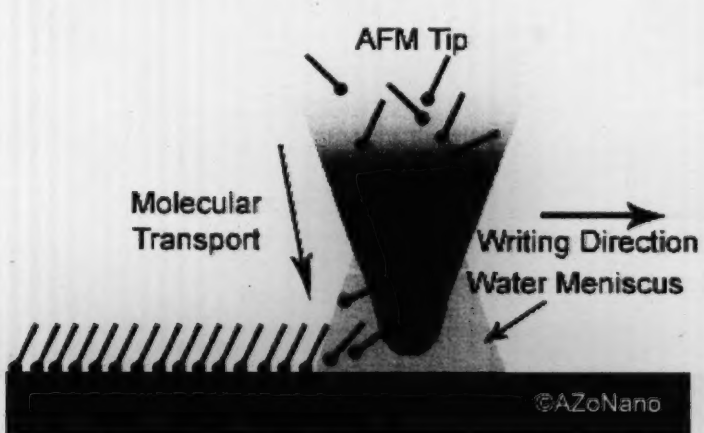

Figure 1.2. Schematic diagram for dip-pen nanolithography.[11]

There are many other SPM based nanolithography techniques.[16, 17] The mechanical force of an AFM tip on a molecule monolayer can be used to mechanically fabricate surface patterns.[18] For example, by engaging the SPM tip into a self-assembled monolayer (SAM) of alkanethiol on a gold surface with increased force, the Au-S bond is destroyed and the alkanethiol molecules are "shaved" away from the SAM in the scanned area. The empty space can then be refilled with other desired molecules to obtain a patterned multi-component SAM. AFM tips can also be used to apply other external stimuli to pattern surfaces. By applying proper bias on the conductive AFM tip, high electric fields between the surface and the tip are formed and this can drive local surface oxidation or reduction reactions to pattern conductive polymers, organic molecules and nanowires on the surface with very high resolution.[19,20]

Similar to EBL, SPM-based nanolithography is also a low-throughput method. To address this issue, a large effort has been put into building up AFM tip arrays to improve their efficiency.[21] Recently, simultaneous DPN patterning using tip arrays with 55000 tips has been demonstrated.[22]

1.2.3 Soft Lithography

Developed by Whitesides and coworkers, soft lithography is a set of patterning techniques utilizing flexible elastomer stamps to fabricate replicate patterns on surfaces.[23, 24] PDMS (polydimethylsiloxane) is the most frequently used elastomer, although other polymer materials have been developed as well. The PDMS stamp fabrication process is shown in Figure 1.3a-d. Firstly, a patterned structure on a solid substrate is used as a master. The PDMS precursor was poured onto the master and then cured at elevated temperatures or by UV irradiation. The PDMS replica of the master

pattern is then peeled off from the master and used as "stamp" for patterning. Shown in Figure 1.3e-g is the schematic of the micro-contact printing technique using the obtained PDMS stamp. In Figure 1.3e, the PDMS stamp is inked with desired molecules, which is then brought into contact with the surface. The ink is then "printed" on the surface only at the area the stamp is contacted. The patterned surface is then subjected to further development and etching steps to obtain the desired nanostructures.

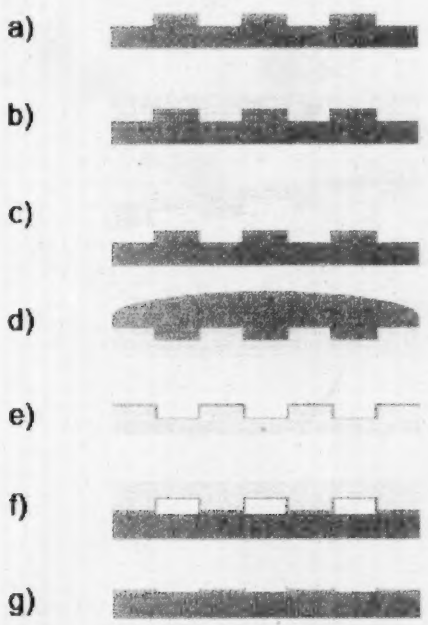

Figure 1.3. Schematic diagram for soft lithography procedure. (a) Master. (b) Pouring PDMS precursor on the master. (c) Curing and peeling off of the PDMS stamp. (d) Applying inking solution on the stamp. (e) Ink loaded stamp. (f) Making conformal contact of stamp with substrate. (g) Patterned ink molecules on the substrate.

Several main advantages of soft lithography technique include: 1) the technique can be applied to pattern non-planar surfaces, because of the flexible nature of the elastomer;[25] 2) the PDMS stamp is cheap and reusable; 3) PDMS is chemically inert and

compatible with a number of chemical and biological species. Soft lithography has a typical resolution limit of ~100 nm, although higher resolution is possible using PDMS of different composition.[26] The drawback of soft lithography also comes from the PDMS itself: PDMS typically shrinks 1% during curing and can swell a bit when adsorbing non-polar solvents, both of which are undesirable for patterning nanostructures requiring high precision.

A recently developed technique related to soft lithography is nanoimprint lithography (NIL).[27] The master is typically made of a hard material such as quartz and is patterned with nanoscale features. The surface of interest is brought into contact with the master using a piezo-controlled step-motor. The feature is transferred by mechanical imprinting. The main advantage of nanoimprint nanolithography is high resolution and high fidelity to the master.

1.3 Block Copolymer Nanolithography

1.3.1 Introduction

Block copolymers are a large class of polymers with two or more polymer blocks connected by a covalent bond. Due to connectivity constraints and the distinct chemical properties of the blocks, block copolymers exhibit interesting self-assembly behaviour in the solid state or in solution phase and have attracted immense attention from both fundamental and application points of view.[28,29] For example, a diblock copolymer solid can display a number of thermodynamically stable equilibrium phase structures such as sphere, cylinder, lamella, and gyroid phases. Figure 1.4 shows a typical phase diagram of

a diblock copolymer modeled using self-consistent mean field theory.[30] The x-axis is the molecular fraction of each block in the polymer and the y-axis is the product of the Flory-Huggis interaction parameter χ, which represents the interaction between two blocks, and the total degree of polymerization N. Similar phase diagrams have been observed experimentally.[31,32] The phase diagram gives very important guidelines for purposely building-up desirable polymer nanostructures for a number of block copolymer templating processes.[33,34,35,36]

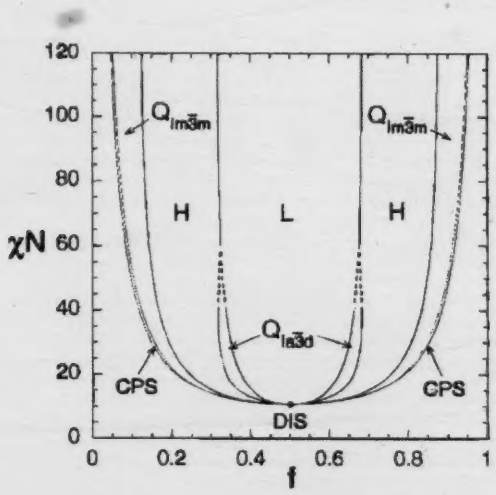

Figure 1.4. Mean-field phase diagram for conformationally symmetric diblock copolymer melts. Phases are labeled L (lamellar), H (hexagonal cylinders), $Q_{la\bar{3}d}$ (bicontinuous cubic), $Q_{lm\bar{3}m}$ (bcc spheres), CPS (close-packed spheres), and DIS (disordered).[30]

The feature sizes of self-assembled block copolymer structures are typically in the range of 10 to 100 nm. These self-assembled nanostructures have been shown to offer huge potential to be used as templates for surface patterning. This patterning strategy is named block copolymer nanolithography. The advantages of block copolymer

nanolithography include highly controllable morphology, versatile chemical structures and properties, compatibility with existing semiconductor fabrication processes, and much more.[37,38,39] Another important feature of the block copolymer nanolithography is that it is a bottom up technique, which is invaluable for scale-up applications.

In 1997, Park and coworkers demonstrated the ability to fabricate an ultrahigh density of periodical arrays of holes and dots using block copolymer nanolithography.[40] A diblock copolymer of polystyrene-*block*-poly-(butadiene) (PS-*b*-PB) was used to generate highly-ordered two-dimensional templates. The PS-*b*-PB film was prepared by spin coating on a silicon nitride substrate from toluene solution. After a thermo-annealing process above the glass transition temperature of both blocks, the polymer spontaneously undergoes micro phase separation due to the incompatible nature of the PS and PB blocks. Depending on the molecular weight and ratio of the two blocks, the copolymer can self-assemble into different morphologies such as two dimensional hexagonal arrays or cylindrical patterns. By appropriately controlling the film thickness, a uniform monolayer of self-assembled microdomains of PB in a PS matrix is obtained. At the air-Si_3N_4 interface, there are continuous wetting layers of PB, as shown in the schematic diagram, Figure 1.5. Two different approaches were adopted to pattern complementary nano-dots or nano-holes on the surface. In the course of producing nano-holes on the surface, the PB block is first selectively degraded and removed through exposure to ozone treatment, which slices the double bond in the butadiene unit. The surface is then subjected to a RIE process to transfer the copolymer pattern to the underlying substrate. In this process, the unreacted PS matrix serves as mask for RIE process and an ordered array of nano-holes on the substrate is produced. In the second

processing technique, the same copolymer self-assembly is used to produce nano-dots on the surface. The polymer template is exposed to an OsO_4 source to selectively stain PB blocks through coordination between Os and double bonds in the PB backbone. Osmium stained PB blocks show reduced propensity to etching in the RIE process, resulting in the formation of negative features on the area where the PS blocks sit. As a result, an ordered nano-dot array is obtained.

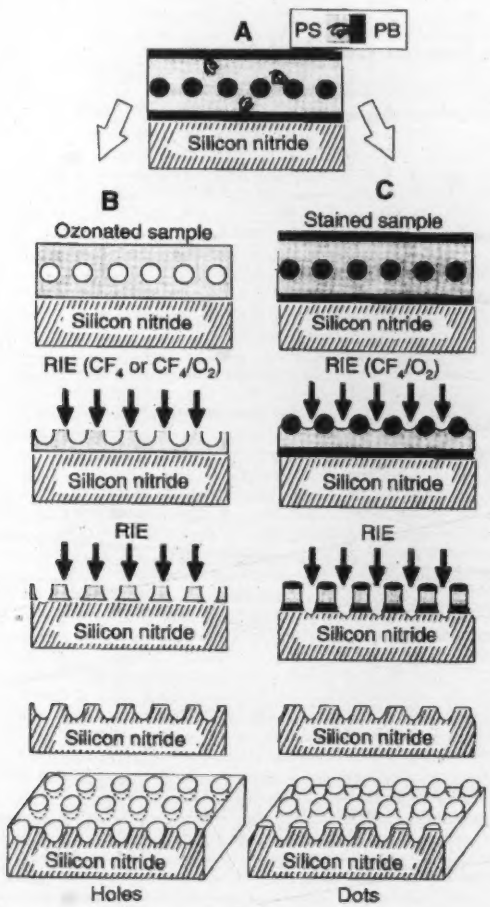

Figure 1.5. Schematic diagram for the block copolymer nanolithography. (A) Schematic of PS-*b*-PB template for nanolithography. (B) and (C) Schematic of the processing flow to produce holes and dots in silicon nitride, respectively.[40]

1.3.2 Block Copolymer Template

Control over the orientation, periodicity, and morphology of polymer self-assembly is a prerequisite for the success of block copolymer nanolithography. Although detailed phase behaviours of copolymers in the solid state are available from polymer physics studies, the structures of copolymer films on the surface exhibit some distinct features, mainly due to surface-polymer interactions.[41,42]

Film thickness is one important parameter determining the morphology of copolymer self-assembly on the surface. Knoll et al studied the phase behaviour of polystyrene-*block*-polybutadiene-*block*-polystyrene (SBS) triblock copolymer films by combining experimental and theoretical approaches.[43] The equilibrium phase of the copolymer in the solid state is a cylindrical phase, with PS as cylinders and PB as a matrix. The film was spin-coated on silicon from a toluene solution, and then subjected to chloroform vapour, which is a non-selective solvent for both blocks, to induce chain movement within the copolymer in order to achieve equilibrium. Figures 1.6a and 1.6b show AFM images of two annealed SBS films of different film thicknesses. After solvent annealing, the film developed discrete terraces with gradually increasing film thicknesses, which are slightly lower or higher than the initial film thickness. Each terrace corresponds to a phase of the copolymer film, which is associated with the specific film thickness of the terrace and shows well-defined microdomain patterns. Different phases are separated by the clear boundaries, as outlined in Figures 1.6a and 1.6b. Figure 1.6c shows the schematic height profile of the terraces and associated phase structures in Figures 1.6a and 1.6b. In the thinner area of Figure 1.6a, a disordered featureless phase is seen. With the increase of the film thickness, the PS cylinders are

orientated perpendicularly to the surface, and appear as bright spots in the AFM phase image. The majority of the surface is covered with the parallel phase, where the PS cylinders orient parallel to the surface, and display as bright strips. Further increases in film thickness result in the formation of perforated PS lamella, *i.e.* PB microdomains, which show up as dark spots in Figure 1.6b, in the continuous PS layer. In thicker films, the same morphological evolution from a perpendicular phase to a parallel phase emerges. The phase behaviour of the copolymer film was further modeled by a dynamic density functional theory approach. The evolution of copolymer surface phase structures with the increase of film thickness is shown in Figure 1.6d, which matches well with the experiment results.

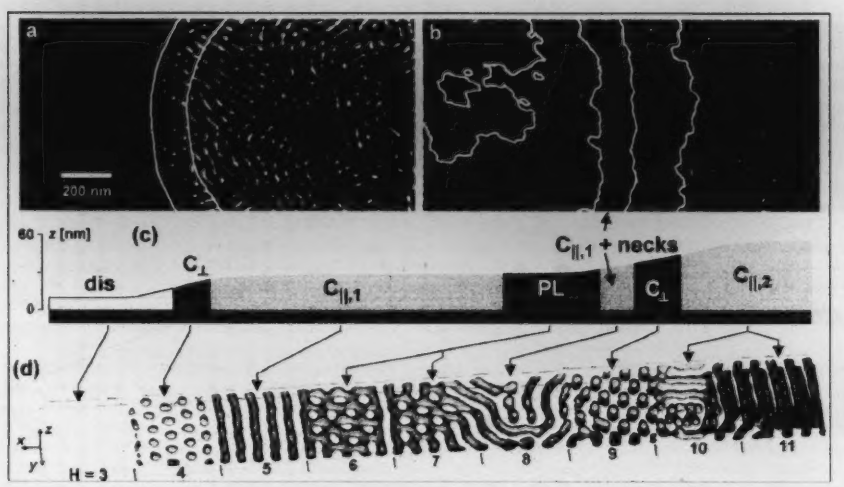

Figure 1.6. (a,b) Tapping-mode SFM phase images of thin SBS films on Si substrates after annealing in chloroform vapour. Contour lines are superimposed to indicate the domain boundaries. (c) Schematic height profile of the phase images shown in (a,b). (d) Simulated film structures of the *ABA* block copolymer with different film thickness.[43]

The chemical properties of the surface are another important factor determining the polymer film self-assembled structure. Russell and coworkers find that the orientation of PS-*b*-PMMA (polystyrene-*block*-poly(methyl methacrylate)) cylindrical microdomains can be controlled by surface modification.[44, 45] Generally, parallel orientation of a copolymer is preferentially seen in polymer films, because of favourable interactions between the surface and one of the components. To remove the preferential interaction, a neutral polymer brush consisting of a random copolymer (PS-r-MMA) of two components of the block copolymer is grafted on the surface. After annealing to achieve the thermodynamic equilibrium state, the block copolymer microdomains orient themselves perpendicularly to the neutralized surface. Figure 1.7 shows typical top and cross-section views of PS-*b*-PMMA films oriented perpendicularly to the surface.[46] The PMMA portion was removed by UV-irradiation followed by rinsing with acetic acid before imaging. The ordered nano-holes in the SEM image correspond to the position of PMMA cylinders. The as-prepared nano-hole arrays could be used as a template for surface patterning processes.

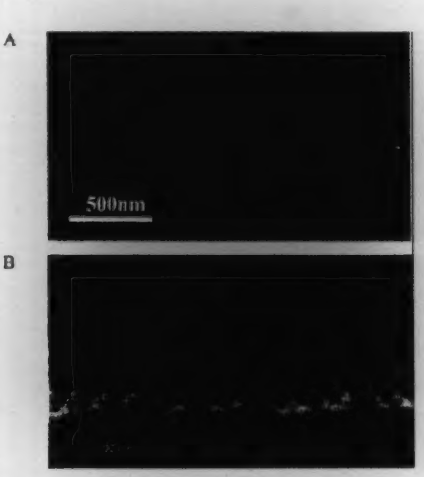

Figure 1.7. SEM top (A) and side view (B) of PS-*b*-PMMA film orientated perpendicularly to the surface.[46]

Block copolymers can organize themselves into interesting nanostructures in the solution phase. A variety of structures, such as micelles, rods, and vesicles, can be obtained through control over choice of solvent, concentration, and others. Transferring the self-assembled aggregates of block copolymers in solution to a substrate provides another very general technique to obtain a template for nanolithography. Spatz and coworkers have developed block copolymer micelle nanolithography to obtain metal particle arrays on solid surfaces from the self-organized micelle arrays.[47, 48, 49] Polystyrene-*block*-poly(2-vinylpyridine) (PS-*b*-P2VP) was used to form the polymer template. When dissolved in toluene, which is a good solvent for PS block and a poor solvent for P2VP block, PS-*b*-P2VP forms micelles in solution with a P2VP core and a PS corona. By spin or dip coating onto the substrate, the micelles can spontaneously self-assemble into a quasi-hexagonal array on the surface. This self-assembled micelle array can serve as the template for nanolithography. For example, an ordered array of metal nanoparticles on the surface can be obtained by applying a plasma treatment to a metal precursor loaded with block copolymer micelles. The periodicity of the micelle array can be controlled by tuning the polymer molecular weight, solvent, micelle solution concentration, spinning-coating rate and other parameters.[50]

This block copolymer micelle nanolithography can be combined with other "top-down" lithography techniques to obtain more sophisticated nanostructures.[51] For example, Massey *et al* demonstrated the fabrication of orientated ceramic lines from organometallic polyferrocene block copolymers.[52] By casting the cylindrical micelle solution of polyferrocene block copolymer onto a surface with an EBL defined nanoscopic line pattern, the alignment of the micelles into the prepatterned channel takes

place as a consequence of capillary effects and steric hinderance. After lifting-off of the resist, followed by a H_2 plasma etching process to remove the copolymer micelles, oriented Fe/Si ceramic lines with structures defined by the nanochannels are revealed, as shown in Figure 1.8.

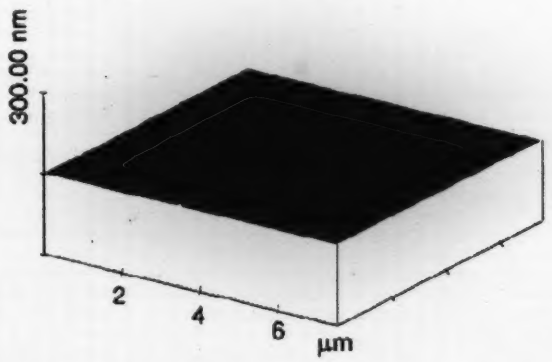

Figure 1.8. Scanning force micrographs of Fe/Si ceramic lines on a silicon substrate obtained by deposition of polyferrocene copolymer cylindrical micelles into pre-patterned grooves followed by lift-off and hydrogen plasma treatment.[52]

One drawback of block copolymer self-assembly is the lack of long-range order, which sets a practical limit of block copolymer nanolithography where high precision and strict registration is required. Much effort has been made to improve the order of block copolymer self-assembly. Solvent annealing and graphoepitaxy are two well developed methods to obtain highly ordered block copolymer self-assembled structures.

Russell and coworkers applied solvent annealing to induce long-range order of polystyrene-*block*-poly(ethylene oxide) (PS-*b*-PEO) self-assembly.[53,54] The polymer film prepared from solution casting represents a frozen non-equilibrium state during solvent evaporation. As shown in Figure 1.9, the film spin-coated from a benzene solution of PS-

b-PEO shows numerous defects. After annealing in benzene vapour for 48 hours, the lateral order of the film is greatly improved and the single domain of ordered assembly extends over several microns. To understand the annealing process, grazing incidence X-ray scattering (GIXS) was employed to track the order of the film during solvent evaporation. The solvent gradient formed during evaporation is proposed to explain the observation of long-range ordered, micro-phase separation during solvent annealing. By choosing the proper solvent, highly ordered phase-separation structures have been obtained in other copolymer self-assemblies.[55,56]

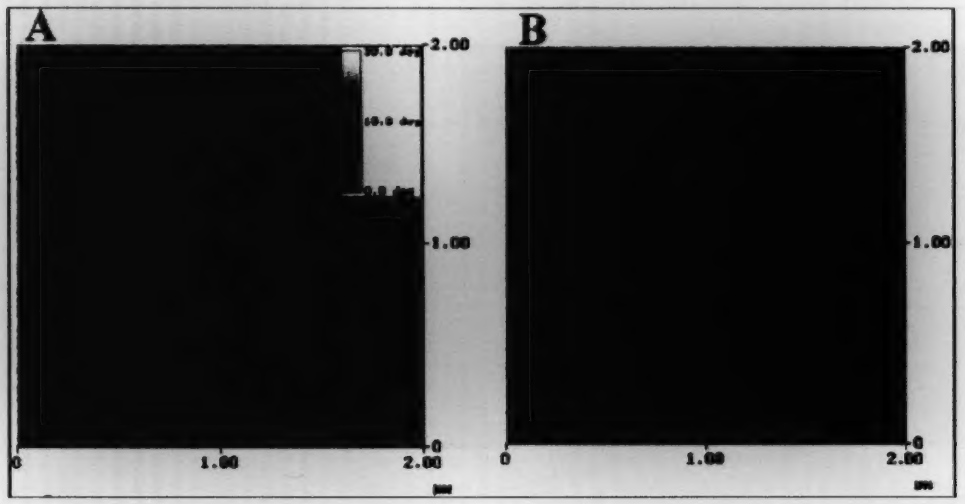

Figure 1.9. AFM phase image of a PS-*b*-PEO film spin coated on Si (A) and after benzene vapour annealing (B).[53]

Graphoepitaxy is another widely used technique to obtain long-range ordered copolymer assembly.[57,58] In graphoepitaxy, the polymer is allowed to organize and assemble in an artificial topographic or chemical surface pattern. The well-defined pattern boundaries can induce the alignment of microdomains and result in the long-range

order of block copolymer films.[59,60] Figure 1.10 shows the improvement of order of PS-*b*-PFS (polystyrene-*block*-polyferrocenyldimethylsilane) microdomains in lithographic-defined channels of different widths.[61] The patterned channels were fabricated by interference lithography on a silica substrate. The block copolymer film was spin coated on the prepatterned surface and annealed to induce the self-assembly process. Finally, an oxygen plasma treatment was applied to the film to remove the PS part and reveal the position of PFS microdomains. In a 500 nm wide channel (Figure 1.9a), the close-packed PFS domains are seen to align into ordered rows near the groove edge. With a continuous decrease of the channel width to 240 nm, the single crystal arrangement of PFS microdomains in the channel was achieved. Results from secondary ion mass spectroscopy and cross sectional SEM reveal that a thin layer of PFS brush wets the silica at the channel edge and bottom. This surface-induced thin layer was believed to induce the alignment of the PFS microdomains rows parallel to the groove edges. When the channel width is small enough and comparable to the grain size of the PS-*b*-PFS assembly, the PFS microdomains arranged into single crystalline arrangement in the channels. The conformal alignment of copolymer microdomains along the channel edges was further supported by the production of point and dislocation defects around the roughness defects along the channel edge.[62] As a result, it is possible to pin the position or tune the periodicity of the copolymer assembly by intentionally introducing small defects along the channel edge. This ability is very important in many potential applications such as high density storage media, photonic waveguides, microfluidics, and many others.

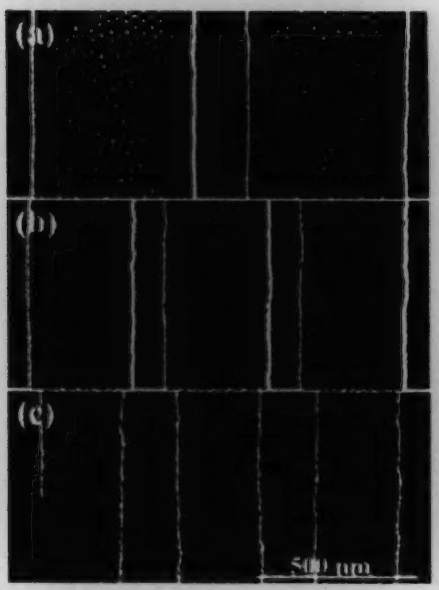

Figure 1.10. Scanning electron micrographs of annealed and plasma-treated PS-*b*-PFS films on lithographically defined nanochannels with different width. (a) 500-nm-wide, (b) 320-nm-wide, (c) 240-nm-wide. The inset in (c) is the Fourier transform of the plan-view pattern showing six-fold symmetry.[61]

1.3.3 Nanolithography

A straightforward way to transfer the ordered copolymer assembly into a useful surface pattern is by using the polymer microdomain as a mask. Due to the similar resistances of copolymer blocks toward reactive ion etching, it is generally necessary to selectively remove one block to produce porous structures to enhance the contrast in the etching process. This step is similar to the development step in photo-lithography processes. PS-*b*-PMMA is a widely used copolymer for nanolithography templating. By carefully adjusting the molecular weight and film thickness, highly ordered vertically orientated PMMA arrays can be obtained on the surface. The different photochemical properties of PS and PMMA blocks are taken advantage of to develop the template.[46]

Under UV irradiation, PMMA undergoes a degradation process via chain scission. On the other hand, a cross linking process, which results in lower solubility, takes place in PS block. Therefore, a brief UV irradiation followed by acetic acid rinsing selectively removes the PMMA block and leaves an array of PS nanoporous structures. As shown previously in Figure 1.7, the locations where the PMMA cylinders had previously resided appear as circular pores. The obtained film can be used as a soft mask for RIE processes, which can transfer the copolymer pattern to the underlying hard substrate, such as SiO_2. The copolymer pattern replica on SiO_2 can serve as a dielectric hard mask for other standard semiconductor process, such as anisotropic RIE, wet etching, to produce ultra small semiconductor devices.[63]

Similar strategies have been applied to other copolymer systems. Harrison et al applied ozone treatment to develop copolymers with unsaturated bonds in the backbone, such as polystyrene-*block*-isoprene, PS-*b*-PI and polystyrene-*block*-butadiene, PS-*b*-PB.[64] It is well-known that the ozone can cleave the carbon-carbon unsaturated bond rapidly. By selectively removing the polydiene blocks through an ozonation process followed by water rinsing, a copolymer template with ordered voids corresponding to the position of polydiene microdomains in PS matrix is obtained. The template can be used for RIE processes to produce desirable nanostructures.

Ordered nanoporous structures can be used as templates for nanowire fabrication.[65] Vertically oriented hexagonal-packed cylinders from PS-*b*-PMMA were obtained by thermoannealing a spin-coated film under an electric field, as shown in Figure 1.11a. A strong dc field (30 to 40 V/μm) was able to induce the alignment of cylinder microdomains parallel to the electric filled lines.[66,67] By removing the minority

cylinder-forming component through a UV-irradiation step (Figure 1.11b) an ordered nanoporous array was formed. Small-angle x-ray scattering (SAXS) measurements confirm the formation of a hexagonally packed nanoporous array normal to the surface. The resulting nanopores were then filled with Co or Cu atoms by electrodeposition. High density magnetic nanowire arrays were obtained, while the morphology of copolymer template was retained. The resulting array shows interesting potential as ultrahigh-density recording media.

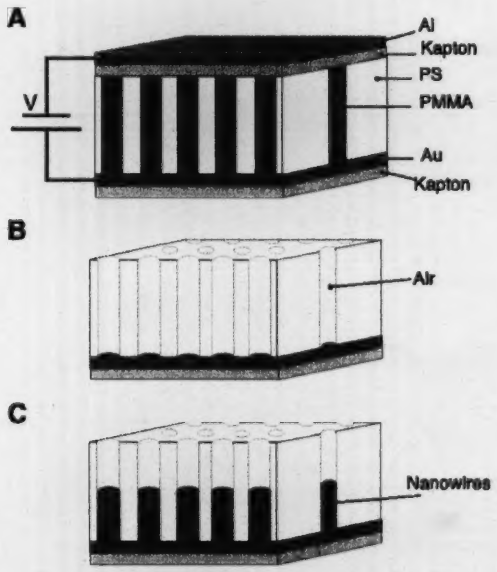

Figure 1.11. A schematic representation of high-density nanowire fabrication in a polymer matrix. (A) PMMA cylinders oriented normal to the surface are obtained by annealing under an applied electric field. (B) Selective removal of the minor component affords a nanoporous PS film. (C) Nanowires can be grown in the porous template by electrodeposition.[65]

So far, we have shown the application of copoplymer nanostructures as "physical" soft mask materials for nanopatterning. On the other hand, copolymer components always have distinct chemical properties that can be utilized. The self-assembly of

copolymer microdomains creates isolated nanoreactor arrays on the surface, which also show great potential in surface nanolithography.

Ordered nanoparticle arrays on surfaces have great promise in electronic, optical, and magnetic applications.[68] Their fabrication, however, remains a big challenge in nanotechnology. Block copolymer micelle nanolithography has been demonstrated to be an effective approach to obtain nanopatterned nanoparticle arrays. Self-assembled PS-*b*-P2VP micelle arrays have been chosen as templates because the nanoparticle precursors can selectively bind to the pyridine group of P2VP block to form metal complexes.[69] In the first step, the diblock copolymer micelles were generated in a toluene solution. The micelle consists of a PS corona and a P2VP core due to the different solubilities of PS and P2VP blocks in toluene. A metal salt, such as $HAuCl_4$ was then added into the micelle solution. The gold precursors are bound only to the polar P2VP blocks through the electrostatic interaction between the protonated pyridine (pyridinium) and the $AuCl_4^-$. After transferring the micelles by dip-coating, an ordered micelle array is spontaneously formed on the substrate. In the second step, hydrogen plasma was applied to reduce the $HAuCl_4$ precursor and simultaneously remove the organic polymer. As a result, ordered nanoparticle arrays with a structure mirroring that of the block copolymer micelles were obtained. Nanoparticle size is controllable through changing the loading ratio of gold precursor to the P2VP block. By choosing different metal precursors, the ordered nanoparticle array of different elements can be obtained in a similar manner, as shown in Figure 1.12.[70] The ordered nanoparticle array can further serve as hard mask for the dry etching process to fabricate other advanced nanostructures.[71] Other block copolymers such as PS-*b*-PEO, PS-*b*-PAA (polystyrene-*block*-poly(acrylic acid)) have also been used

to template the nanoparticle array taking advantage of selective interaction of nanoparticle precursors with one of the copolymer components.[72,73,74] Using a micro-phase separated organometallic copolymer containing suitable precursors can achieve the same result, although the availability of organometallic copolymers is limited.[75,76,77]

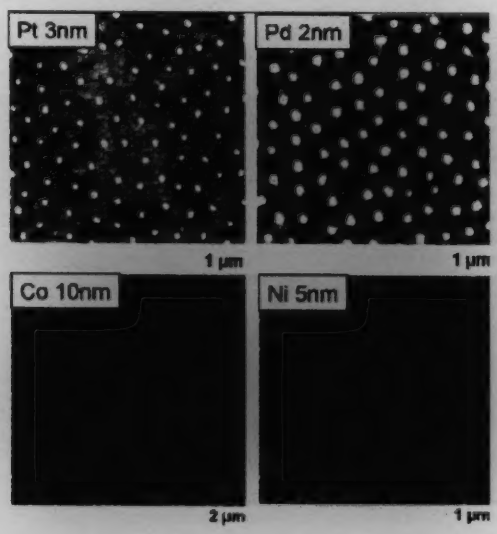

Figure 1.12. AFM images of arrays of nanoparticles prepared from different elements.[70]

Recently, our group has developed block copolymer micelle mediated interfacial chemistry to pattern nanoparticles on surfaces.[78] Two different approaches to obtain ordered nanoparticle arrays on a surface are described in Figure 1.13a. In deposition method 1, the metal precursor was loaded within the block copolymer micelle of PS-*b*-P4VP and an ordered micelle array was obtained upon casting the micelle solution on the substrate. Instead of using plasma to reduce the metal salts as shown in the previous example, an interfacial galvanic displacement reaction was employed to reduce the metal salts. As shown in the schematic diagram Figure 1.13b, the metal precursors associated

with the pyridine group of P4VP blocks were reduced by the electrons from the semiconductor substrate. This spontaneous electroless deposition process was monitored by X-ray photoelectron spectroscopy (XPS). After removing the copolymer template, an ordered nanoparticle array was revealed. In deposition method 2, a semiconductor chip coated with a nanostructured monolayer of a self-assembled block copolymer was immersed into the solution of the metal precursors. The metal salts can selectively diffuse through the polar P4VP cores to the semiconductor interface, where the same galvanic displacement reaction takes place, resulting in the same nanoparticle pattern. The main advantage of the latter method is that the quantity of metal precursors is essentially unlimited and not restricted by the capacity of the block copolymer micelle cores in solution, as is the case with deposition method 1. Thus, better control over the nanoparticle size is achieved by simply tuning the immersing time. The same strategy has been used to pattern multi-component metal nanostructures on surface.[79] In that case, a monolayer of triblock copolymer polystyrene-*block*-poly(2-vinylpyridine)-*block*-poly(ethylene oxide) (PS-*b*-P2VP-*b*-PEO) was used as template. It is found that two blocks, PEO and P2VP, are capable of selective transport of different metal complexes to the surface. For example, the anionic precursors like $HAuCl_4$ prefer to go through P2VP blocks, presumably through the electrostatic interaction, while the co-solvated cationic precursors like Ag^+ tend to go through PEO blocks. As a result, selective deposition of binary metal nanostructures at the desired position can be achieved at the same time.

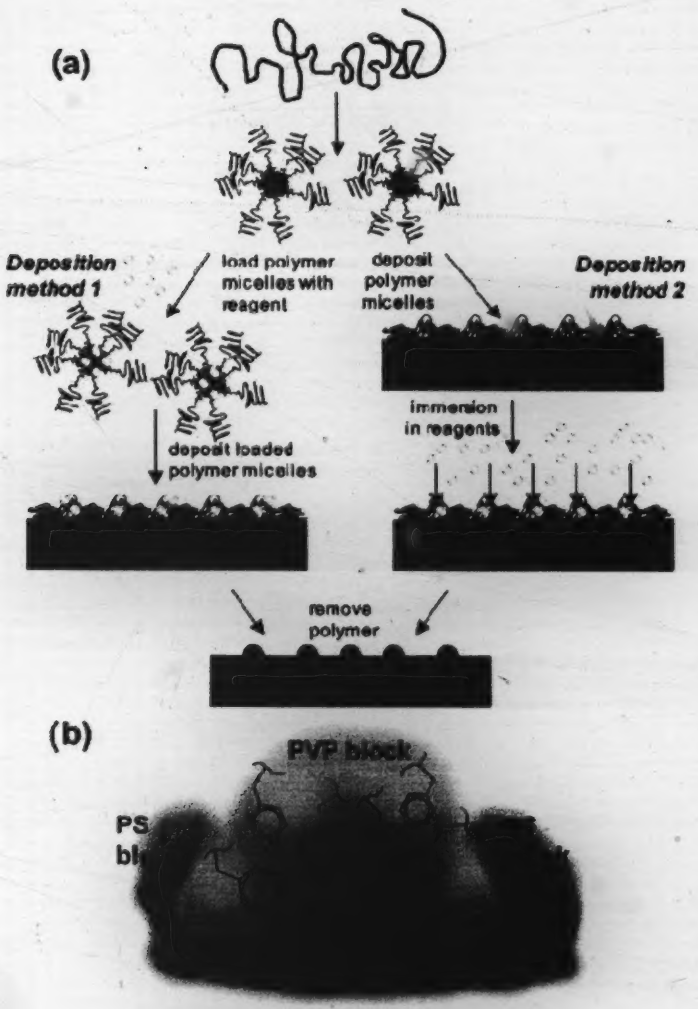

Figure 1.13. (a) Schematic diagram of the block copolymer template mediated delivery of reagents to semiconductor surfaces (deposition methods 1 and 2). (b) Metal ions are associated with the pyridine groups of P4VP cores, and reduced by electrons from the semiconductor substrate via a galvanic displacement reaction.[78]

Another well-exploited way to pattern nanoparticle arrays on surfaces is direct deposition of nanoparticles. Depending on the functional group of the passivation layer on the nanoparticle and surface energy of the copolymer microdomains, selective aggregation of nanoparticles in one of the block copolymer components or at the

interface can take place.[80,81,82] The selective decoration of the polymer template by nanoparticles is also observed when ultrathin metal films are evaporated on cylindrical PS-*b*-PMMA block copolymer films.[83] Figure 1.14a shows SEM images of the copolymer template immediately after evaporation of Au. The selective decoration of the PS block is clearly seen. Selectivity of nearly 100% was achieved by a brief annealing process, as shown in Figure 1.14b. Repeating the evaporation/annealing cycle can significantly increase the loading without destroying the selectivity. The formation of densely packed Au nanoparticle chains in the PS block was clearly visible in Figure 1.14c. On the other hand, Ag exhibits quite interesting behaviour. First, the mobility of Ag nanoparticles on PMMA is so high that selective deposition on PS blocks was achieved without the annealing step. Second, Ag nanoparticles tend to aggregate into continuous nanowires in the PS block upon repeated deposition. As expected, the Au nanochain assembly shows nonlinear current/voltage (I/V) curves due to the existence of single-electron tunnelling between nanometre-sized metal islands. In contrast, electronic transportation measurement over Ag nanowires reveals ohmic character, consistent with the SEM observation. The Monte Carlo simulation was employed to reveal the kinetic mechanism of different aggregation behaviour of Au and Ag in copolymer template.

1.4 Applications of Block Copolymer Nanolithography

One of most important features of block copolymer nanolithography is compatibility with the existing semiconductor processing techniques, which enable the fabrication of a variety of basic device units with potential for electronic, magnetic, and optical applications.

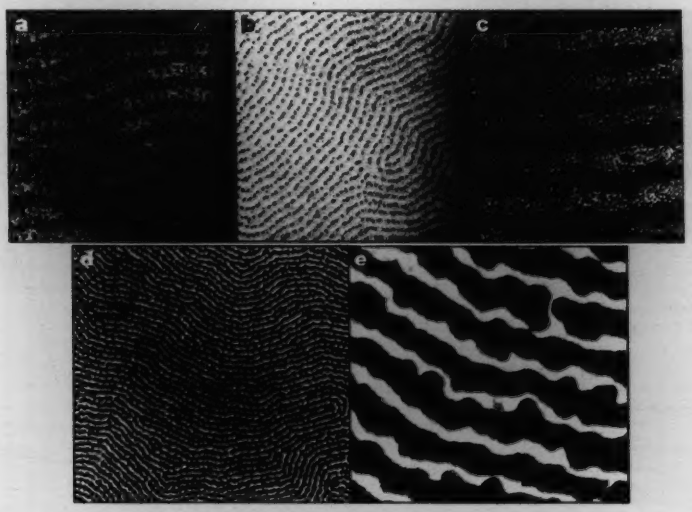

Figure 1.14. Selective decoration of metal nanoparticles on copolymer templates. (a) Aggregation of as-deposited Au metal into a PS-*b*-PMMA copolymer film. (b) Selective wetting of Au metal to PS domains is achieved by brief annealing. (c) Formation of Au nanochains after repeated deposition and annealing. Large-scale (d) and close-up (e) TEM micrographs of self-assembled Ag nanowires.[83]

Black and coworkers have demonstrated the fabrication of high density decoupling capacitors by combining block copolymer nanolithography with the standard nano-fabrication processes.[84,85] Decoupling capacitors are an important device unit in semiconductor devices with the function of minimizing power supply noise. A self-assembled structure of PS-*b*-PMMA was used as a template to define the nanostructure of nanoscale capacitors. Figure 1.15a shows the fabrication process. By adjusting the molecular weight and the film thickness, PS-*b*-PMMA diblock copolymers spontaneously form hexagonally close-packed 20 nm cylindrical PMMA domains on a 40 nm thick PS matrix. The PMMA domains are selectively removed to create PS nanoporous templates; the PS pattern can easily be transferred to the underlying SiO_x layer, followed by removal

of polymer to generate the nanoporous oxide, which then serves as a hard template for Si reactive ion etching to produce a patterned capacitor surface. After stripping the remaining SiO_x hardmask, a thin layer of thermal SiO_2 gate dielectric was grown on the patterned electrode, as shown in Figure 1.15c. Then, a TaN top electrode was conformally deposited onto the SiO_2 gate dielectric by atomic layer deposition to complete the capacitor devices. As expected, the accumulation capacity of the patterned capacitor is 4 times higher than the corresponding planar device over the same lateral area, mainly because of the larger surface area of patterned capacitor.

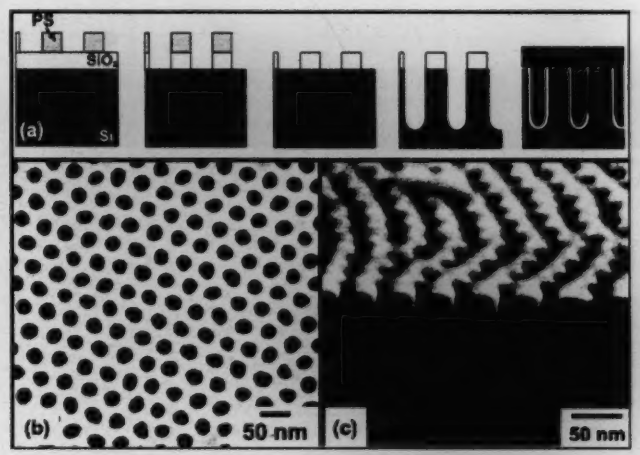

Figure 1.15. (a) Schematic process flow for decoupling capacitor fabrication. (b) Top-down SEM image of porous oxide hardmask. (c) SEM image of the capacitor bottom Si electrode.[84]

The field effect transistor (FET) is the most important device unit in the semiconductor industry. Block copolymer nanolithography provides a cheap solution to pattern sub-50 nm nanowire array FET's.[86] A graphoepitaxy technique was employed to obtain well-defined, aligned, nanowire arrays. Figure 1.16a shows the schematic diagram of the fabrication process. First, a trench pattern with desired width and depth was defined by optical lithography on a silicon on insulator (SOI) wafer. The width and depth

of the trench was tuned so that the cylindrical phase of PS-*b*-PMMA film was aligned with the trench wall. After selectively removing the PMMA blocks by acetic acid, well-aligned PS templates were obtained. The PS template was transferred onto the top silicon layer by a plasma etching process. These lithographically defined Si nanowires can work as an FET array. These prototype FET devices were fabricated by integrating with standard nanofabrication techniques and the device performance was tested. By simply changing the width of trench, devices with different numbers of nanowires were fabricated. A linear relationship between FET drive current and the number of wires comprising the device was revealed, indicating that each wire contributes equally to the device conductance.

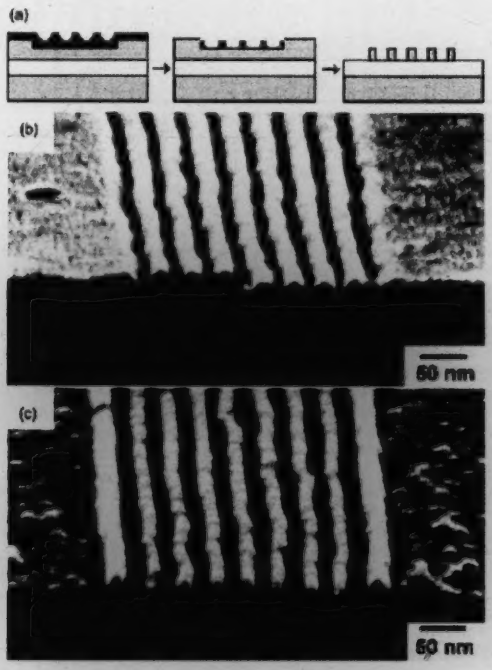

Figure 1.16. Si Nanowire FET array fabrication. (a) Schematic of nanowire array fabrication. (b) SEM of self-aligned PS-*b*-PMMA film of eight periods formed by graphoepitaxy. (c) Completed silicon nanowire array after plasma etch using a self-aligned polymer film as a mask.[86]

Block copolymer nanolithography provides a great technique to obtain nanostructures at the dimension of tens of nanometers, which are desirable for high density data storage. A multi-step process to pattern high density cobalt magnetic particles on a surface was demonstrated using a PS-*b*-PFS block copolymer as a template.[87] By choosing the proper molecular weight and fraction, the PS-*b*-PFS block copolymer self-assembles into a spherical morphology on the surface. One advantage of the PS-*b*-PFS system is that the PFS block is more resistant to oxygen plasma than PS, making it a good mask for pattern transfer. A multilayer structure was designed to transfer the block copolymer pattern to a magnetic layer. The schematic experiment process is summarized in Figure 1.17. The multilayer architecture is necessary because magnetic materials such as cobalt, nickel, and iron are not amenable to RIE. The block copolymer pattern was sequentially transferred to the underlying silicon oxide and tungsten layers through an RIE process. The patterned tungsten layer serves as a hard mask for pattern transfer to cobalt layer through an ion beam etching process. The resulting cobalt particle array has a density as high as 30 Gparticles/cm^2.

As introduced previously, block copolymer microdomains can work as nanoreactors for the synthesis of nanoparticles. By choosing $FeCl_3$ as a precursor, Yun *et al* demonstrated a different approach to obtain magnetic particle arrays on a surface.[88] First, $FeCl_3$ was loaded in the PVP core of the PS-*b*-P4VP copolymer micelle formed in toluene, which is the selective solvent of the PS block. Upon spin-coating, the micelles spontaneously assembled into a quasi-hexagonal array on the substrate. An oxygen plasma treatment was introduced to fabricate the iron oxide nanoparticles through the oxidization of the $FeCl_3$ precursor and to remove the polymer template at the same time.

As a result, an iron oxide particle array that preserves the dimensional order of micelles was fabricated. The size of the nanoparticles can be tuned by simply varying the loading ratio of $FeCl_3$ relative to the P4VP. Magnetic property measurements indicate that the iron oxide nanoparticles exhibit ferrimagnetic or superparamagnetic behaviour depending on the particle size.

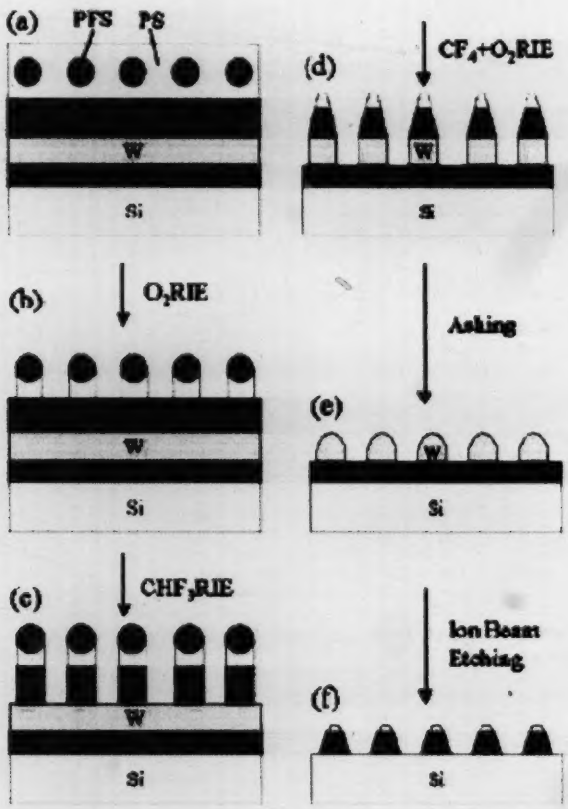

Figure 1.17. Fabrication process of the cobalt dot array via block copolymer lithography.[87]

1.5 Scope of the Thesis

In this thesis, a new approach to fabricate ordered nanopit arrays on Si is established using block copolymer nanolithography. One unique feature of the nanopit array obtained by the block copolymer templated etching process is the chemical functionality difference between the interior and exterior of the nanopits. By tailoring the chemistry of nanopits, nanoparticle arrays were prepared, using the nanopits as the template for the structures. The potential applications of the ordered nanoparticle arrays for chemical analysis based on surface enhanced Raman scattering effects were investigated.

In chapter 2, block copolymer self-assembly-based templated nanoscale etching of silicon to produce three-dimensional nanoscale features with controllable shapes, sizes, average spacing, and chemical functionalization is demonstrated. Self-assembled PS-*b*-P4VP copolymer micelle arrays were used as the template. The distinct chemical properties of the two blocks were used to direct the standard fluoride based etchant to etch the silicon surface and produce ordered nanopit arrays. The block copolymers serve to direct the silicon surface chemistry by controlling the spatial location of the reaction, as well as the concentration of reagents.

In chapter 3, the chemical functionalities of nanopit arrays were investigated. Because fluoride-based etching of Si(s) yields surface-bound Si-H_x groups, the walls of the etch pits are hydride-terminated, while the exterior of the nanopits remains coated by native oxide. The different chemical functionalities of the interiors and exteriors of the nanopits are supported by direct surface infrared spectra measurements. By employing

the correct choice of synthetic approach, controlled growth of metal nanocrystal arrays directly from the nanopits is demonstrated.

In chapter 4, we demonstrated the fabrication of nanoparticle arrays with controlled nanoparticle aggregation, taking advantage of both the topological and chemical pattern of the nanopit array. By selectively functionalizing the interior of nanopits with organic monolayers, the nanoparticles can be selectively captured within the etched nanopits. The nanoparticles exhibit different aggregation behaviour inside the nanopits depending upon the particle size and pit diameter, due to steric restriction effects. Different nanoparticle aggregations array exhibit distinct surface Raman enhancement effects, which provide a new platform for trace-amount chemical analysis application.

A conclusion and outlook chapter will finish the thesis.

References

1 http://www.its.caltech.edu/~feynman/plenty.html.

2 (a) Drexler, K. E. *Engines of Creation 2.0: The Coming Era of Nanotechnology;* Anchor Press/Doubleday: New York, 1986. (b) Drexler, K. E. *Nanosystems: Molecular Machinery, Manufacturing, and Computation;* John Wiley & Sons: New York, 1992.

3 Xia, Y.; Rogers, J. A.; Paul, K. E.; Whitesides, G. M. *Chem. Rev.* **1999**, *99*, 1823.

4 http://www.intel.com/technology/45nm/index.htm

5 http://www.itrs.net/Links/2007ITRS/2007_Chapters/2007_Lithography.pdf

6 Gates, B. D.; Xu, Q.; Stewart, M.; Ryan, D.; Willson, C. G.; Whitesides, G. M. *Chem. Rev.* **2005**, *105*, 1171.

7 Barth, J. V.; Costantini, G.; Kern, K. *Nature* **2005**, *437*, 671.

8 Rosenfield, M. G.; Thomson, M. G. R.; Coane, P. J.; Kwietniak, K. T.; Keller, J.; Klaus, D. P.; Volant, R. P.; Blair, C. R.; Tremaine, K. S.; Newman, T. H.; Hohn, F. J. *J. Vac. Sci. Technol. B* **1993**, *11*, 2615.

9 Binnig,G.; Rohrer, H.; Gerber, Ch.; Weibel, E. *Appl. Phys. Lett.*, **1982**, *40*, 178.

10 Binnig, G.; Quate, C. F.; Gerber, Ch. *Phys. Rev. Lett.* **1986**, *56*, 930.

11 Piner, R. D.; Zhu, J.; Xu, F.; Hong, S.; Mirkin, C. A. *Science*, **1999**, *283*, 661.

12 Ginger, D.S.; Zhang, H.; Mirkin, C.A. *Angew. Chem. Int. Ed.* **2004**, *43*, 30.

13 Lee, K-B.; Lim, J-H.; Mirkin, C.A. *J. Am. Chem. Soc.* **2003**, *125*, 5588.

14 Liu, X.; Fu, L.; Hong, S.; Dravid, V. P.; Mirkin, C. A. *Adv. Mat.*, **2002**, *14*, 231.

15 Demers, L. M.; Ginger, D. S.; Park, S.-J.; Li, Z.; Chung, S.-W.; Mirkin,C. A. *Science*, **2002**, *296*, 1836-1838.

16 Nyffenegger, R. M.; Penner, R. M. *Chem. Rev.* **1997**, *97*, 1195.

17 Kramer, S.; Fuierer, R. R.; Gorman, C. B. *Chem. Rev.* **2003**, *103*, 4367.

18 Liu, G.-Y.; Xu, S.; Qian, Y. *Acc. Chem. Res.* **2000**, *33*, 457-466.

19 Maynor, B. W.; Filocamo, S. F.; Grinstaff, M. W.; Liu, J. *J. Am. Chem. Soc.* **2002**, *124*, 522.

20 Hurley, P. T.; Ribbe, A. E.; Buriak, J. M. *J. Am. Chem. Soc.* **2003**, *125*, 11334.

21 Hong, S.; Mirkin, C. A. *Science*, **2000**, *288*, 1808.

22 Salaita, K. S.; Wang, Y.; Fragala, J.; Liu, C.; Mirkin, C. A. *Angew. Chem. Int. Ed.*, **2006**, *45*, 7220.

23 Xia, Y.; Whitesides, G. M., *Annu. Rev. Mater. Sci.* **1998**, *28*, 153.

24 Xia, Y.; Whitesides, G. M. *Angew. Chem. Int. Ed. Engl.* **1998**, *37*, 551.

25 Jackman, R.; Wilbur, J.; Whitesides, G. M. *Science*, **1995**, *269*, 664.

26 Odom, T. W.; Love, J. C.; Wolfe, D. B.; Paul, K. E.; Whitesides, G. M. *Langmuir* **2002**, *18*, 5314.

27 Chou, S. Y.; Krauss, P. R.; Renstrom, P. J. *Science* 1996, 272, 85.

28 (a) Förster, S.; Antonietti, M. *Adv. Mater.* **1998**, *10*, 195. (b) Förster, S.; Plantenberg, T. *Angew. Chem. Int. Ed.* **2002**, *41*, 688.

29 Hamley, I. W. *Angew. Chem. Int. Ed.* **2003**, *42*, 1692.

30 Matsen, M. W.; Bates, F. S. *Macromolecules* **1996**, *29*, 1091.

31 (a) Förster, S.; Khandpur, A. K.; Zhao, J.; Bates, F. S.; Hamley, I. W.; Ryan, A. J.; Bras, W. *Macromolecules* **1994**, *27*, 6922. (b) Khandpur, A. K.; Förster, S.;

Bates, F. S.; Ryan, A. J.; Bras, W.; Hamley, I. W. *Macromolecules* **1995**, *28*, 8796.

32 Bates, F. S.; Schulz, M. F.; Khandpur, A. K.; Forster, S. and Rosedale, J. H.; Almdal, K.; Mortensen, K. *Faraday Discuss.*, **1994**, *98*, 7.

33 Li, M.; Ober, C. K. *Mater. Today* **2006**, *9*, 30.

34 Hamley, I. W. *Nanotechnology* **2003**, *14*, R39.

35 Park, C.; Yoon, J.; Thomas. E. L. *Polymer* **2003**, *44*, 6725.

36 Shchukin, D. G.; Sukhorukov, G. B. *Adv. Mater.* **2004**, *16*, 671.

37 Krishnamoorthy, S.; Hinderling, C.; Heinzelmann, H. *Mater. Today* **2006**, *9*, 40.

38 Hawker, C. J.; Russell, T. P. *MRS Bull.* **2005**, *30*, 952.

39 Spatz, J. P. *Angew. Chem., Int. Ed.* **2002**, *41*, 3359.

40 Park, M.; Harrison, C.; Chaikin,P. M. Register, R. A.; Adamson, D. H. *Science* **1997**, *276*, 1401

41 Fasolka, M. J.; Mayes, A. M. *Annu. Rev. Mater. Res.* **2001**. *31*, 323.

42 Fasolka, M. J.; Banerjee, P.; Mayes, A. M.; Pickett, G.; Balazs, A. C. *Macromolecules* **2000**, *33*, 5702.

43 Knoll, A.; Horvat, A.; Lyakhova, K. S.; Krausch, G.; Sevink, G. J. A.; Zvelindovsky, A.V.; Magerle, R. *Phys. Rev. Lett.* **2002**, *89*, 035501

44 Mansky, P.; Liu, Y.; Huang, E.; Russell, T. P.; Hawker, C. *Science* **1997**, *275*, 1458.

45 Huang, E.; Rockford, L.; Russell, T. P.; Hawker, C. J. *Nature*, **1998**, *395*, 757.

46 Thurn-Albrecht, T.; Steiner, R. DeRouchey, J.; Stafford, C. M.; Huang, E.; Bal, M.; Tuominen, M.; Hawker, C. J.; Russell, T. P. *Adv. Mater.* **2000**, *12*, 787.

47 Spatz, J. P.; Herzog, T.; Mossmer, S.; Ziemann, P.; Moller, M. *Adv. Mater.* **1999**, *11*, 149.

48 Glass, R.; Moller, M.; Spatz, J. P. *Nanotechnology* **2003**, *14*, 1153.

49 Spatz, J. P.; Mossmer, S.; Hartmann, C.; Moller, M.; Herzog, T.; Krieger, M.; Boyen, H.-G.; Ziemann, P.; Kabius, B. *Langmuir* **2000**, *16*, 407.

50 Krishnamoorthy, S.; Pugin, R.; Brugger, J.; Heinzelmann, H.; Hinderling C. *Adv. Funct. Mater.* **2006**, *16*, 1469.

51 Spatz, J. P.; Chan, V. Z. H.; Mossmer, S.; Kamm, F.-M.; Plettl, A.; Ziemann, P.; Moller, M. *Adv. Mater.* **2002**, *14*, 1827.

52 Massey, J. A.; Winnik, M. A.; Manners, I.; Chan, V. Z.-H.; Ostermann, J. M.; Enchelmaier, R.; Spatz, J. P.; Moller, M. *J. Am. Chem. Soc.* **2001**, *123*, 3147.

53 Kim, S. H.; Misner, M. J.; Xu, T.; Kimura, M.; Russell, T. P. *Adv. Mater.* **2004**, *16*, 226.

54 Kim, S. H.; Misner, M. J.; Russell, T. P. *Adv. Mater.* **2004**, *16*, 2119.

55 Yun, S.-H.; Yoo, S. I.; Jung, J. C.; Zin, W.-C.; Sohn, B.-H. *Chem. Mater.* **2006**, *18*, 5646.

56 Bang, J.; Kim, S. H.; Drockenmuller, E.; Misner, M. J.; Russell, T. P.; Hawker, C. J. *J. Am. Chem. Soc.* **2006**, *128*, 7622.

57 Cheng, J. Y.; Ross, C. A.; Smith, H. I.; Thomas, E. L. *Adv. Mater.* **2006**, *18*, 2505.

58 Stoykovich, M. P.; Nealey, P. F. *Mater. Today*, **2006**, *9*, 20.

59 (a) Segalman, R. A.; Yokoyama, H.; Kramer, E. J. *Adv. Mater.* **2001**, *13*, 1152. (b) Segalman, R. A.; Hexemer, A.; Hayward, R. C.; Kramer, E. J. *Macromolecules*, **2003**, *36*, 3272.

60 Kim, S. O.; Solak, H. H.; Stoykovich, M. P.; Ferrier, N. J.; de Pablo, J. J.; Nealey, P. F. *Nature* **2003**, *424*, 411.

61 Cheng, J. Y.; Ross, C. A.; Thomas, E. L.; Smith, H. I.; Vancso, G. J. *Appl. Phys. Lett.* **2002**, *81*, 3657.

62 Cheng, J. Y.; Ross, C.A.; Thomas, E. L.; Smith, H. I.; Vancso, G. J. *Adv. Mater.* **2003**, *15*, 1599.

63 Guarini, K. W.; Black, C. T.; Zhang, Y.; Kim, H.; Sikorski, E. M.; Babich, I. V. *J. Vac. Sci. Technol. B* **2002**, *20*, 2788.

64 Harrison, C. Park, M. Chaikin, P. M.; Register, R. A.; Adamson, D. H. *J. Vac. Sci. Technol. B* **1998**, *16*, 544.

65 Thurn-Albrecht, T.; Schotter, J.; Kastle, G. A.; Emley, N.; Shibauchi, T.; Krusin-Elbaum, L.; Guarini, K.; Black, C. T.; Tuominen, M. T.; Russell, T. P. *Science*, **2000,** *290*, 2126

66 Thurn-Albrecht, T.; DeRouchey, J.; Russell, T. P.; Jaeger, H. M. *Macromolecules* **2000**, *33*, 3250.

67 (a) Amundson, K.; Helfand, E.; Quan, X.; Smith, S. D. *Macromolecules* **1993**, *26*, 2698. (b) Amundson, K.; Helfand, E.; Quan, X.; Hudson, S. D.; Smith, S. D. *Macromolecules* **1994**, *27*, 6559.

68 Shipway, A. N.; Katz, E. Willner, I. *ChemPhysChem* **2000**, *1*, 18.

69 Spatz, J. P.; Sheiko, S.; Moller, M. *Macromolecules* **1996**, *29*, 3220.

70 Kästle, G.; Boyen, H.-G.; Weigl, F.; Lengl, G.; Herzog, T.; Ziemann, P.; Riethmüller, S.; Mayer, O.; Hartmann, C.; Spatz, J. P.; Möller, M.; Ozawa, M.; Banhart, F.; Garnier, M. G.; Oelhafen P. *Adv. Func. Mater.* **2003**, *13*, 853.

71 Haupt, M.; Miller, S.; Ladenburger, A.; Sauer, R.; Thonke, K.; Spatz, J. P.; Riethmuller, S.; Moller, M.; Banhart, F. *J. Appl. Phys.* **2002**, *91*, 6057.

72 Bennett, R. D.; Xiong, G. Y.; Ren, Z. F.; Cohen, R. E. *Chem. Mater.* **2004**, *16*, 5589.

73 Spatz, J.; Mossmer, S.; Moller, M.; Kocher, M.; Neher, D.; Wegner, G. *Adv. Mater.* **1998**, *10*, 473.

74 (a) Kim, D. H.; Kim, S. H.; Lavery, K.; Russell, T. P. *Nano Lett.* **2004**, *4*, 1841. (b) Kim, D. H.; Jia, X.; Lin, Z.; Guarini, K. W.; Russell, T. P. *Adv. Mater.* **2004**, *16*, 702.

75 (a) Lu, J. Q.; Kopley, T. E.; Moll, N.; Roitman, D.; Chamberlin, D.; Fu, Q.; Liu, J.; Russell, T. P.; Rider, D. A.; Manners, I.; Winnik, M. A. *Chem. Mater.* **2005**, *17*, 2227. (b) Lammertink, R. G. H.; Hempenius, M. A.; Vancso, G. J.; Chan, V. Z.-H.; Thomas, E. L. *Chem. Mater.* **2001**, *13*, 429.

76 (a) Sankaran,V.; Yue, J.; Cohen, R. E.; Schrock, R. R.; Silbey, R. J. *Chem. Mater.* **1993**, *5*, 1133. (b) Chan, Y. N. C.; Craig,G. S. W.; Schrock, R. R.; Cohen, R. E. *Chem. Mater.* **1992**, *4*, 885.

77 Cohen, R. E. *Curr. Opin. Solid State Mater. Sci.* **1999**, *4*, 587.

78 Aizawa, M.; Buriak, J. M. *J. Am. Chem. Soc.* **2005**, *127*, 8932. (b) Aizawa, M.; Buriak, J. M. *Chem. Mater.* **2007**, *19*, 5090.

79 Aizawa, M.; Buriak, J. M. *J. Am. Chem. Soc.* **2006**, *128*, 5877.

80 (a) Zehner, R. W.; Sita, L. R. *Langmuir* **1999**, *15*, 6139. (b) Zehner, R. W.; Lopes, W. A.; Morkved, T. L.; Jaeger, H.; Sita, L. R. *Langmuir* **1998**, *14*, 241.

81 Lin, Y.; Boker, A.; He, J.; Sill, K.; Xiang, H.; Abetz, C.; Li, X.; Wang, J.; Emrick, T.; Long, S.; Wang, Q.; Balazs, A.; Russell, T. P. *Nature*, **2005**, *434*, 55.

82 Deshmukh, R. D.; Liu, Y.; Composto, R. J. *Nano Lett.* **2007**, *7*, 3662.

83 Lopes, W. A.; Jaeger, H. M. *Nature* **2001**, *414*, 735.

84 Black, C. T.; Guarini, K. W.; Zhang, Y.; Kim, H. J.; Benedict, J.; Sikorski, E.; Babich, I. V.; Milkove, K. R. *IEEE Electron Device Lett.* **2004**, *25*, 622.

85 Black, C. T.; Guarini, K. W.; Milkove, K. R.; Baker, S. M.; Russell, T. P.; Tuominen, M. T. *Appl. Phys. Lett.* **2001**, *79*, 409.

86 Black, C. T. *Appl. Phys. Lett.* **2005**, *87*, 163116.

87 Cheng, J. Y.; Ross, C. A.; Chan, V. Z.-H.; Thomas, E. L.; Lammertink, R. G. H.; Vancso, G. J. *Adv. Mater.* **2001**, *13*, 1174.

88 Yun, S.-H.; Sohn, B.-H.; Jung, J. C.; Zin, W.-C.; Lee, J.-K.; Song, O. *Langmuir* **2005**, *21*, 6548.

Chapter 2

Block Copolymer Templated Etching on Silicon

2.1 Introduction

The fabrication of sub-100 nm features on silicon surfaces is a critical challenge for future technological devices based on silicon-based materials, including hybrid silicon-organic and nanoparticle devices, molecular electronics, micro- and nanofluidics, sensing, photovoltaics, and others.[1,2] The most important representative top-down technique, photolithography, has seen decades of remarkable improvements, leading to the latest 65 nm commercial transistor technologies, with further decreases in size and chip densities still expected.[3] The sheer monetary and energetic costs of manufacturing such devices have reached such an unprecedented magnitude, however, that alternative strategies to produce patterned silicon architectures are under intense investigation in both academia and industry.[3] To be considered commercially viable in the near to mid-term and beyond, new processes should ideally be compatible with existing silicon-based micro- and nanofabrication techniques.

Polymer self-assembly has recently arisen as one possible approach to uniformly pattern large areas of semiconductor interfaces.[4,5,6,7,8,9,10] The spontaneous phase separation of block copolymers into nanoscale domains can be harnessed in a cost-effective manner to efficiently and simultaneously produce periodic patterns.[11,12,13,14,15,16] While certainly not intended to replace photolithography, polymer self-assembly is complementary due in large part to the ubiquity of polymers in IC fabrication processes as photoresists.[4] For instance, IBM announced in 2003 its intention to utilize self-

assembled block copolymers that form quasi-hexagonal close packed templates for manufacture of floating silicon gates for flash memory. The approach is based upon techniques first described in 1997 in which a block copolymer monolayer serves as a mask for plasma and reactive ion etching.[17] So far, fabrication of sub-100 nm electronic devices, such as capacitor, field-effect transistor, and magnetic storage array, using block copolymer nanolithography has been demonstrated.[5,18,19]

While the covalent linking of two chemically distinct polymer blocks leads to an amphiphilic molecule, a property critical for the self-assembly process, the dual nature of the polymer can also be used to direct chemical reagents to the surface in a spatially defined manner, as outlined in Figure 2.1. The chemical specificity of one block over the other towards passage and transport of reagents to the surface results in localized reactivity, directed by the parent block copolymer.[13,20] The reaction described in this work is based upon the central ingredient in silicon surface processing, the fluoride ion [F^- (aq)], typically derived from either hydrofluoric acid [HF (aq)] or ammonium fluoride [NH_4F (aq)].[21,22,23] Aqueous fluoride treatment of silicon wafers leads to rapid dissolution of silicon oxide, and depending upon the length of exposure, etching of the silicon lattice and hydride termination.[19,21] Here we demonstrate that self-assembled block copolymer-based quasi-hexagonal template arrays can direct aqueous fluoride-based etching of silicon surfaces, to produce three-dimensional nanoscale features with controllable shapes, sizes, average spacing, and chemical functionalization.

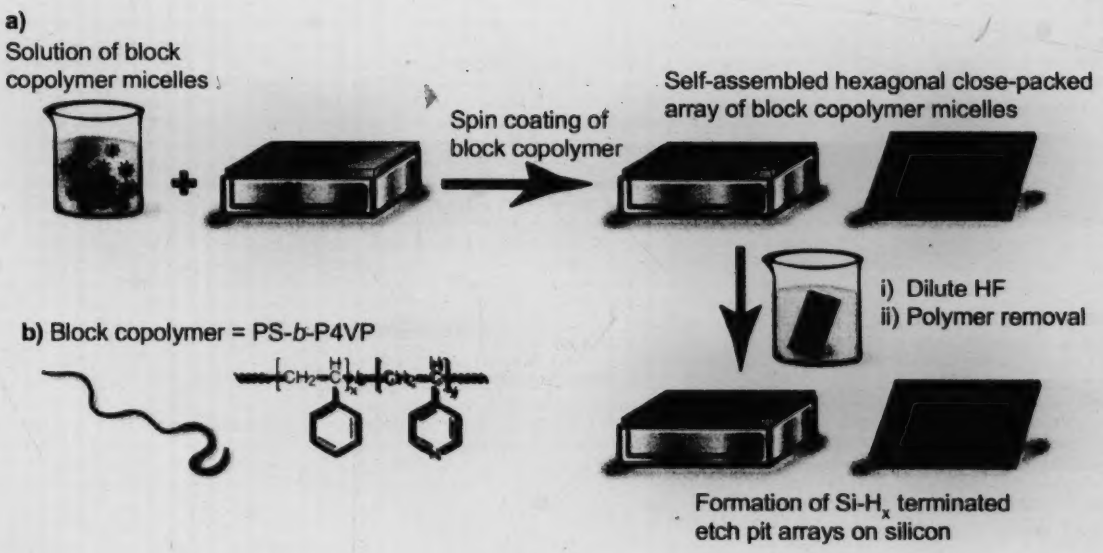
a)
Solution of block copolymer micelles
Spin coating of block copolymer
Self-assembled hexagonal close-packed array of block copolymer micelles
i) Dilute HF
ii) Polymer removal
b) Block copolymer = PS-b-P4VP
Formation of Si-H$_x$ terminated etch pit arrays on silicon

Figure 2.1. Schematic diagram for the fabrication of the etch pits on a Si(100) surface using PS-*b*-P4VP as the template. (a) The polymer micelles formed in toluene solution were spin-coated onto a native oxide-coated silicon surface, and the micelles spontaneously self-assembled into a quasi-hexagonal close-packed monolayer array on the surface. Next, the polymer thin film-coated silicon shard was dipped into an HF (aq) solution for the designated time. The etch pit array (squares shown here) was obtained after removal of the polymer. (b) Chemical structure of the PS-*b*-P4VP block copolymer.[24]

2.2 Results and Discussion

The amphiphilic block copolymer, polystyrene-*block*-poly(4-vinyl pyridine), denoted throughout as PS-*b*-P4VP, was selected as the general polymer for template surface patterning, as illustrated schematically in Figure 2.1. This block copolymer was chosen since it contains the pyridyl group, a Brönsted base. By dissolving the copolymer into toluene, a micelle solution with P4VP core and PS corona is generated. The sizes of the micellar core (represented in blue) and the corona (represented in red) are easily controlled through variation of the molecular weight of two blocks.[25] The micelles are transferred from solution onto the Si surface by spin-coating or dip-coating, upon which they spontaneously self-assemble into monolayers of quasi-hexagonal arrays, thus resulting in formation of the template for the subsequent etching process. Through immersion of native oxide-capped Si wafers of different orientations, coated with a monolayer of the self-assembled PS-*b*-P4VP block copolymer [PS-*b*-P4VP, (M_n=128400-*b*-33500 g/mol, PDI=1.1)] in a dilute HF (aq) solution for less than 1 h, etching of the silicon surface takes place selectively in a manner that reflects the spacing of the parent template. As shown in the plane and sectional view scanning electron microscopy (SEM) images of polymer-coated wafer shard dipping in 0.01% HF (aq) for 40 min (Figure 2.2), the etch pits develop directly under the position of P4VP cores of the copolymer film.

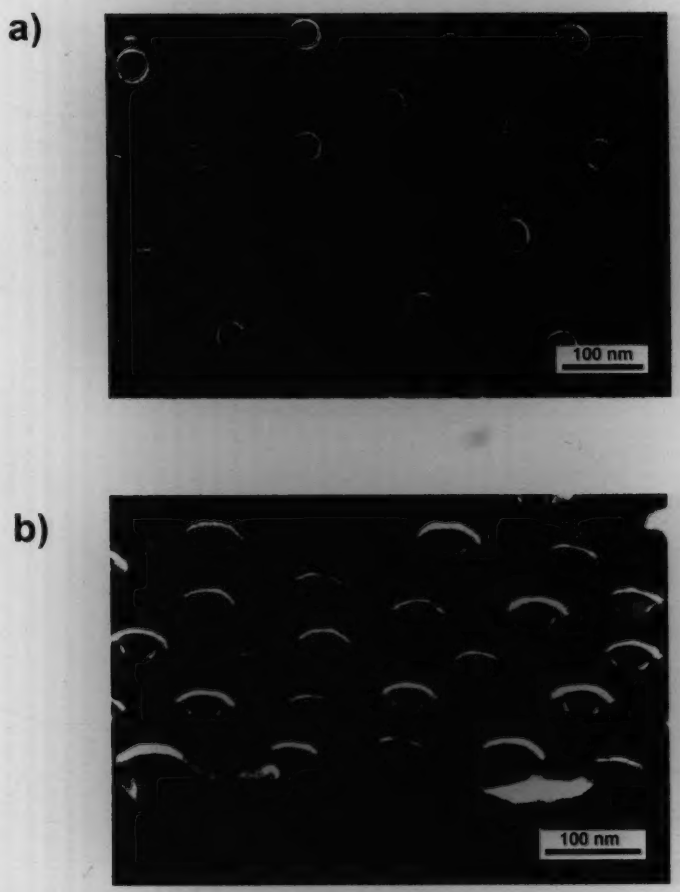

Figure 2.2. Morphology of the copolymer template coated surface after immersion into HF (aq) solution. Top (a) and side (b) view SEM images of PS-*b*-P4VP (M_n=128400-*b*-33500 g/mol)-coated Si(111) surface etched in 0.01% HF (aq) for 40 min, with the polymer left intact; the polymer removal step was omitted.[24]

2.2.1 Geometric Shape Control of the Etch pits on Silicon Surfaces of Different Orientations

After removing the polymer film through 5 min of ultrasonication of the wafer shard in neat toluene, the well-defined etch pit array is revealed. Plane view SEM images (Figures 2.3a-d) of Si(100), Si(111) and Si(110) show the formation of truncated square- and pseudohexagonal-shaped etch pits with centre-to-centre spacings of ~125 nm, identical to that of the parent block copolymer monolayer. The cross sectional images in Figures 2.3e-h reveal the three dimensional nature of the etch pits. By carefully registering the orientation of the etch pits with respect to that of the Si wafer, the assignment of the flat walls of the etch pits could be carried out. Figures 2.4a-d show the enlarged SEM images of the etch pits produced on Si wafers of different orientations. The apparently flat walls defining the shape of the etch pits are assigned to Si(111), Si(100) and possibly transitional Si(311) faces (Figure 2.4e-l, *vide infra*).[26,27] Both top view and side view models agree well with the SEM images shown in Figure 2.3. The shape of the etch pits on the silicon surfaces is dependent on the relative etch rate along different crystallographic direction, which is affected by many factors, such as the etching conditions, etchant, atomic defects in the silicon crystals, and *et al.*[28,29] For example, the relative etching rates along major crystallographic direction in pure KOH (aq) are $R_{110}>R_{100}>R_{111}$, while for EDP (ethylenediamine pyrocatechol) and KOH/IPA $R_{100}>R_{110}>R_{111}$.[30,31] Tokoro and coworkers also found that the etching rate ratio of (100)/(111) in TMAH (tetramethylammonium hydroxide) was the half of that in KOH.[32] In our system, the existence of Si(100) and Si(111) planes in the etch pits (see Figure 2.3 and Figure 2.4) indicate the etching rates is $R_{110}>>R_{100}>R_{111}$. Some degree of corner

rounding is apparent, as is common in absence of a clearly defined top surface mask.[23] Oxygen appears to play a minor role, as shown by the subtle difference in etch pit shapes on Si(100) in the presence and absence of oxygen (Figures 2.3a-b). Oxygen is an anisotropic oxidant of Si(111)-H surfaces, and thus its occurrence appears to play a minor role in etch pit morphology.[33]

Etching takes place exclusively beneath the micellar cores, in close proximity to the P4VP cores due to protonation of the pyridyl groups of the poly(4-vinylpyridine) block by HF (pK_a = 3.17) that results in selective localization of fluoride ion within the P4VP core. The protonation process results in the high local concentration of (poly)pyridinium fluoride at the silicon surface, which is reminiscent of the well studied ammonium fluoride (aq) etchant, typically used at high concentrations (~40% w/w in water). Ammonium fluoride (aq) is an anisotropic etchant that etches much more slowly along the <111> direction than along the <100> direction.[34,35] On Si(111) surfaces, anisotropic etching with NH_4F (aq) leads to atomically flat, monohydride-terminated Si(111) interfaces while it has been reported that on Si(100), a rougher interface made up of Si(111)-H microfacets and Si(100)-H_2 planes is produced.[21,36,37] The pH of NH_4F (aq) solutions used for etching silicon is critical to the microstructures of the etched surfaces. At a low pH, a relatively rough surface was produced, while an atomically flat surface can be obtained in buffered NH_4F solution with higher pH.[23,38,39] This indicates that the anisotropic vs isotropic etching was influenced by the pH of the solution. In our system, although acidic HF was used as an etchant, the local environment at the silicon surface is defined by the polymer membrane bearing with basic pyridyl groups. It is anticipated

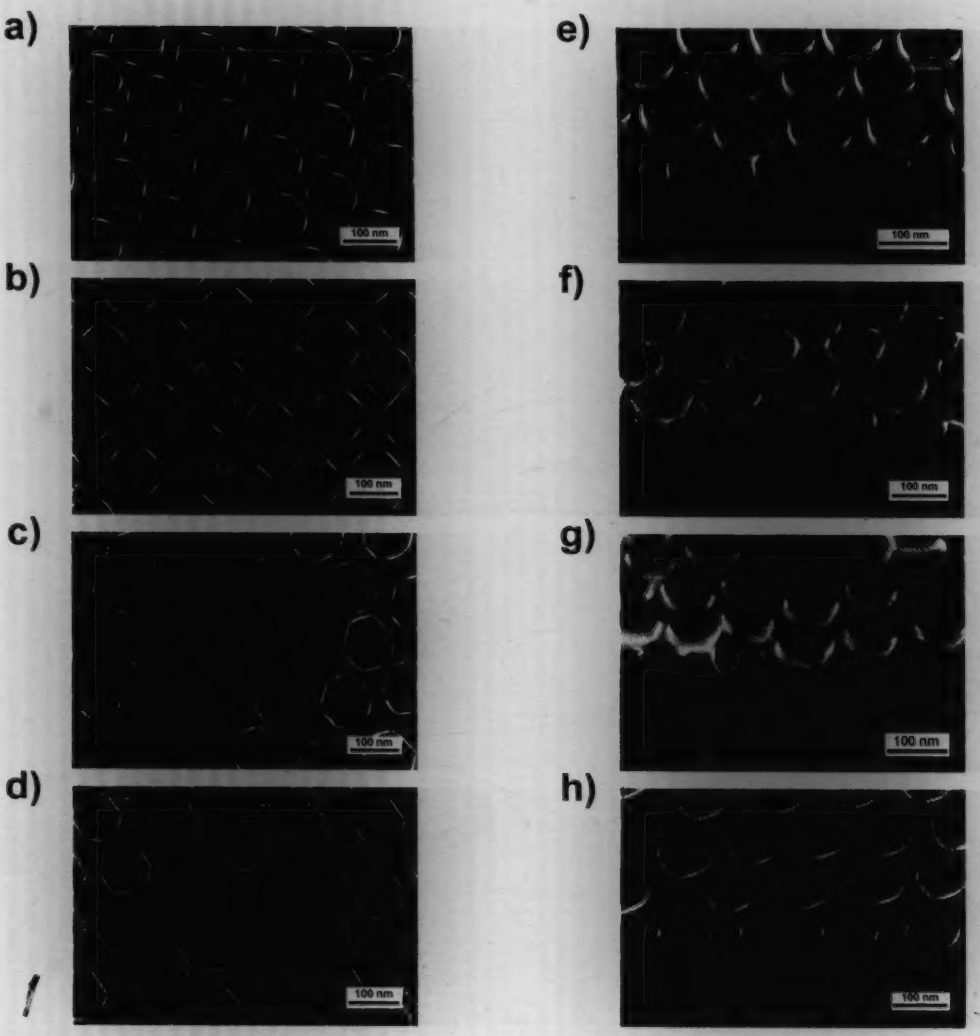

Figure 2.3. Geometric shape evolution of the patterned etch pits on different orientations of single crystalline silicon. Top (a-d) and side (e-h) view SEM images showing the etch pit arrays on silicon. (a+e) etching of Si(100), in 0.01% HF (aq) for 50 min, in air. (b+f) Si(100) etched in Ar sparged 0.01% HF (aq) for 50 min. (c+g) Si(111) etched in Ar sparged 0.01% HF (aq) for 40 min. (d+h) Si(110) etched in Ar sparged 0.01% HF (aq) for 40 min.[24]

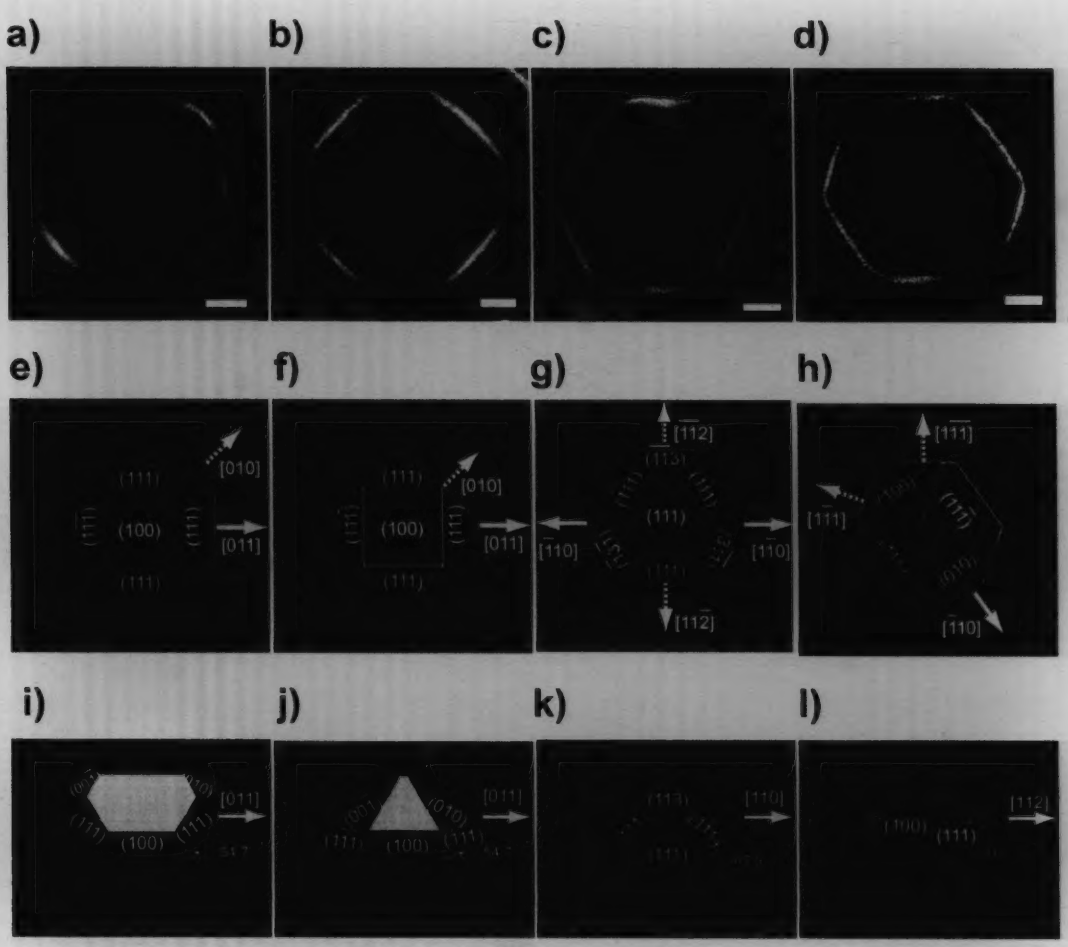

Figure 2.4. (a-d) Close-up SEM images of the etch pits obtained on silicon with different crystallographic orientations. Scale bar is 20 nm. These images correspond to the SEM images in Figure 2.3a-d. (e-h) top view and (i-l) side view models showing the proposed assignments of the exposed planes of the etch pits.[24]

that HF will protonate P4VP to form polypyridinium, which can be regarded as a buffer agent to regulate the local pH at the interfaces where etching process takes place. The local pH change will also affect the dissociation degree of HF, and thus the local concentration of fluoride ion. Overall, the anisotropic etching observed in our system is closely related to the formation of polypyridinium fluoride.

To demonstrate that the poly(pyridinium) fluoride block could be the etchant, a 56% w/w pyridinium fluoride (aq) solution was studied for the etching of the Si(100), Si(111) and Si(110) wafers (SEM images in Figures 2.5). Similar square and elongated pseudohexagonal pit shapes and morphologies are observed on Si(100) and Si(110) surfaces, respectively, although their sizes and locations are diverse and heterogeneous due to the obvious lack of spatial control. On the other hand, triangular etch pits form on Si(111) with the 56% pyridinum fluoride (aq) solution; triangular and pseudohexagonal etch pits are simply variations on the same theme, and are closely related as the two morphologies differ only in the rate of etching of the Si(11 $\bar{2}$) and Si($\bar{1}$ $\bar{1}$2) planes.[40,41] The three broad internal walls of the pseudohexagonal etch pit structures can be assigned as Si(111) faces (Figure 2.4c), identical to the three walls of the triangular etch pits.[42] The three smaller walls, on the other hand, are more difficult to assign since formation of the stable Si(111) face would result in undercutting, as has been observed in other basic etches.[32,43] A provisional assignment of an intermediary Si(311) surface would yield an almost vertical wall [~80° from surface Si(111) plane], similar to those observed here by SEM (Figure 2.3g); the Si(311) face should be considered to be composed of stair-like ledges of Si(100) and Si(111) planes.[23] The morphological shapes of the etch pits are transitional, and thus a particular form observed at any given time represents the arrested

development of the anisotropic etching reaction; the shapes may not correspond to the most stable final product of the etching solution [hence the appearance of atypical surfaces such as the proposed Si(311) faces, for instance].

2.2.2 Effect of Etching Time and Etchant Concentration

Preliminary screening revealed the importance of HF concentration with respect to both the size and shape of the etch pits, as well as etching rates. Figure 2.6 shows SEM images of the patterned etch pits on Si(100) and Si(111) substrates prepared from a variety of HF concentrations, over the range from 10% to 0.01% HF (aq) while keeping etching time at 10 min. Little etching and etch pit formation was observed below 0.01% HF (aq). SEM images indicate the etching rates for 0.1 % HF (aq) is the fastest on both Si(100) and Si(111) substrates. In addition, the characteristic square shape etch pits are seen at 1% HF (aq) concentration on silicon (100), while the shape of the etch pits formed by 0.1 % HF (aq) etching for 10 min on silicon (111) are predominately triangular. No clear orientation-dependent etch pit shape is observed at other etchant concentrations.

Slow etch rates at HF concentrations of 0.01% provide a good opportunity to study the kinetics of the etching process. In fact, evolution of the morphology of etch pits through simple modulation of immersion time reveals a range of shapes and sizes. Figures 2.7a-d show the SEM images of etch pits on Si(100), obtained at increasing etching times using PS-*b*-P4VP (M_n=128400-*b*-33500 g/mol) as the template in 0.01% HF (aq). The SEM images and the histograms in Figure 2.8 show that the etch pit diameter varied from ~14 nm to ~83 nm with increasing time; the depth of the etch pits also simultaneously increased from <5 nm to ~55 nm. In addition to the increase in depth and width, the morphology of etch pits also evolved, starting with irregularly shaped pits

at short etching times, and gradually developing into well defined geometric shapes after 30-40 min. In Figure 2.9, which shows the evolution of etch pits on Si(111) with increasing etching time, similar depth and width increase is observed.

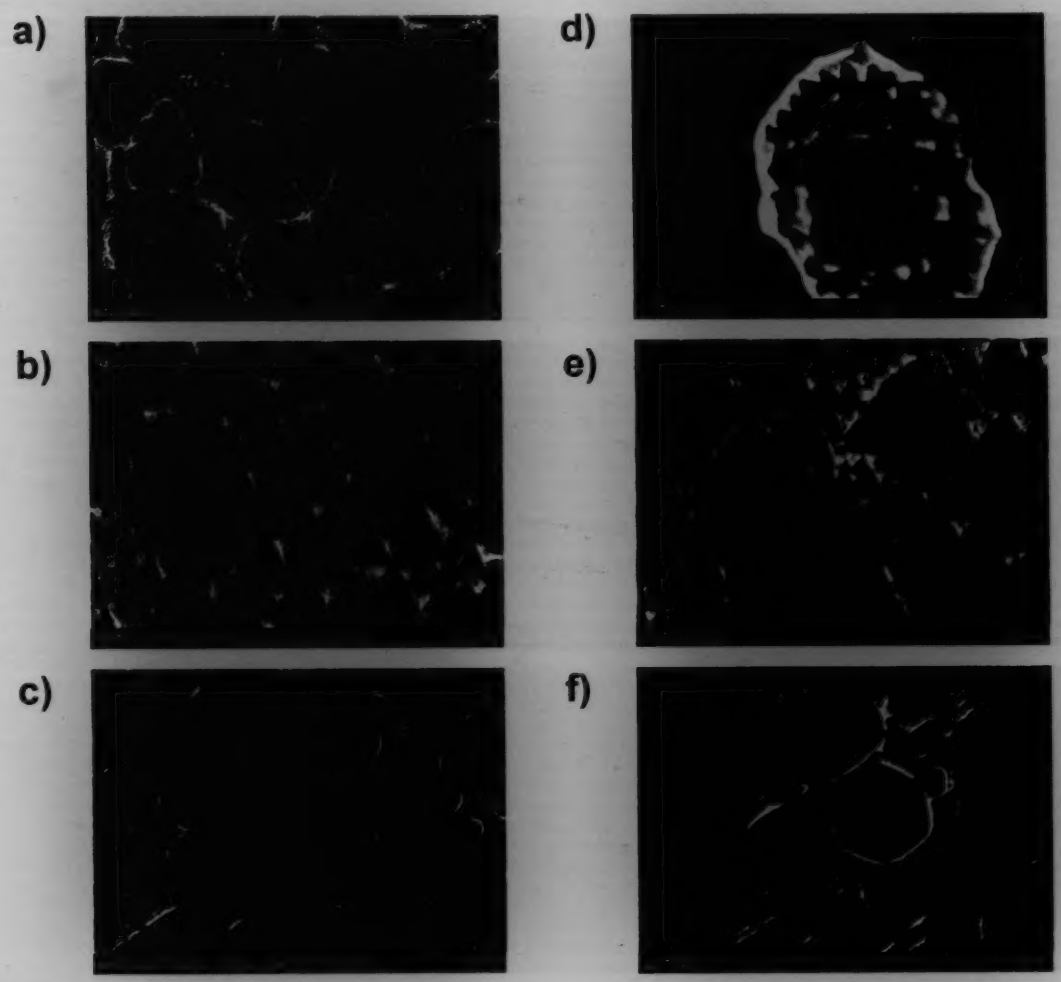

Figure 2.5. Morphologies of the silicon surfaces of different crystallographic orientations, etched by the 56% pyridinium fluoride (aq) for 1 h. (a) SEM image of the etched surface on Si(100). (b) SEM image of the etched surface on Si(111). (c) SEM image of the etched surface on Si(110). (d+e+f) Close up of etch pits on Si(100), Si(111) and Si(110), respectively.[24]

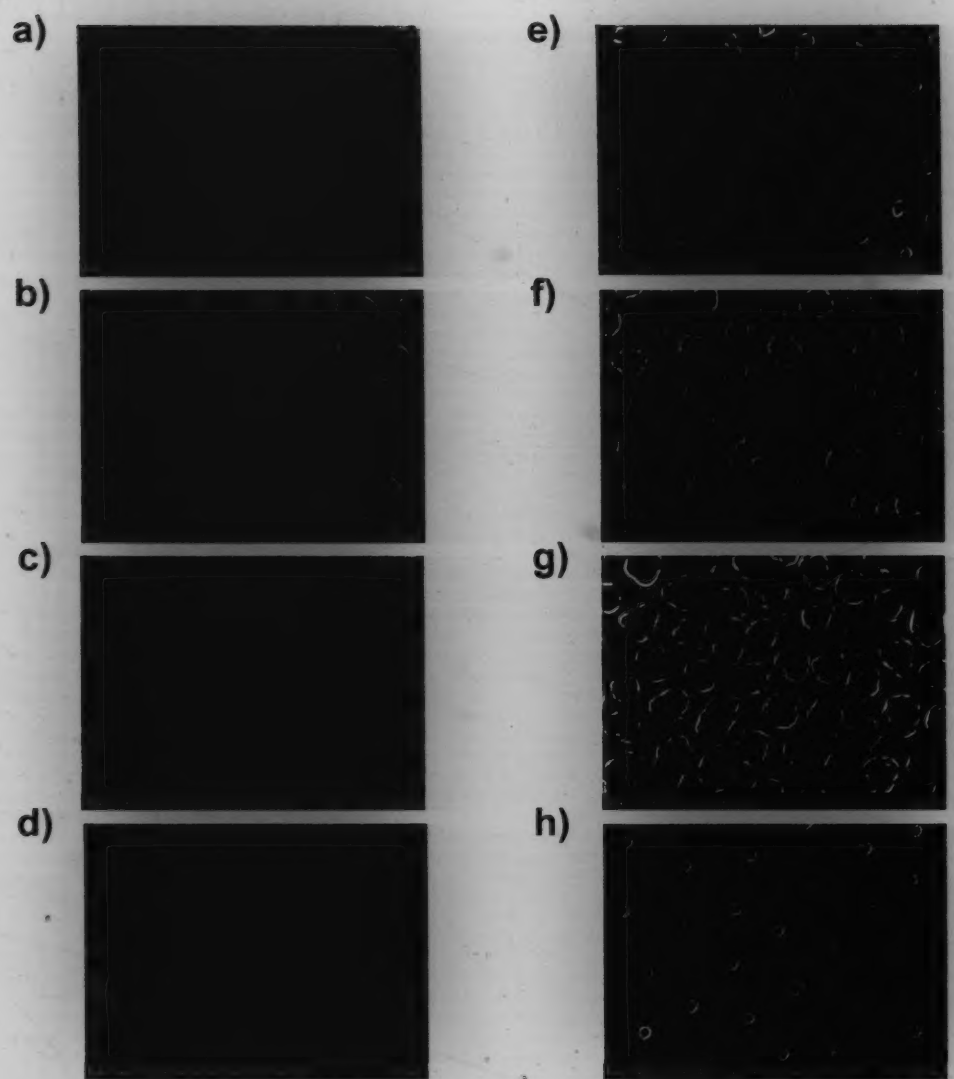

Figure 2.6. SEM images of the etch pits obtained with different concentrations of HF (aq) solutions, keeping etching time constant (10 min). (a-d) SEM images of the etch pits on Si(100). (e-h) SEM images of the etch pits on Si(111). The HF solution concentrations are 10% for (a) and (e), 1% for (b) and (f), 0.1% for (c) and (g), and 0.01 % for (d) and (h). The copolymer used is PS-*b*-P4VP (M_n=128400-*b*-33500 g/mol).[24]

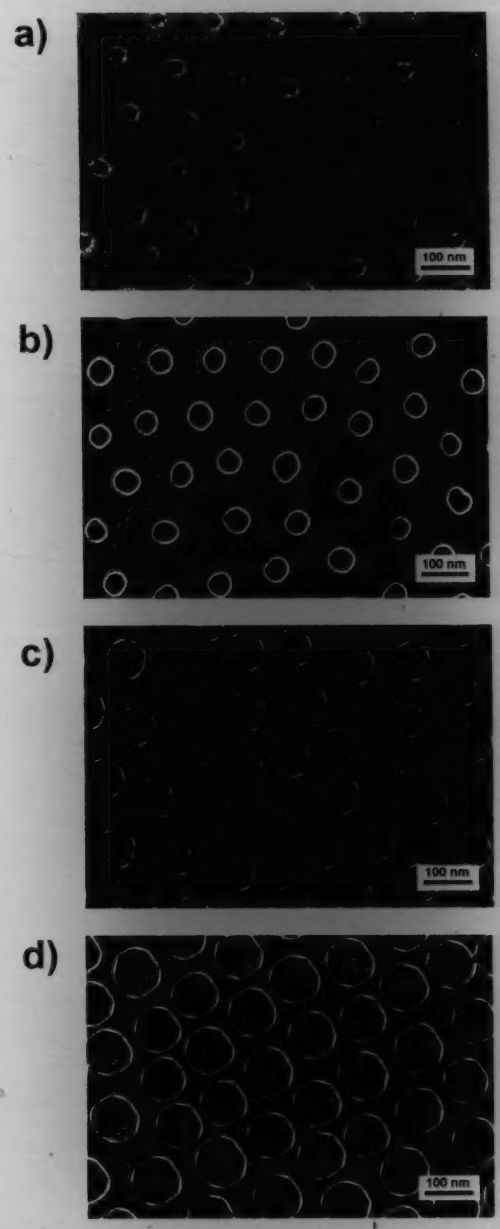

Figure 2.7. Shape evolution of etch pits with increasing etching time. SEM images of the etch pits on Si(100) obtained at different etching times using PS-*b*-P4VP (M_n=128400-*b*-33500 g/mol) as templates. The etching time from (a-d) is 20 min, 30 min, 40 min and 50 min, respectively. 0.01% HF (aq) solution was used as etchant.

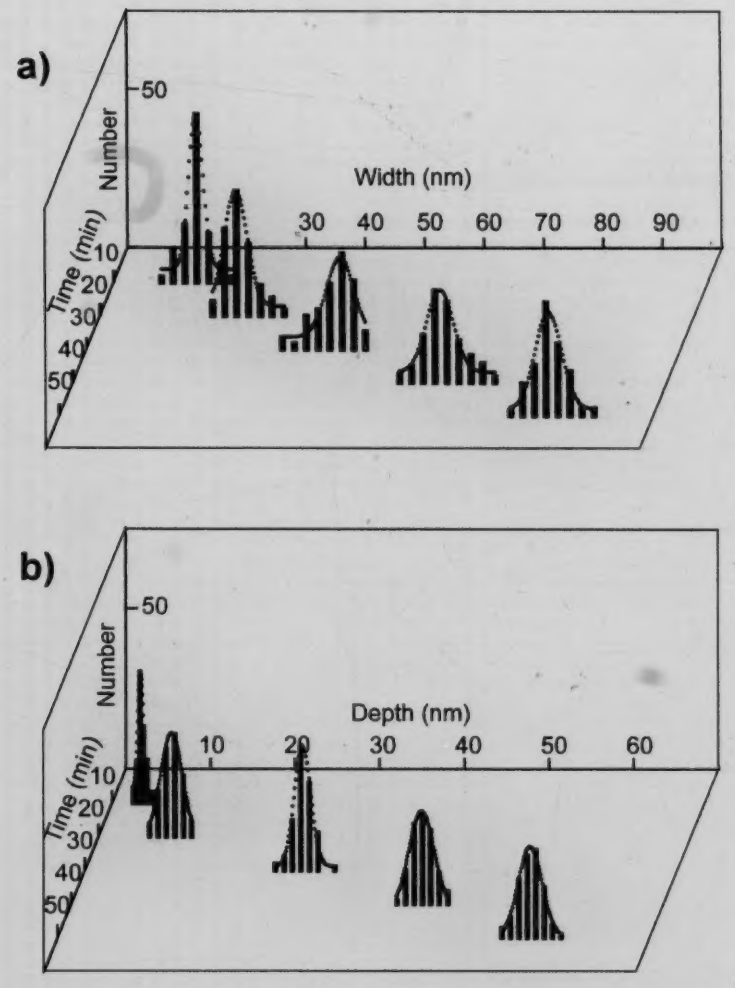

Figure 2.8. (a and b) Histogram representation of the width and depth distribution of the etch pits obtained with different etching times on Si(100).[24]

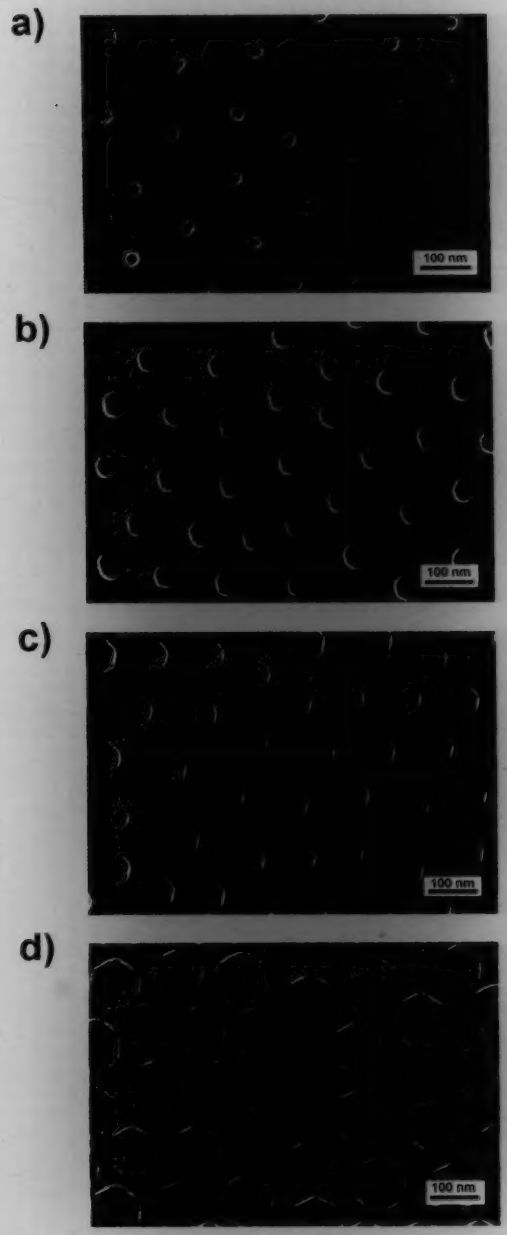

Figure 2.9. Shape evolution of etch pits with increasing etching time. SEM images of the etch pits on Si(111) obtained at different etching times using PS-*b*-P4VP (M_n=128400-*b*-33500 g/mol) as templates and 0.01% HF (aq) as etchant. The etching time from (a-d) is 10 min, 20 min, 30 min, and 40 min, respectively.[24]

While the shape evolution of etch pits with time using 0.01% HF clearly demonstrates the anisotropic nature and the kinetics of the etching process, the effect of etchant concentration seems complicated. As discussed in the previous section, the protonated polypyridinium fluoride appears to function as the anisotropic etchant in the system. The kinetics of the etching process is determined by the local concentration of polypyridinium fluoride near the surface. The local concentration of polypyridinium fluoride, however, may not be related in a linear fashion with the concentration of HF in solution since it is associated with the extent of protonation of the pyridine group by HF molecules and the core-corona conversion between PS and P4VP blocks induced in acidic solution. The incorporation of HF and inevitably water in the P4VP blocks will swell the P4VP blocks and induce the core-corona inversion of the micelles. Figure 2.10 shows the AFM images of PS-*b*-P4VP film taken after exposure to HF (aq). The swelling and inversion of P4VP cores is clearly seen. As has been previously reported, immersion of a monolayer of amphiphilic block copolymer in methanol or ethanol results in swelling of the polymer nanostructures, and also shows a similar swelling and inversion phenomenon.[44,45] The morphological shift of the PS-*b*-P4VP block copolymer would be expected to affect local concentrations of polypyridinium fluoride. As shown in Figure 2.11, this reorganization process will result in more P4VP blocks exposed to the air surface due to the swelling of P4VP blocks. At high concentration (10% HF (aq) for example), although more HF molecules protonate the pyridine groups, it also may quickly induce more P4VP blocks exposed to the air surface, which decrease the contact area between the etchant (polypyridinium fluoride) and silicon surfaces and slower the etching. While at relatively lower HF concentration (0.1 % $\approx$ 0.05 M), the interaction

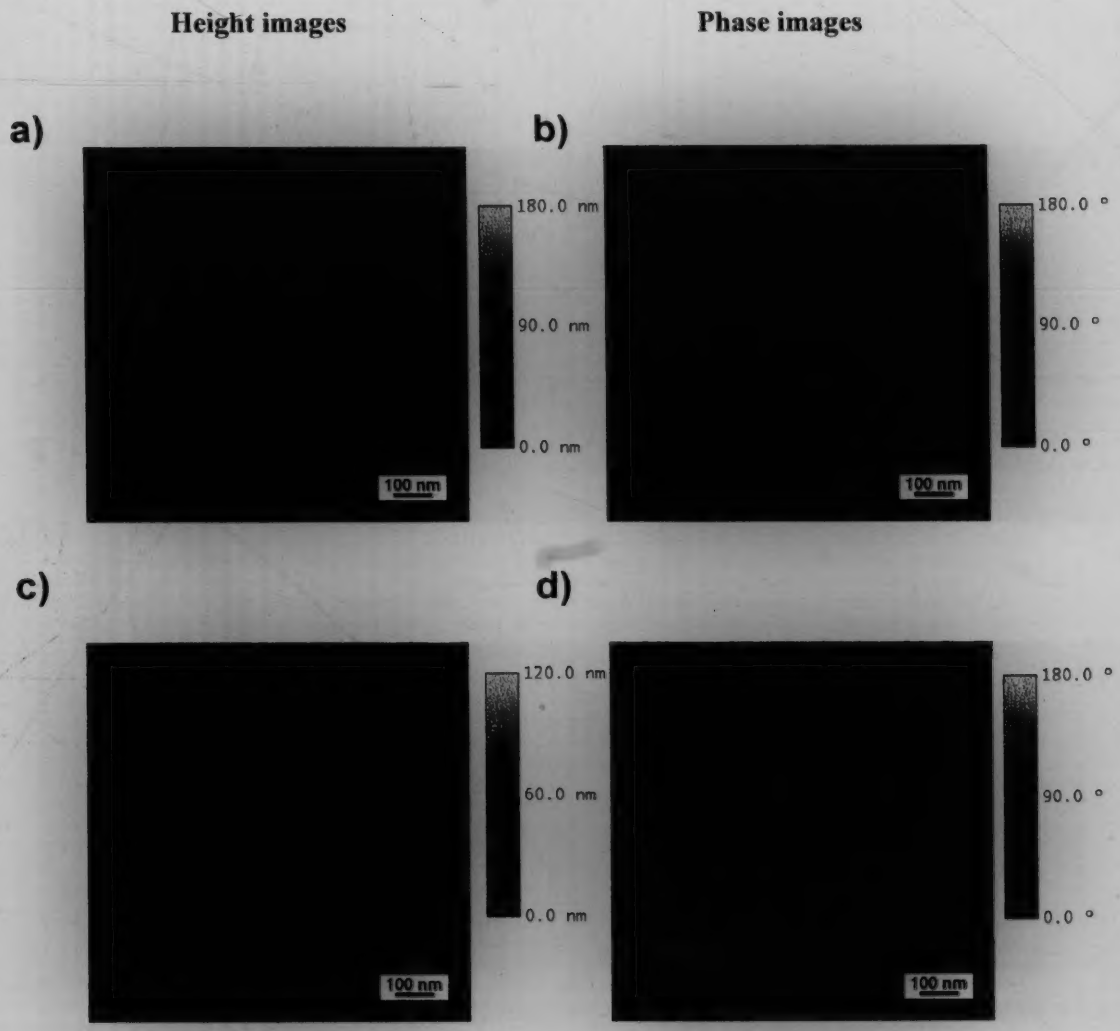

Figure 2.10. AFM height and phase images of a PS-*b*-P4VP (M_n=128400-*b*-33500 g/mol)-coated Si(100) surface before (a-b) and after (c-d) immersion in 0.01% HF (aq) for 10 min without removal of the polymer. Scan area is 1 μm × 1 μm for all images.[24]

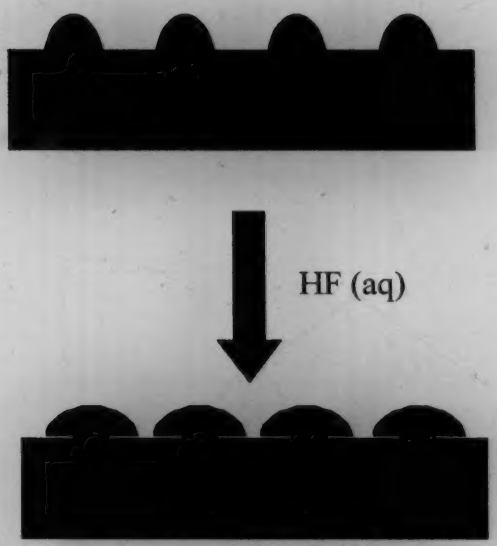

Figure 2.11. Schematic diagram shows the swelling and inversion process of PS-*b*-P4VP in acidic solution.

Table 2.1. Film thickness of the block copolymer monolayer

PS-*b*-P4VP (M_n=x-*b*-y g/mol)	Film Thickness*
20000-*b*-19000	23.4 ± 0.7 nm
57300-*b*-24700	29.5 ± 0.6 nm
128400-*b*-33500	22.8 ± 0.9 nm

* Average of 5 copolymer films on Si by spin-coating at 3000 rpm.

** The film thickness is slightly changed by varying the spin-coating speed, which has no effect on the etching process.

between the HF molecules and pyridine group on the polymer maybe proper to produce a certain concentration of polypyridinium fluoride as etchant, while induce the core-corona inversion at a less extent compared to higher concentration of HF solution. In addition, the kinetics of the Si etching process itself is complicated. Previous results indicate that many anisotropic etchants for silicon, such as NH_4F and tetramethylammonium hydroxide (TMAH), have a non-linear etch rate vs. concentration relationship. A detailed understanding of the kinetics of polypyridinium fluoride or its close analogue pyridinium fluoride on the anisotropic etching of silicon is required to fully understand the experiment results observed here.

2.2.3 Inter-distance Control of Etch Pits

In addition to shape, diameter and depth, periodicity can be controlled through utilization of block copolymers of different molecular weights. Figures 2.12a-c show atomic force microscopy (AFM) images of PS-*b*-P4VP with molecular weights of PS-*b*-P4VP (M_n=20000-*b*-19000 g/mol), PS-*b*-P4VP (M_n=57300-*b*-24700 g/mol), and PS-*b*-P4VP (M_n=128400-*b*-33500 g/mol); the centre-to-centre spacings of the P4VP cores, the bright spots in the AFM images, vary from 50 nm, to 65 nm, to 125 nm, respectively. The corresponding film thickness of each block copolymer film with the increase of the molecular weights was 23.4 ± 0.7 nm, 29.5 ± 0.6 nm, and 22.8 ± 0.9 nm, respectively, as measured by ellipsometry (see Table 2.1). Brief immersion of the PS-*b*-P4VP monolayer-capped silicon wafer in 1% HF (aq) for 3 minutes, followed by polymer removal through 5 min ultrasonication in toluene, results in etch pits on the surface with periodicity identical to that of the parent polymer template (Figures 2.12d-f).

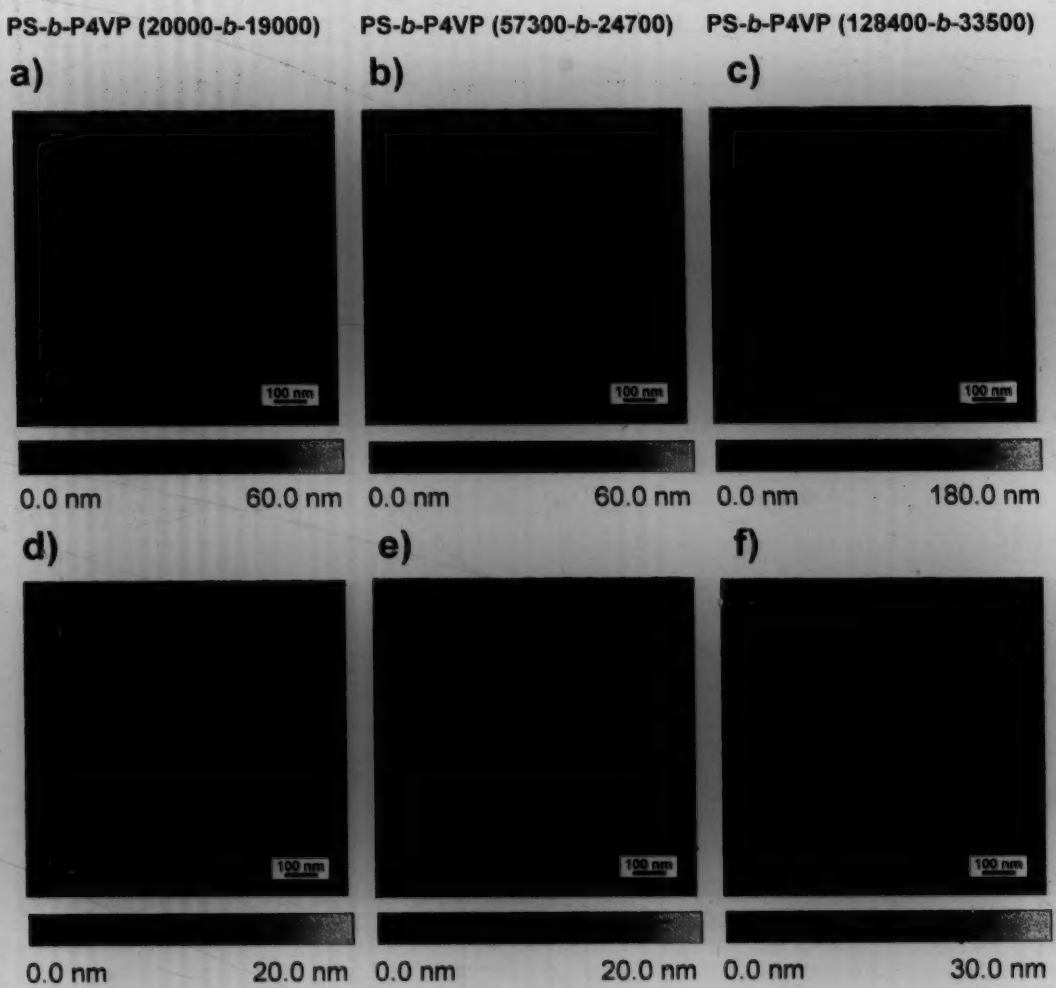

Figure 2.12. Modulation of etch pit periodicity by using block copolymers of different molecular weights. (a-c) AFM height images of PS-*b*-P4VP (x-*b*-y) thin films on a silicon (100) surface, where x and y designate the molecular weights of the PS and P4VP blocks, respectively. (d-f) AFM height images of the corresponding patterned etch pits obtained by etching with 1% HF (aq) for 3 min. Scan areas are 1 μm × 1 μm in all cases.

2.2.4 Effect of Silicon Doping

The block copolymer micelle array templated etching process is observed on both n-type and p-type silicon substrates, except for highly doped p++ wafers (1 mΩ·cm). Figure 2.13 shows the different morphologies observed on Si(100) with different dopant concentrations. Similar square shaped etch pits are seen on substrates with low doping, while little etching is observed for the p++ wafer (1 mΩ · cm). The dopant concentration dependent etching rate change is well known in the semiconductor industry,[46] and in fact, intentionally doped p++ zones in silicon wafers is used as an etch stop layer for anisotropic wet etching. An etch stop is a widely used method in silicon-based mechanical and electrical device fabrication, to selectively remove a specific material and produce the defined microstructure relief. Although the exact mechanism for the dopant-dependent etch stop process is still under debate, the model proposed by Seidel et al on the basis of the electrochemical nature of the etching process provides an elegant explanation.[47] At a high dopant level, the electrons produced in the silicon oxidation step can effectively inject into the silicon lattice due to the shrinkage of the space charge layer and recombine with holes in the valence band and thus are not available for the dissolution of silicon. The etching rate is then impeded by the lack of electrons. The understanding of the dopant-dependent etch stop in our system needs further investigation.

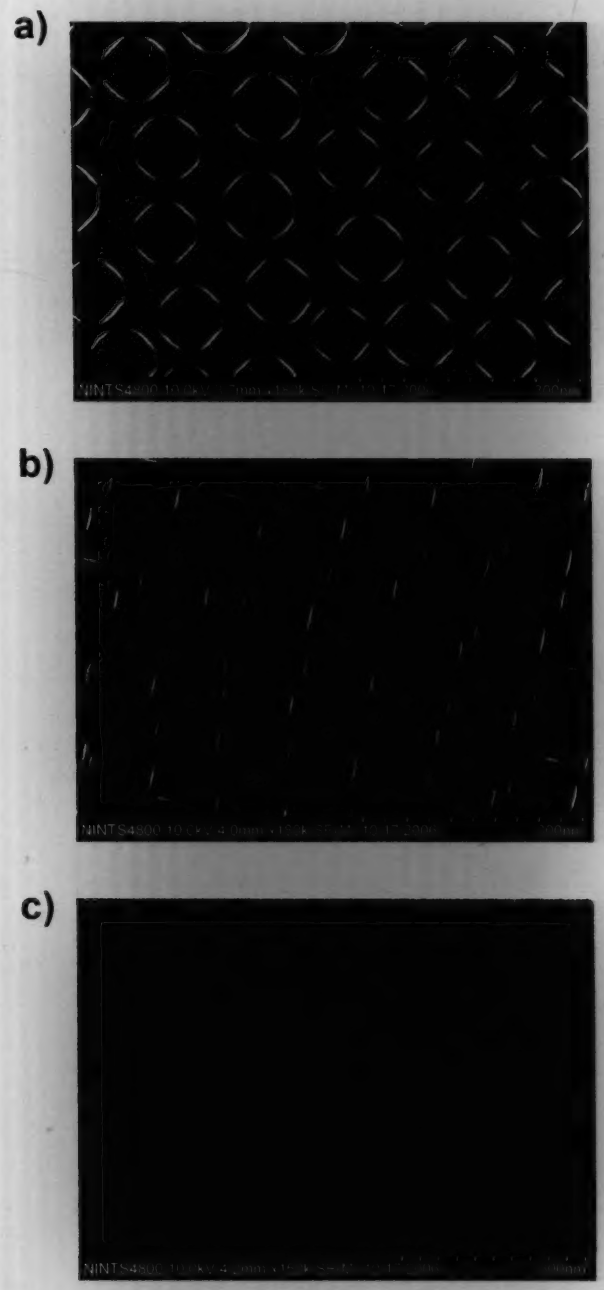

Figure 2.13. P-type silicon (100) with different resistivities etched in 0.01% HF (aq) for 50 min. (a) 6.4 Ω•cm; (b) 0.5 Ω•cm; (c) 0.001 Ω•cm.

2.2.5 Nanopatterns on Curved Surfaces

Due to the good wettability of PS-*b*-P4VP on silicon surfaces, the block copolymer templated etching process can be scaled up to pattern very large areas of surface. Large scale SEM images show that the ordered pattern extends on silicon wafer with no obvious defects over ranges of tens of microns, as exemplified in Figure 2.14. In addition, the conformal coating of copolymer micelles on surfaces creates the possibility to obtain etch pit patterns on non-planar surfaces. The fabrication of patterns on the curved surfaces is of practical use for applications in thin film transistors, biological devices, optoelectronics, and others. Soft lithography has been utilized to pattern non-planar substrates,[48,49,5051] but the feature sizes are typically at the micron-level. In the present method, the copolymer template can easily be transferred to a non-planar surface and template the subsequent patterning process. As a simple test of principle, the edge of a polished Si(111) wafer dip-coated in PS-*b*-P4VP (M_n=128400-*b*-33500 g/mol) was transferred into a 1% HF (aq) solution for 10 min. After removing the polymer, the patterned curved surface was obtained. The SEM images show the edge of the Si wafer (Figure 2.15a) and the patterned surface obtained on the different sites of curved surface (Figure 2.15b,c). This result indicates that the present method in this paper is applicable for the fabrication of nanopatterns on silicon surfaces with irregular shapes.

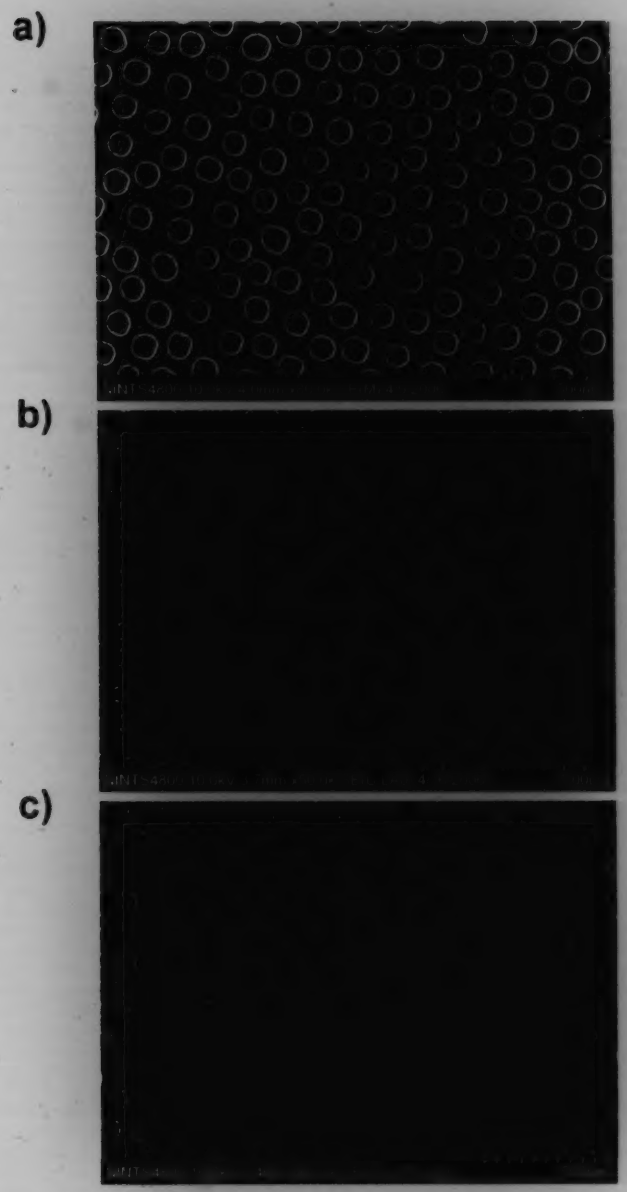

Figure 2.14. Large scale SEM images of patterned etch pits on Si(100) (a), Si(111) (b), and Si(110) (c). The pattern is obtained using PS-*b*-P4VP (M_n=128400-*b*-33500 g/mol) as templates and 0.01% HF (aq) as etchant for 40 min.

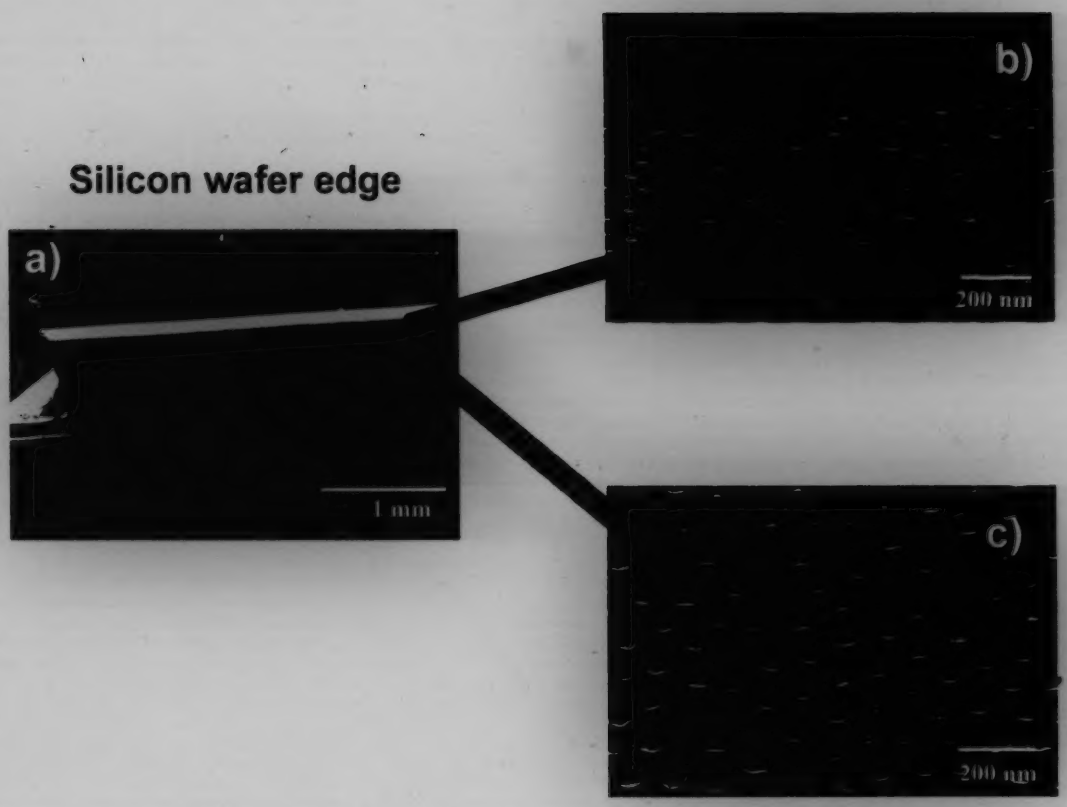

Figure 2.15. Patterning the curved silicon wafer edge using block copolymer templated etching process. (a) SEM image of the silicon wafer edge. (b) and (c) SEM images of the etch pits obtained from different sites on the silicon (111) wafer edge. PS-*b*-P4VP (M_n=128400-*b*-33500 g/mol) micelles were used as template. The etching time is 10 min.

2.3 Conclusions

In conclusion, block copolymer-directed silicon surface etching is demonstrated, using straightforward aqueous fluoride-based chemical etchants. Through modulation of the etching conditions (time, fluoride concentration, silicon wafer orientation, etc), shape, size and morphology of the resulting etch pits can be controlled. The protonated polypyridinium fluoride works as an anisotropic etchant in the system. The block copolymer templated etching proceeds on Si wafers with different orientations and dopant levels and even on curved surfaces, with the exception of highly doped p++ wafers, which could be used as an etch stop in future device design. Because fluoride etching of silicon results in hydride termination, the etch pit interiors are chemically distinct from the top face of the silicon wafer, rendering it possible to construct functionalized three-dimensional etched nanostructures on the wafer. The chemical functionality of the etch pit array will be discussed in the following chapter.

2.4 Experimental Section

Materials and instrumentation. Hydrofluoric acid (HF, semiconductor grade) was purchased from J. T. Baker. Asymmetric diblock copolymers of polystyrene-*block*-poly(4-vinylpyridine), denoted throughout the paper as PS-*b*-P4VP, with different molecular weights were purchased from Polymer Source Inc. (www.polymersource.com). The 56% (aq) w/w solution of pyridinium fluoride was prepared by mixing equal volumes of 49% HF (aq) and pyridine (Caledon Laboratories Ltd., 99%). All other chemicals and reagents were obtained from Aldrich and used as received. High purity

Millipore water (18 MΩcm, Barnstead Nanopure water) was used for all experiments. Atomic Force Microscopy (AFM) was performed with a Nanoscope IV (Veeco, USA) instrument in tapping mode, under ambient conditions. SSS (supersharp silicon) probes with a 2 nm radius of curvature (Nanosensors) were used for measurements of the depth distribution. Ellipsometry (Gaertner Scientific Corporation) was used for the measurements of the thicknesses of the block copolymer films on the silicon surface. Scanning electron microscopy (SEM) was carried out on a Hitachi S-4800 FE-SEM.

Silicon wafer preparation. Prime-grade 150 mm diameter n-type Si(100) (0.008-0.02 Ω•cm), Si(111) (0.0011-0.0015 Ω•cm), and Si(110) (4-7 Ω•cm) wafers were diced by hand into 1 cm^2 square shards. The silicon shards were initially degreased with a common dish soap solution and then cleaned with piranha solution at 80 °C for 30 min (Piranha solution = H_2SO_4: H_2O_2=3:1, v/v. Note: Piranha solution reacts violently with organics. Special precaution should be made when working with this mixture). All silicon shards were thoroughly rinsed with Millipore water after each cleaning step and blown dry with a stream of nitrogen prior to use.

Thin films of diblock copolymers. PS-*b*-P4VP was dissolved in toluene and heated at 70 °C for 45 min to produce a 3–6 mg/mL solution, and allowed to cool. Thin PS-*b*-P4VP films were prepared by spin-coating the prepared polymer solution, at room temperature, onto the as-cleaned silicon shards at 2500-3500 rpm.

Fabrication of etch pit arrays. The typical synthetic procedure is as follows. As-prepared silicon shards coated with a monolayer of PS-*b*-P4VP were dipped into the HF (aq) solution [concentration range, from 0.01%-10% (aq)] for the designated time. The shards were then removed from the HF (aq) solution and dried with a stream of nitrogen

gas. The block copolymer was then removed by ultrasonication in neat toluene for 5 min, and the ordered etch pits were characterized by SEM and AFM.

References

1 Xia, Y.; Rogers, J. A.; Paul, K. E.; Whitesides, G. M. *Chem. Rev.* **1999**, *99*, 1823.

2 Barth, J. V.; Costantini, G.; Kern, K. *Nature* **2005**, *437*, 671.

3 The ITRS Roadmap, found at http://www.itrs.net under 'reports'.

4 Guarini, K. W.; Black, C. T.; Zhang, Y.; Kim, H.; Sikorski, E. M.; Babich. I. V. *J. Vac. Sci. Technol. B* **2002**, *20*, 2788.

5 Black, C. T. *Appl. Phys. Lett.* **2005**, *87*, 163116.

6 Hawker C. J.; Russell, T. P. *MRS Bull.* **2005**, *30*, 952.

7 (a) Glass, R.; Möller, M.; Spatz, J. P. *Nanotechnology* **2003**, *14*, 1153. (b) Kästle, G.; Boyen, H. G.; Weigl, F.; Lengl, G.; Herzog, T.; Ziemann, P.; Riethmüller, S.; Mayer, O.; Hartmann, C.; Spatz, J. P.; Möller, M.; Ozawa, M.; Banhart, F.; Garnier, M. G.; Oelhafen, P. *Adv. Func. Mater.* **2003**, *13*, 853. (c) Spatz, J. P.; Mössmer, S.; Hartmann, C.; Möller, M.; Herzog, T.; Krieger, M.; Boyen, H. G.; Ziemann, P.; Kabius, B. *Langmuir* **2000**, *16*, 407. (d) Spatz, J. P.; Herzog, T.; Mössmer, S.; Ziemann, P.; Möller, M. *Adv. Mater.* **1999**, *11*, 149.

8 La, Y. H.; Edwards, E. W.; Park, S. M.; Nealey, P. F. *Nano Lett.* **2005**, *5*, 1379.

9 (a) Mansky, P.; Chaikin, P.; Thomas, E. L. *J. Mater. Sci.* **1995**, *30*, 1987. (b) Cheng, J. Y.; Ross, C. A.; Chan, V. Z.-H.; Thomas, E. L.; Lammertink, R. G. H.; Vancso, G. J. *Adv. Mater.* **2001**, *13*, 1174. (c) Cheng, J. Y.; Ross, C. A.; Thomas, E. L.; Smith, H. I.; Vancso, G. J. *Appl. Phys. Lett.* **2002**, *81*, 3657.

10 Park, M.; Harrison, C.; Chaikin, P. M.; Register, R. A.; Adamson, D. H. *Science*, **1997**, *276*, 1401.

11 Antonietti, M.; Göltner. C. *Angew. Chem. Int. Ed.* **1997**, *36*, 910.

12 Hamley, I. W. *Angew. Chem. Int. Ed.* **2003**, *42*, 1692.

13 Aizawa, M.; Buriak, J. M. *J. Am. Chem. Soc.* **2005**, *127*, 8932.

14 Lin, Z. Q.; Kim, D. H.; Wu, X. D.; Boosahda, L.; Stone, D.; LaRose, L.; Russell, T. P. *Adv. Mater.* **2002**, *14*, 1373.

15 Yang, X. M.; Xiao, S. G.; Liu, C.; Pelhos, K.; Minor, K. *J. Vac. Sci. Technol. B.* **2004**, *22*, 3331.

16 Stoykovich, M. P.; Müller, M.; Kim, S. O.; Solak, H. H.; Edwards, E. W.; de Pablo, J. J.; Nealey, P. F. *Science* **2005**, *308*, 1442.

17 Mansky, P.; Liu, Y.; Huang, E.; Russell, T. P.; Hawker, C. *Science* **1997**, *275*, 1458.

18 Black, C. T.; Guarini, K. W.; Zhang, Y.; Kim, H. J.; Benedict, J.; Sikorski, E.; Babich, I. V.; Milkove, K. R. *IEEE Electron Device Lett.* **2004**, *25*, 622.

19 Cheng, J. Y.; Ross, C. A.; Chan, V. Z.-H.; Thomas, E. L.; Lammertink, R. G. H.; Vancso, G. J. *Adv. Mater.* **2001**, *13*, 1174.

20 Aizawa, M.; Buriak, J. M. *J. Am. Chem. Soc.* **2006**, *128*, 5877.

21 Monk, D. J.; Soane, D. S.; Howe, R. T. *Thin Solid Films* **1993**, *232*, 1.

22 Lehmann, V. *Electrochemistry of Silicon: Instrumentation, Science, Materials and Applications* (Wiley-VCH, New York, 2002).

23 Higashi, G. S.; Chabal, Y. J.; Trucks, G. W.; Raghavachari, K. *Appl. Phys. Lett.* **1990**, *56*, 656.

24 Qiao, Y. H.; Wang, D.; Buriak, J. M. *Nano Lett.* **2007**, *7*, 464.

25 Förster, S.; Zisenis, M.; Wenz, E.; Antonietti, M. *J. Chem. Phys.* **1996**, *104*, 9956.

26 Resnik, D.; Vrtacnik, D.; Amon, S. *J. Micromech. Microeng.* **2000**, *10*, 430.

27 Resnik, D.; Vrtacnik, D.; Aljancic, U.; Amon, S. *J. Micromech. Microeng.* **2003**, *13*, 26.

28 Sato, K.; Shikida, M.; Matsushima, Y.; Yamashiro, T.; Asaumi, K.; Iriye, Y.; Yamamoto, M. *Sensors Actuators A* **1998**, *64*, 87.

29 Bäcklund, Y.; Rosengren, L. *J. Micromech. Microeng.* **1992**, *2*, 75.

30 Seidel, H.; Csepregi, L.; Heuberger, A; Baumgärtel, H. *J. Electrochem. Soc.* **1990**, *137*, 3612.

31 Chang, S-C.; Hicks, D. B. *J. Micromech. Microeng.* **1991**, *1*, 25.

32 Tokoro, K.; Uchikawa, D.; Shikida, M.; Sato, K. **1998** *INTERNATIONAL SYMPOSIUM ON MICROMECHATRONICS AND HUMAN SCIENCE.*

33 Garcia, S. P.; Bao, H.; Manimaran, M.; Hines, M. A. *J. Phys. Chem. B* **2002**, *106*, 8258.

34 Hines, M. A. *Annu. Rev. Phys. Chem.* **2003**, *54*, 29.

35 Faggin, M. F.; Green, S. K.; Clark, I. T.; Queeney, K. T.; Hines, M. A. *J. Am. Chem. Soc.* **2006**, *128*, 11455.

36 Neuwald, U.; Hessel, H. E.; Feltz, A.; Memmert, U.; Behm, R. J. *Surf. Sci.* **1993**, *296*, L8.

37 Thanh, V. L.; Bouchier, D.; Débarre, D. *Phys. Rev. B* **1997**, *56*, 10505.

38 Hessel, H. E.; Feltz, A.; Memmert, U.; Behm, R. J. *Chem. Phys. Lett.* **1991**, *186*, 275.

39 Allongue, P.; Kieling, V.; Gerischer, H. *Electrochimica Acta* **1995**, *40*, 1353.

40 Flidr, J.; Huang, Y.-C.; Newton, T. A.; Hines, M. A. *J. Chem. Phys.* **1998**, *108*, 5542.

41 Gosálvez, M. A.; Nieminen, R. M. *New J. Phys.* **2003**, *5*, 100.

42 Oosterbroek, R. E.; Berenschot, J. W.; Jansen, H. V.; Nijdam, A. J.; Pandraud, G.; van den Berg, A.; Elwenspoek, M. C. *J. Microelectromech. Syst.* **2000**, *9*, 390.

43 Famini, S.; Esfandyarpour, B.; Mohajerzadeh, S. *J. Electrochem. Soc.* **2006**, *153*, G721.

44 Sohn, B.-H.; Yoo, S.-I.; Seo, B.-W.; Yun, S.-H.; Park, S.-M. *J. Am. Chem. Soc.* **2001**, *123*, 12734.

45 Krishnamoorthy, S.; Pugin, R.; Brugger, J.; Heinzelmann, H.; Hoogerwerf, A. C.; Hinderling, C. *Langmuir* **2006**, *22*, 3450.

46 Collins, S. D. *J. Electrochem. Soc.* **1997**, *144*, 2242

47 Seidel, H.; Csepregi, L.; Heuberger, A.; Baumgartel, H. *J. Electrochem. Soc.* **1990**, *137*, 3626.

48 Jackman, R. J.; Brittain, S. T.; Adams, A.; Prentiss, M. G.; Whitesides, G. M. *Science* **1998**, *280*, 2091.

49 Erhardt, M. K.; Jin, H.-C.; Abelson, J. R.; Nuzzo, R. G. *Chem. Mater.* **2000**, *12*, 3306.

50 Xia, Y.; Kim, E.; Zhao, X.-M.; Rogers, J. A.; Prentiss, M.; Whitesides, G. M. *Science* **1996**, *273*, 347.

51 Xia, Y.; Whitesides, G. M. *Ang. Chem. Int. Ed.* **1998**, *37*, 550.

Chapter 3

Chemical Bifunctionality of Patterned Arrays of Nanoscale Pits and their Application for Selective Metal Deposition

3.1 Introduction

The fabrication of sub-micrometer and nanometer-scale surface patterns with multi-functionality has captured a great deal of interest and attention over the past several decades. By applying well-established chemistry in order to chemically pattern a surface, sophisticated structures have been developed with broad application potential in many emerging research areas such as sensors, biological recognition, electronic devices, and many others.[1,2,3,4,5] The development of new patterning techniques allows for the patterning of nanoscale features with controllable spacing and size, as well as functionality. Soft lithography and scanning probe microscopy (SPM) based lithography are two of the most popular techniques for chemical surface pattern fabrication in academic settings.[6,7] In soft lithography and dip-pen nanolithography, the ink molecules, which can be a variety of chemicals and biological molecules, are delivered to the surface in a patterned fashion with a topologically patterned elastomeric stamp, or with an SPM tip. An alternative way is to apply external stimuli such as a mechanical force or an electric field, to induce a local surface reaction and produce chemically patterned surface features.[8]

Block copolymer nanolithography is emerging as a promising and flexible technique to fabricate sub-100 nm surface patterns.[9,10] The distinct chemical properties

of the different components in a block copolymer provide great opportunities to induce surface chemical reactions in a spatially defined way. For example, block copolymer micelle arrays have been used to template surface galvanic displacement reactions and to produce ordered metal nanoparticle array on surfaces.[11,12] Recently, we developed an efficient method to obtain highly controlled and tailored nanoscale etch pits using self-assembled diblock copolymer monolayers as the template.[13] The intriguing feature of the obtained pattern is that the interior and exterior of the patterned surfaces have distinct chemical functionalities, that allow further surface modification for specific applications. As one of many possibilities, we demonstrated in this chapter that ordered noble metal nanocrystal arrays can be achieved by tailoring the surface chemistry of the initial nanoscale etch pits.

3.2 Results and Discussion

3.2.1 Fabrication of Ordered Etch Pits

A detailed experimental procedure to fabricate ordered etch pit arrays on silicon surfaces has been described in Chapter 2. Briefly, amphiphilic block copolymers, of the composition polystyrene-*block*-poly (4-vinyl pyridine), denoted by PS-*b*-P4VP, were used as a template to pattern silicon surfaces. When the concentration of the copolymer in the apolar solvent toluene is larger than the critical micelle concentration, they spontaneously form spherical micelles with a P4VP core and a PS shell because of the different solubility of the two blocks in toluene.[14] The micelles in solution phase are transferred onto the Si surface by spin coating and spontaneously self-assemble into

quasi-hexagonal arrays, which can be used as soft-masks for the subsequent etching process. By immersing the Si wafer coated with a monolayer of PS-*b*-P4VP micelles into an aqueous HF solution for the designated time and removing the polymer through 5 min of ultrasonication in neat toluene, we can obtain the corresponding ordered patterned etch pit array with the same periodicity as that of the parent copolymers monolayer (see Figure 3.1).

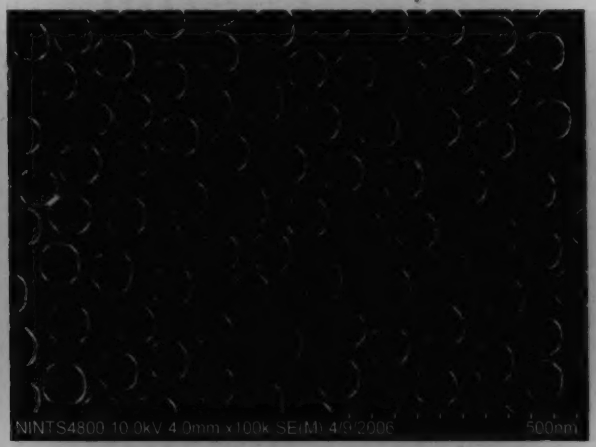

Figure 3.1. Patterned etch pit array on Si(100) obtained using PS-*b*-P4VP (M_n=128400-*b*-33500 g/mol) templated etching.

3.2.2 Chemical Functionality of Patterned Surface

As demonstrated in Chapter 2, block copolymer templated etching selectively took place beneath the P4VP cores area. The PS matrix in the copolymer film prevents contact of the HF etching solution with the native oxide on the silicon surfaces, leading to exclusive etch pit formation under the P4VP cores; the top unetched silicon surface should therefore remain oxide terminated. Because fluoride-based etching of Si yields

surface-bound Si-H_x groups, the walls of the etch pits would be expected to be hydride-terminated. As a result, selective functionalization either inside the etch pits or on the top oxide surface should be achievable, assuming that the etching process is indeed as selective as postulated. Precise control over the chemistry of the internal environment of the etch pits would enable, for instance, selective functionalization, growth, and isolation of nanoscale materials and immobilization of individual biomolecules.

Germanium attenuated total reflection (GATR) Fourier-transform infrared spectroscopy (FTIR) was employed to characterize the chemical functionalities of the etch pit array.[15] As shown in Figure 3.2a, a Si(100) surface etched with 1% HF (aq) through a PS-*b*-P4VP monolayer has both non-oxidized and oxygen back-bonded (Si-H_x) modes centered around 2100-2200 cm^{-1}. The two modes would be expected, as there are at least two populations of Si-H_x groups, one near the oxide interface and the other on the nonoxidized Si-H_x terminated etch pit interior. The spectrum of the wafer after the immersion of the same freshly patterned Si wafer into a 1% HF aqueous solution for 6 min is presented in Figure 3.2b. The increase of the intensity of ν(Si-H_x) centered around ~2100-2200 cm^{-1} indicates the much greater level of Si-H_x coverage as compared to that of Figure 3.2a. This is reasonable because the native oxide layer on the flat surface of etch pit array was etched away by HF (aq), rendering the whole surface hydride-terminated.

The FTIR data do not provide any spatial information as to the location of the Si-H_x groups. The bifunctionality of the patterned surface can, however, be clearly demonstrated via parallel functionalization methods, showing that selective chemical reactivity can take place within the etch pits, or, if desired, outside of them. We use

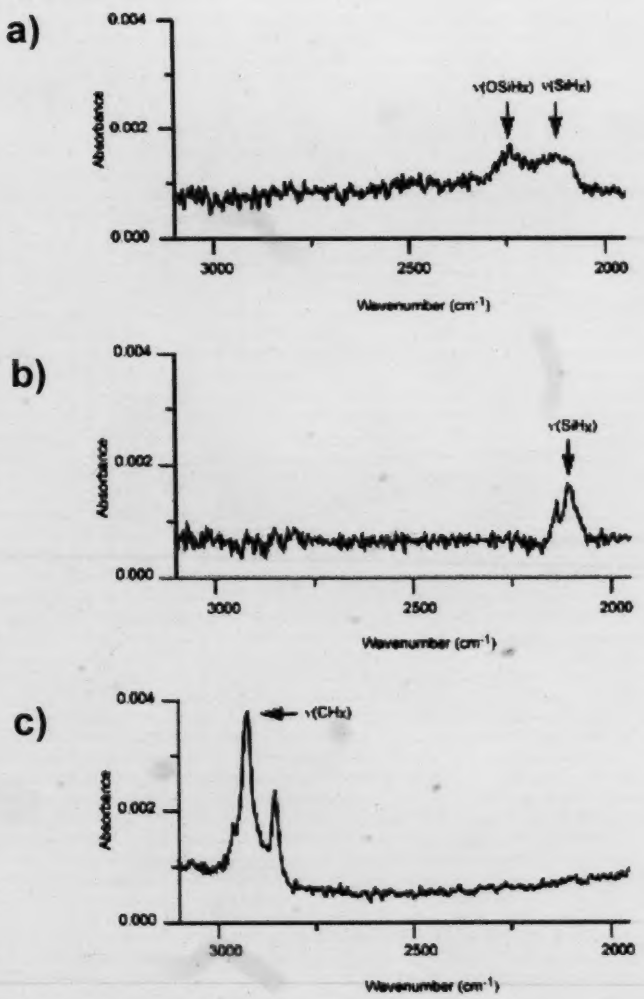

Figure 3.2. GATR-FTIR spectra of etch pit array. (a) Freshly patterned Si surface. (b) After dipping the freshly patterned Si surface into the HF (aq) solution to remove native oxide layer. (c) After functionalizing the fresh patterned surface through thermal hydrosilylation of octadecyne.

galvanic displacement and silicon hydrosilylation to establish the surface functionalities of the patterned etch pit array.

Galvanic displacement reactions, widely studied as a means to deposit metals on semiconductor surfaces, occur spontaneously on H-terminated Si surfaces, and not on the insulating oxide interface.[16,17,18] Figure 3.3 shows the schematic diagram of galvanic displacement of a noble metal on a silicon surface. In a typical galvanic displacement process, the metal ions in the solution phase are reduced by the electrons from the bonding electrons of the substrate lattice (valence band), resulting in the formation of metal films or particles on the surface. The donation of electrons from the substrates accompanies the oxidation of substrate, which causes the formation of a thin layer of SiO_x in the case of Si substrate. Although the detailed mechanism of galvanic displacement is not fully understood, mixed potential theory provides a useful tool to predict reactivities of metal/substrate systems.[19] Metal ions with reduction potentials higher than the oxidation potential of Si to SiO_x can form deposited metal. As shown by the half potential equation in Figure 3.3, $HAuCl_4$ can spontaneously deposit on Si surfaces in the absence of any external electron source because the overall cell potential is positive. Immersion of an H-terminated silicon surface in a sufficiently oxidizing metal salt solution, such as Ag^+ (aq) or $HAuCl_4$ (aq), results in electron transfer from the Si(s) to the metal salt, bringing about metal deposition on silicon. On the other hand, oxide inhibits electron transfer, and thus little or no metal deposition occurs on silicon oxide. Deposition proceeds until the dielectric SiO_x layer blocks the electron transfer process.

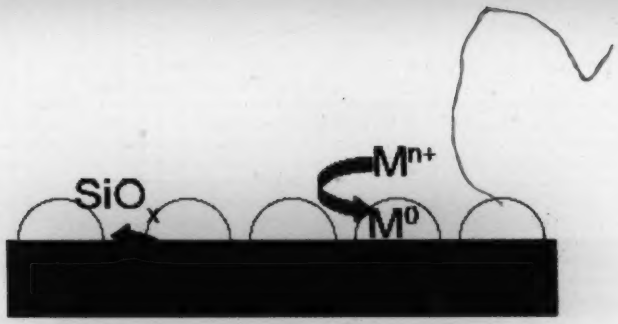

$AuCl_4^- + 3e^- \longrightarrow Au + 4Cl^-$ $E^o = 1.002$ V

$SiO_2 + 4H^+ + 4e^- \longrightarrow Si + 2H_2O$ $E^o = -0.857$ V

Figure 3.3. Schematic diagram of the galvanic displacement reaction of metal on Si surfaces. The standard electrode potentials shown are with respect to the normal hydrogen electrode.

Another unique surface chemistry of a hydride-terminated Si surface used in the present study is hydrosilylation on surfaces.[20] Hydrosilylation is the one of the most direct means to produce Si-C bonds in organosilane chemistry. Because of the covalent nature of the surface Si-H bond, the hydride-terminated silicon can be modified by reaction with unsaturated terminal alkenes or alkynes to form covalently bonded organic monolayers in a similar way, compared with solution phase organometallic chemistry. The formation of organic monolayers improves the surface stability against etching and oxidation and, more importantly, provides useful functional groups with which to interface silicon with other interesting chemical and biological systems to build hybrid structures. Silicon surface hydrosilylation reaction can be activated by a number of different methods such as high temperature, UV irradiation, chemical radical initiators and others.[21, 22, 23] Figure 3.4 shows a radical mechanism involved in the thermohydrosilylation of alkene on hydride-terminated surface.[24] The thermo-activated surface silicon radicals can add across the unsaturated alkene or alkyne groups to form Si-C bonds. The resulting β-carbon radical abstracts a hydrogen atom from a

neighboring silicon to propagate the chain reaction and afford the organic monolayer formation.

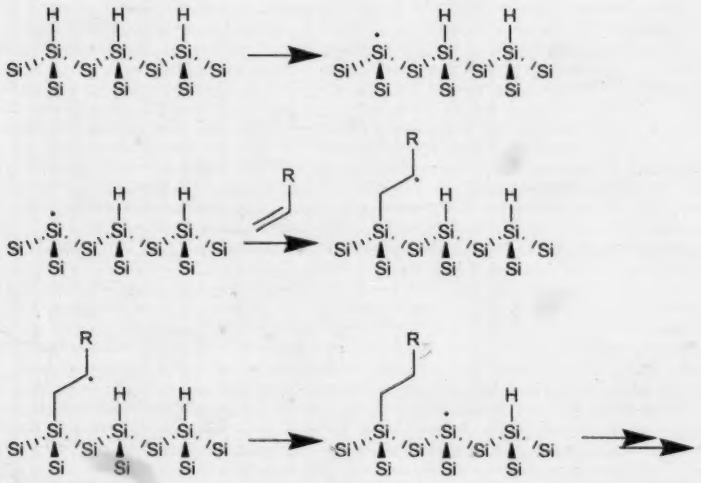

Figure 3.4. Radical mechanism of thermohydrosilylation of alkene on hydride-terminated silicon surface.

Three different experiments are designed to establish the chemical functionalities of the array of etch pits. In the first experiment, a freshly patterned Si(100) wafer, following removal of the block copolymer, was immersed in a $HAuCl_4$ (10^{-4} M) ethanolic solution (H_2O: ethanol=1:1, v/v) for 5 min, as shown schematically in Figure 3.5. The sample was removed from the solution and then rinsed thoroughly with ethanol and water. As expected, strongly adhering nanoparticles of Au(0) grow selectively inside the etch pits with no metal observed on the exterior, as shown in Figure 3.6. The selective occurrence of galvanic displacement demonstrates the obvious difference in chemical reactivity between the etch pit interior and the flat top surface due to the distinct

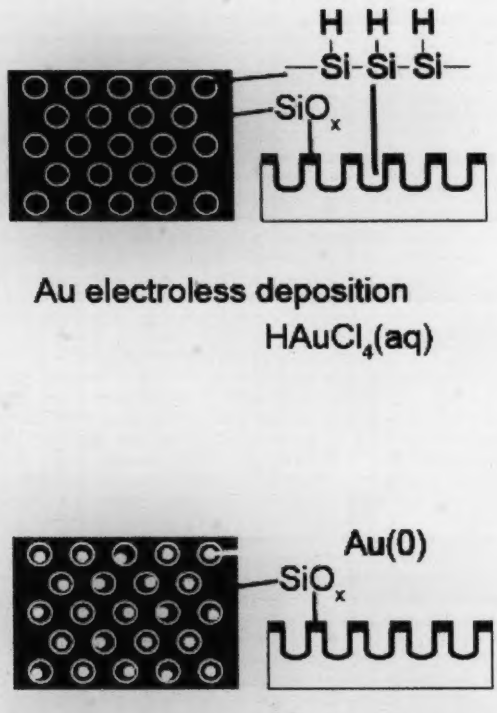

Figure 3.5. Schematic diagram of selective metal deposition inside the etch pits

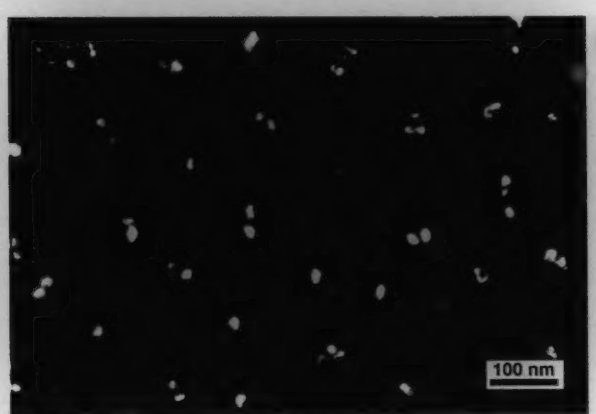

Figure 3.6. SEM image of gold nanoparticles in the etch pit array through a galvanic displacement process.

functionalities - hydride versus oxide. In addition, the patterned surface with the gold nanoparticles deposited inside the etch pits is further characterized by scanning Auger microscopy (SAM). Figure 3.7a is a SEM image of the gold deposition inside the etch pits. The average size of the deposited gold particles is about 45 nm. Figures 3.7b and c show the Auger maps of silicon and gold on the same scan area corresponding to that of the SEM image; silicon (yellow green) and gold (green) are clearly visualized with very good spatial resolution. Figure 3.7d is the overlapped image of a, b and c, in which the green color represents the gold, and the blue color the silicon. The Auger maps unquestionably identify the composition of the deposited nanoparticles on the silicon surface to be gold. Figure 3.7f shows a SAM line profile along the red color line marked in Figure 3.7e. The expected relative concentration of gold and silicon along the line is clearly seen.

The Si-H_x-terminated etch interiors can also be functionalized via hydrosilylation of a long chain alkyne, producing Si-alkenyl groups. Figure 3.8a outlines the procedure to hydrosilylate the Si(100) etch pit interiors, prepared as described for Figure 3.1a, with 1-octadecyne, via a short thermal reaction to produce covalently bonded 1-octadecenyl groups. The presence of $\nu(C\text{-}H_x)$ at 2800-3000 cm^{-1} in the GATR IR spectrum (Figure 3.2c), following hydrosilylation, indicates the formation of organic monolayer. Rinsing with a 1% HF (aq) solution to remove all native oxide on the top layer of the silicon transforms this interface into an Si-H_x-terminated surface. Immersion of this silicon wafer into an $HAuCl_4$ (10^{-5} M) ethanolic solution (H_2O: ethanol = 1:1, v/v) for 5 min leads to metal deposition exclusively on the top of the silicon wafer, and not within the etch pit interiors (Figure 3.9). The 1-octadecenyl layer is insulating, preventing electron

transfer from Si(s) to the Au(III) salt, and thus gold deposition is hindered within the functionalized etch interior.

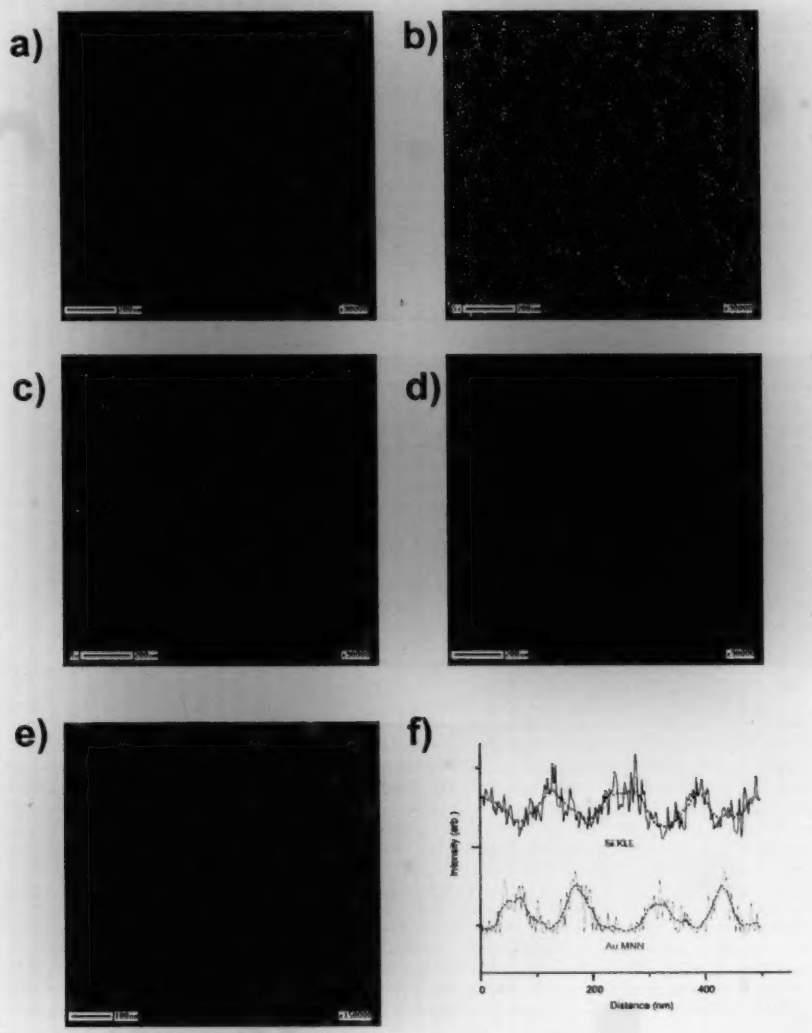

Figure 3.7. Scanning Auger microscopy (SAM) images of Au nanocrystals on the etch pit array obtained by galvanic displacement. (a) SEM image. (b) Si KLL SAM. (c) Au MNN SAM. (d) The overlapping images of (a), (b) and (c). (e+f) SAM line profiles of Si KLL (top) and Au MNN (bottom) along the red line marked in the SEM image (e) shown in (f). The scale bars are 200 nm in (a-d) and 100 nm in (f), respectively.

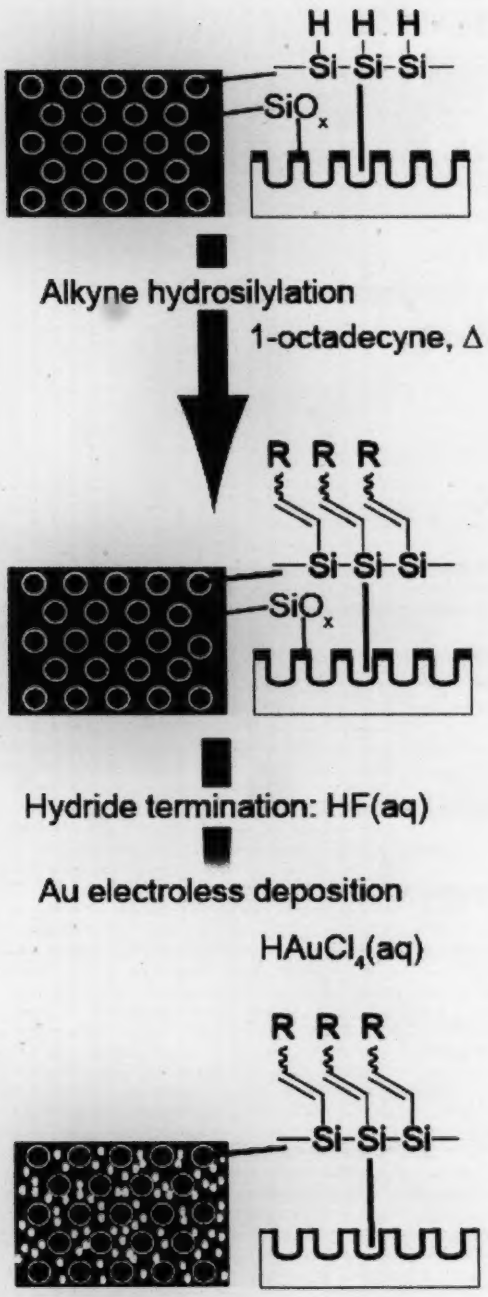

Figure 3.8. Schematic diagram for the controlled decoration of gold nanoparticles on the flat top surface of the etch pit array.

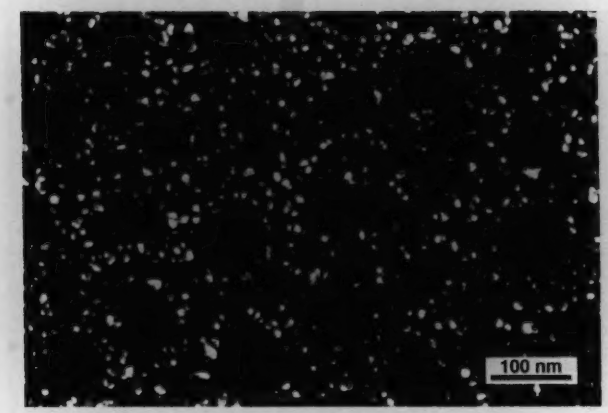

Figure 3.9. SEM image of selective decoration of the flat top surface of the etch pit array with gold nanoparticles.

As a control experiment, outlined in Figure 3.10, the freshly patterned and etched Si(100) wafer was entirely terminated with Si-H_x groups by dipping in 1% HF (aq) - both the etch pit interiors and the top face of the silicon wafers are hydride-terminated. Exposure of this chemically homogeneous surface to the $HAuCl_4$ (10^{-5} M) ethanolic solution (H_2O: ethanol = 1:1, v/v) for 5 min leads to deposition in all regions, as shown in Figure 3.11.

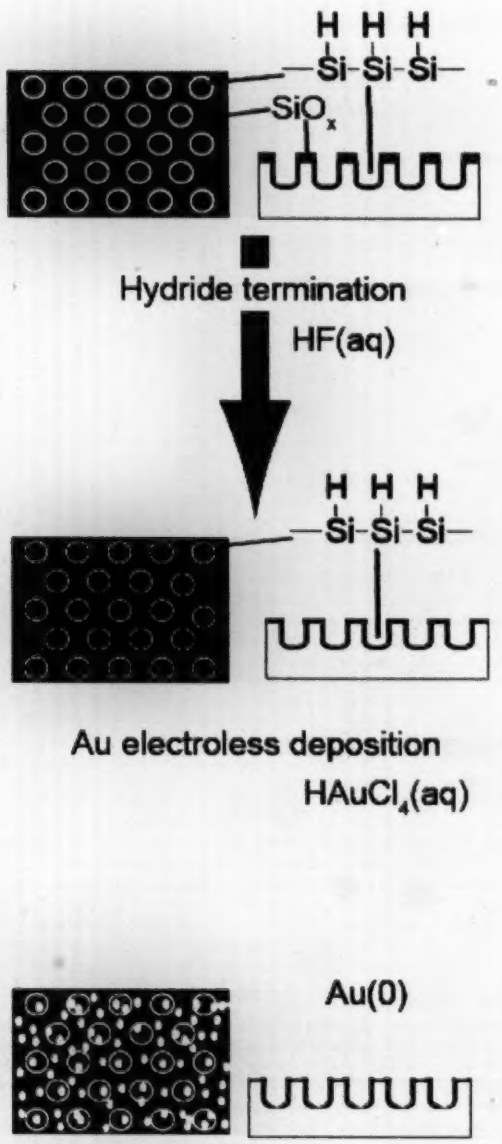

Figure 3.10. Schematic diagram for the formation of gold nanoparticles over the entire etch pit array (on top flat surface and within the pits).

Figure 3.11. SEM image of gold nanoparticles decorating the entire etch pit array, following the experiment process outlined in Figure 3.10.

3.2.3 Fabrication of Nanocrystal Arrays from Etch Pits

Anisotropic nanoparticles show unique properties relative to isotropic spherical particles, and have promising applications in photonics, nanoelectronics, bioanalytical, biomedical engineering and chemical imaging.[25,26,27] The synthesis of anisotropic metal particles in solution phase has been well studied.[28] The assembly, however, of anisotropic nanoparticles into ordered arrays, which is not only very important for future applications but also, more intriguingly, may display unique properties,[29,30,31] is still a big challenge. As shown above, we have demonstrated that the chemical functionalities of the interior and exterior surfaces of the etch pits are hydride-terminated silicon and silicon with native oxide, respectively. We will show in this section it is possible to fabricate nanoparticle arrays by tailoring the chemical functionalities of the etch pits.

In the first procedure, the nanoparticles inside the etch pits obtained by galvanic displacement of gold, as shown in Figure 3.7, were used as seeds for the growth of the

nanoparticles. The as-prepared sample containing gold seeds within the pores was then introduced to a gold growth solution containing an anisotropic directing agent, as is used for the growth of nanocrystals in solution phase. After the final rinsing step, an ordered nanocrystal array with the same periodicity as that of the etch pit array is obtained (Figure 3.12).

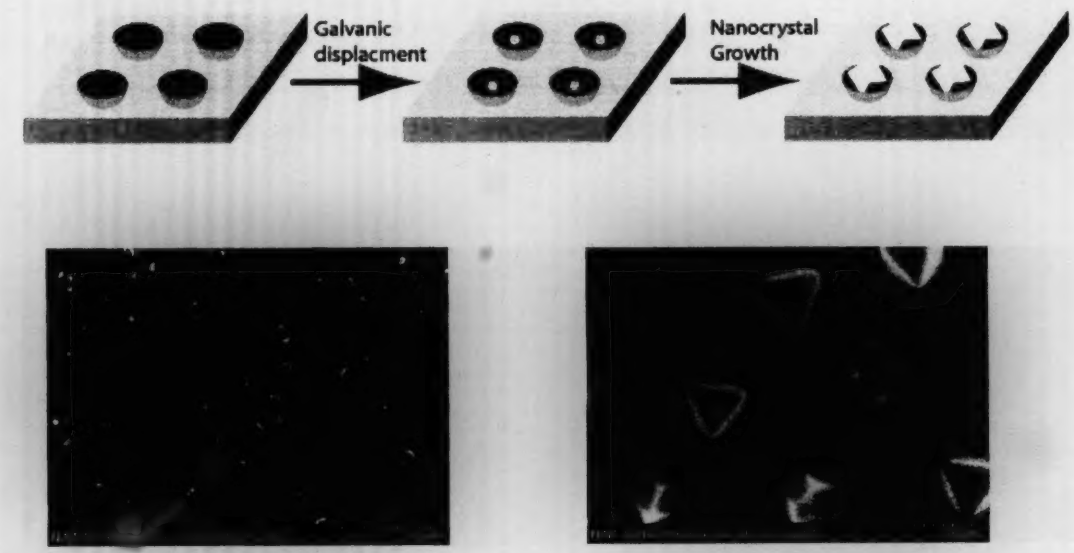

Figure 3.12. Gold nanoparticles grown from the etch pit array.

In the second attempt, the freshly prepared patterned surface is modified by UV-induced hydrosilylation with 4-vinylpyridine.[32] The pyridine group is expected to localize within the interior walls of the etch pits because the surface is hydride-terminated. After dipping the modified sample into the solution of Ag nanoprisms synthesized following the literature method,[33] as shown in Figure 3.13, the nanoprisms are trapped in

the etch pits to form an array with the same periodicity as that of the etch pits, through Ag-N bonds between Ag nanoprisms and the nitrogen in the pyridine groups (Figure 3.13). The control experiment was carried out on the freshly patterned surface without the modification with 4-vinylpyridine, which was directly dipped into the same Ag nanoprism solution as above. As can be seen from Figure 3.13c, there are no Ag nanoprisms captured within the etch pits except several physically adsorbed Ag nanocrystals on the surface.

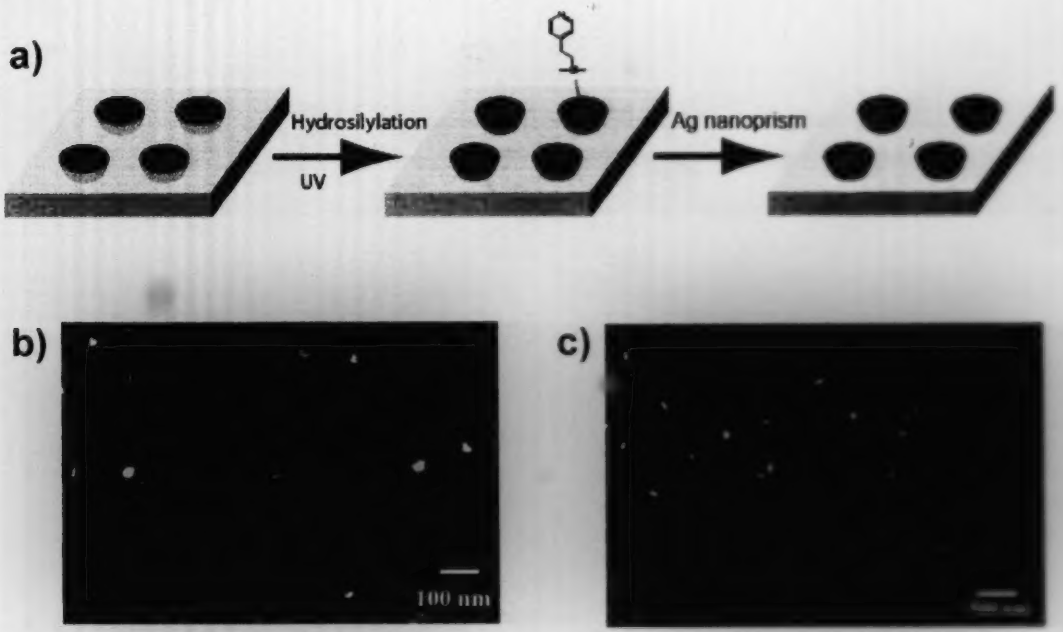

Figure 3.13. (a) Schematic diagram for the capture of Ag nanoprisms within the etch pits. (b) SEM image of capture of Ag nanoprisms into an etch pit array functionalized by hydrosilylation with 4-vinyl pyridine. (c) SEM image of the control experiment done on an etch pit array without the modification with 4-vinyl pyridine.

3.3 Conclusions

In this chapter, we have characterized the chemical functionalities of the etchpit array obtained using block copolymer assembly templated etching on silicon. Because fluoride etching of silicon results in hydride termination, the etch pit interiors are chemically distinct from the top face of the silicon wafer. As one of many possibilities, we demonstrate here the construction of metal nanoparticle arrays with controllable spatial distribution on the surface, utilizing galvanic displacement and thermohydrosilylation of a hydride-terminated silicon surface. Because the surface chemistry of silicon surfaces is now so diverse, the possibilities to interface a wide variety of functional molecules and structures both within the etch pit and on the top face, are endless.

3.4 Experimental Section

Materials and instrumentation. Hydrofluoric acid (HF) was purchased from J. T. Bakers. Asymmetric diblock copolymers of PS-*b*-P4VP were purchased from Polymer Source Inc. Alkene or alkyne (Aldrich) used for hydrosilylation were purified by distillation and stored in refrigerator in nitrogen filled glovebox. All other chemicals and reagents were obtained from Aldrich and used as received. High purity Millipore water (18 MΩ·cm, Barnstead Nanopure water) was used throughout the experiment. Scanning electron microscopy (SEM) was carried out on Hitachi S-4880 FE-SEM. Fourier transform infrared (FTIR) spectra were collected using a Germanium attenuated total reflection (GATR) attachment from Harrick Scientific Products Inc. with 512 scans at 4

cm^{-1} resolution. Scanning Auger microscopy images were obtained from JAMP-9500F Field Emission Scanning Auger Microprobe (JEOL Ltd.).

Cleaning of silicon wafer. Prime-grade 150 mm diameter Si (100) and (111) wafers were cut into 1 by 1 cm^2 shards. The silicon shards were initially degreased with common dish soap solution and then cleaned with a piranha solution (H_2SO_4: H_2O_2=3:1, v/v) (note: *very dangerous. Special precaution should be paid*) at 80 °C for 30 min. All the Si substrates were thoroughly rinsed with Millipore water after each cleaning step and blown dry by the stream of nitrogen prior to use.

Fabrication of etch pits arrays. PS-*b*-P4VP was dissolved in toluene at 70 °C to produce 3 mg/mL solution. Thin films of copolymer were prepared by spin-coating polymer solution onto the as-cleaned Si shards. As-prepared Si shards coated with PS-*b*-P4VP was dipped into 1% HF aqueous solution for 10 min, then removed from the solution and dried with the nitrogen gas. After removing copolymer with toluene, the ordered etch pits were obtained and used for chemical functionalization or metal deposition.

Hydrosilylation of nanopatterned surface. Thermo-hydrosilylation of 1-octadecyne on the patterned silicon surface was carried out by immersing the freshly prepared patterned silicon substrate into the solution of 1-octadecyne in mesitylene (v/v=1:3) and heated under argon atmosphere at 190°C for 3 h. The substrate was then removed from the reaction solution, cleaned thoroughly with hexane and dichloromethane and dried with nitrogen.

Deposition of noble metal nanoparticles. The selective deposition of metal nanoparticles was carried out to study the chemical functionality of nanopattern Si surface. Three different experiment procedures were employed.

Method A. First, as-prepared patterned Si substrate after removing polymer was immersed into $HAuCl_4$ (10^{-4} M) ethanolic solution (H_2O: ethanol=1:1, v/v) for designated time.[34] The sample was removed from the solution and then rinsed thoroughly with ethanol and water. The gold nanoparticles were deposited into the interior of the etch pits.

Method B. The silicon wafer with the 1-octadecenyl modified etch pit interiors was dipped into 1% HF aqueous solution for 5 min. The wafer was moved out from the solution, rinsed thoroughly with water, and then dipped into the $HAuCl_4$ (10^{-5} M) ethanolic solution (H_2O: ethanol = 1:1, v/v) for 5 min. The wafer was rinsed with ethanol and water and dried by the stream of nitrogen prior to characterization.

Method C. In the control experiment, the freshly prepared silicon wafer with patterned etch pits was dipped into the 1 % HF aqueous solution for 6 min to remove the native oxide layer on the walls surrounding the nanopores. And then the same wafer was immersed into $HAuCl_4$ (10^{-4} M) ethanolic solution for designated time, removed from the solution, thoroughly rinsed with ethanol and Millipore water and dried with nitrogen gas.

Fabrication of metal nanocrystal array. The small gold nanoparticles obtained by electroless deposition inside the etch pits could be used as crystal seeds for the further growth of the gold nanocrystals. The method can be referred to references 35&36. In a typical procedure, 1 mL $HAuCl_4$ (4×10^{-4} M) solution, 0.1 mL $AgNO_3$ (10^{-5} M) and 1 mL ascorbic acid (6.4×10^{-4} M) were added into a 7 mL CTAB (1.6×10^{-2} M) solution and followed by immersing the patterned substrate with gold seeds into this mixed

solution. The reaction solution stood for overnight. Then Si substrate was moved out and rinsed with copious ethanol and Millipore water and blown dry with nitrogen for further characterization.

Fabrication of Ag nanoprism array. The freshly prepared etch pit array is transferred into nitrogen-filled glovebox and immersed into a vial with neat 4-vinyl pyridine. After a UV irradiation process for 30 min, the wafer was then removed from the reaction solution, cleaned thoroughly with hexane and dichloromethane and dried with nitrogen. The modified etch pits array was taken out of the glovebox and immersed into an aqueous solution of Ag nanoprisms, which was fabricated following the literature process. The substrate was moved out after 20 min and rinsed with copious ethanol and Millipore water and blown dry with nitrogen for further characterization.

References

1 (a) Iwata, P.; Suk-In, P.; Hoven, V. P.; Takahara, A.; Akiyoshi, K.; Iwasaki, Y. *Biomacromolecules*, **2004**, *5*, 2308. (b) Brock, A.; Chang, E.; Ho, C.-C.; LeDuc, P.; Jiang, X.; Whitesides, G. M.; Ingber, D. E. Langmuir, 2003, 19, 1611. (c) Jiang, X. Y.; Bruzewicz, D. A.; Wong, A. P., Piel M., Whitesides G. M. *Proc. Natl. Acad. Sci.* **2005**, *102*, 975.

2 (a) Blawas, A. S.; Reichert, W. M. *Biomater.* **1998**, *19*, 595. (b) Whitesides, G. M.; Ostuni, E.; Takayama, S.; Jiang, X. Y.; Ingber, D. E. *Annu. Rev. Biomed. Eng.* **2001**, *3*, 335.

3 (a) Werne, T. A. V.; Germack, D. S.; Hagberg, E. C.; Sheares, V. V.; Hawker, C. J.; Carter, K. R. *J. Am. Chem. Soc.*, **2003**, *125*, 3831. (b)Xu, F. J.; Kang, E. T.; Neoh, K. G. *J. Mater. Chem.* **2006**, *16*, 2948. (c) Tu, H.; Heitzman, C. E.; Braun, P. V. *Langmuir*, **2004**, *20*, 8313. (d) Jones, D. M.; Smith, J. R.; Huck, W. T. S.; Alexander, C. *Adv. Mater.*, **2002**, *14*, 1130.

4 Menard, E.; Park, J.; Jeon, S.; Shir, D.; Nam, Y.; Meitl, M.; Rogers, J. A. *Chem. Rev.* **2007**, *107*, 1117.

5 Stewart, M. E.; Anderton, C. R.; Thompson, L. B.; Maria, J.; Gray, S. K.; Rogers J. A.; Nuzzo, R. G. *Chem. Rev.* **2008**, *108*, 494.

6 Xia, Y.; Rogers, J. A.; Paul, K. E.; Whitesides, G. M. *Chem. Rev.* **1999**, *99*, 1823. (b) Xia, Y.; Whitesides, G. M. *Angew. Chem. Int. Ed. Engl.* **1998**, *37*, 551.

7 Ginger, D.S.; Zhang, H.; Mirkin, C.A. *Angew. Chem. Int. Ed.* **2004**, *43*, 30.

8 (a) Nyffenegger, R. M.; Penner, R. M. *Chem. Rev.* **1997**, *97*, 1195. (b) Kramer, S.; Fuierer, R. R.; Gorman, C. B. *Chem. Rev.* **2003**, *103*, 4367. (c) Liu, G.-Y.; Xu, S.; Qian, Y. *Acc. Chem. Res.* **2000**, *33*, 457-466.

9 Hamley, I. W. *Nanotechnology* **2003**, *14*, R39.

10 (a) Park, M.; Harrison, C.; Chaikin,P. M. Register, R. A.; Adamson, D. H. *Science* 1997, *276*, 1401. (b)Lin, Z.; Kim, D. H.; Wu, X.; Boosahda, L.; Stone, D.; LaRose, L.; Russell, T. P. *Adv. Mater.* **2002**, *14*, 1373. (c) Glass, R.; Moller, M.; Spatz, J. P. *Nanotechnology* **2003**, *14*, 1153.

11 (a) Aizawa, M.; Buriak, J. M. *J. Am. Chem. Soc.* **2005**, *127*, 8932. (b) Aizawa, M.; Buriak, J. M. *Chem. Mater.* **2007**, *19*, 5090.

12 Aizawa, M.; Buriak, J. M. *J. Am. Chem. Soc.* **2006**, *128*, 5877.

13 Qiao, Y.; Wang, D.; Buriak, J. M. *Nano Lett.* **2007**, *7*, 464

14 Spatz, J. P.; Herzog, T.; Mossmer, S.; Ziemann, P.; Moller, M. *Adv. Mater.* **1999**, *11*, 149.

15 (a) Milosevic, M.; Berets, S. L.; Fadeev, Y. *Appl. Spectros.*, 2003, 57, 4724. (b) Mulcahy, M. E.; Berets, S. L.; Milosevic, M.; Michl, J. *J. Phys. Chem. B*, 2004, 108, 1519.

16 (a) Porter, L. A.; Choi, H. C.; Ribbe, A. E.; Buriak, J. M. *Nano Lett.*, **2002**, *2*, 1067. (b) Porter, L. A., Jr.; Choi, H. C.; Schmeltzer, J. M.; Ribbe, A. E.; Elliott, L. C. C.; Buriak, J. M. *Nano Lett.* **2002**, *2*, 1369.

17 (a) Magagnin, L.; Maboudian, R.; Carraro, C. *J. Phys. Chem. B* **2002**, *106*, 401. (b) Gao, D.; He, R.; Carraro, C.; Howe, R. T.; Yang, P.; Maboudian, R. *J. Am. Chem. Soc.*, **2005**, *127*, 4574.

18 Oskam, G.; Long, J. G.; Natarajan, A.; Searson, P. C. *J. Phys. D* **1998**, *31*, 1927.

19 Okinaka, Y.; Osaka, T. *Adv. Electrochem. Sci. Eng.* **1994**, *3*, 55.

20 Buriak, J. M. *Chem. Rev.* **2002**, *102*, 1271.

21 (a) Cicero, R. L.; Linford, M. R.; Chidsey, C. E. D. *Langmuir* **2000**, *16*, 5688. (b) Terry, J.; Linford, M. R.; Wigren, C.; Cao, R.; Pianetta, P.; Chidsey, C. E. D. *Appl. Phys. Lett.* **1997**, *71*, 1056-1058.

22 Sieval, A. B.; Vleeming, V.; Zuilhof, H.; Sudhölter, E. J. *Langmuir* **1999**, *15*, 8288.

23 Wang, D.; Buriak, J. M. *Langmuir*, **2006**, *22*, 6214.

24 M. R.; Fenter, P.; Eisenberger, P. M.; Chidsey, C. E. D. *J. Am. Chem. Soc.* **1995**, *117*, 3145.

25 Jain, P. K.; Eustis, S.; El-Sayed, M. A. *J. Phys. Chem. B.* **2006**, *110*, 18243.

26 Narayanan, R.; El-Sayed, M. A. *J. Phys. Chem. B.* **2005**, *109*, 12663.

27 Link, S.; El-Sayed, M. A. *J. Phys. Chem. B.***1999**, *103*, 8410.

28 (a) Sun, Y. G.; Xia, Y. N. *Science* **2002**, *298*, 2176. (b) Jin, R. C.; Cao, Y. W.; Mirkin, C. A.; Kelly, K. L.; Schatz, G. C.; Zheng, J. G. *Science* **2001**, *294*, 1901. (c) Ahmadi, T. S.; Wang, Z. L.; Green, T. C.; Henglein, A.; El-Sayed, M. A. *Science* **1996**, *272*, 1924.

29 Caswell, K. K.; Wilson, J. N.; Bunz, U. H. F.; Murphy, C. J. *J. Am. Chem. Soc.* **2003**, *125*, 13914-13915.

30 Maier, S. A.; Kik, P. G.; Atwater, H. A.; Meltzer, S.; Harel, E.; Koel, B. E.; Requicha, A. A. G. *Nature Mater.* **2003**, 2, 229.

31 (a) Henzie, J.; Shuford, K. L.; Kwak, E.-S.; Schatz, G. C.; Odom, T. W. *J. Phys. Chem. B* **2006**, *110*, 14028. (b) Henzie, J.; Lee, M. H.; Odom, T.W. *Nature Nanotech.* **2007**, *2*, 549.

32 Xu, D.; Kang, E. T.; Neoh, K. G.; Zhang, Y.; Tay, A. A. O.; Ang, S. S.; Lo, M. C. Y.; Vaidyanathan, K. *J. Phys. Chem. B.* **2002**, *106*. 12508.

33 Metraux, G. S.; Mirkin, C. A. *Adv. Mater*. **2005**, *17*, 412.

34 Magagnin, L.; Maboudian, R.; Carraro, C. *J. Phys. Chem. B* **2002**, *106*, 401.

35 Sau, T. K.; Murphy, C. J. *J. Am. Chem. Soc.* **2004**, *126*, 8648.

36 Murphy, C. J.; Sau, T. K.; Gole, A. M.; Orendorff, C. J.; Gao, J.; Gou, L.; Hunyadi, S. E.; Li, T. *J. Phys. Chem. B.* **2005**, *109*, 13857.

Chapter 4

Fabrication of Ordered Nanoparticle Arrays on Silicon and their Surface Enhanced Raman Scattering Applications

4.1 Introduction

In the past 20 years, colloidal nanoparticles have attracted a great deal of attention due to potential applications in optics, electronics, photonic materials, sensors and catalysis.[1] The synthesis of nanoparticles with controllable size, shape, composition, and surface functionality has been achieved and their unique properties have been investigated. Recently, special attention has been paid to the design and construction of self-assembled noble metal nanoparticle arrays since they may possess unique physicochemical properties, which are different from those of bulk material and isolated single nanoparticles.[2] For example, the plasmonic band of a metal nanoparticle is strongly affected by the aggregation of the metal nanoparticles and this effect has been utilized for the trace analysis of DNA base pair mismatch.[3] A number of methods have been used to direct the deposition and organization of metal nanoparticles, including self-assembly, [4] electrostatic interactions, [5] air-water interface by Langmuir-Blodgett techniques,[6] electrophoretic deposition,[7] and evaporation.[8]

Surface enhanced Raman scattering (SERS) is an important physicochemical phenomenon observed on metal surfaces.[9,10] The Raman signal of adsorbed molecules on a rough metal surface can be enhanced by up to 10^{14}-10^{15},[11] and thus SERS has great potential for trace chem- or bio-analysis. SERS was first observed by Fleischman and

coworkers in 1974, where it is found that pyridine adsorbed on roughened silver would exhibit enhanced Raman intensity.[12] In 1977, two groups independently pointed out that the enhanced signal could not be accounted for by the increase of the concentration of scatters. Jeanmaire and Van Duyne tentatively proposed an electromagnetic enhancement mechanism, while Albrecht and Creighton speculated a charge-transfer effect.[13,14] In the electromagnetic mechanism, an enhanced electromagnetic field of the light produced at the surface of the metal under conditions of surface plasmon excitation is proposed to account for the SERS effect.[9,15] In chemical enhancement theory, on the other hand a charge-transfer effect involving the formation of a charge-transfer complex between the metal surface and chemisorbed molecules is believed to be responsible.[9,15]

Despite remaining questions about the exact mechanism, SERS has become into an important surface sensitive spectroscopic technique especially in the context of the observation of extreme high SERS effect up to the single molecular level.[11] A large challenge for the development of SERS effect into a powerful analytical technique, however, is the fabrication of SERS active surfaces with repeatable high enhancement factors. Aside from the improvement of the surface-roughening procedure for fabrication of SERS active metal surface, an improved understanding of the SERS mechanism and recent advances in materials science and nanotechnology provide opportunities to construct novel surface metal structures for SERS research. Strong SERS effects have been observed on novel metal nanostructures such as nanoparticles,[16] nanorods,[17] nanowires,[18] core-shell particles,[19] and others. For example, Nie *et al.* has demonstrated single molecule detection based on the SERS effect of Ag and Au nanoparticles.[20,21]

New surface patterning and fabrication techniques have been applied to generate ordered surface metal nanostructures as SERS active substrates with higher enhancement factors and reproducibility.[22,23] This progress also provides insight into the fundamental mechanism of SERS. While chemical theory plays an important role in rationalizing the Raman enhancement of chemisorbed molecules, electromagnetic theory is now widely accepted as a general theory to understand the SERS effect.[15] In electromagnetic theory, SERS is believed to arise from an enhanced local electric field experienced by adsorbed molecules provided by the surface, which is largely related to the excitation of localized surface plasmons by the incident laser. The most important evidence to support the electromagnetic theory is the existence of a SERS "hot spot". The hot spots are located at the gaps of aggregated metal nanoparticles, where strong plasmon excitation occurs. It follows that the design and fabrication of metal nanoparticle nanostructures with controllable aggregation is critical to understand the SERS mechanism and develop new SERS platforms for analytical applications.[24,25]

Recently, we have reported an easy route to fabricate ordered nanopits on silicon surfaces etched by dilute aqueous HF using poly(styrene)-*block*-poly(4-vinyl pyridine) (PS-*b*-P4VP) as a template. Other than the topologic pattern, the nanopit array has distinct chemical functionality differences at the interior and exterior of the nanopits which can be exploited. The surfaces inside the patterned nanopits terminated by Si-H bond are functionalized by α-ω-alkene-thiol molecules to afford terminal thiol groups on the etch pit surfaces. The resulting thiol surface is used to direct the selective deposition of the nanoparticles through chemical interaction between nanoparticles and the thiol groups. Due to size restriction within the nanopits, a controlled aggregation of

nanoparticles results. The ordered nanoparticle aggregate arrays exhibit a strong SERS effect and could be used for trace chemical analysis.

4.2 Results and Discussion

4.2.1 Fabrication of Nanoparticle Arrays

A scheme of the method used to construct arrays of aggregated nanoparticles using patterned nanopits is outlined in Figure 4.1. As shown in Chapter 2 and Chapter 3, a block copolymer templated etching technique can produce an ordered etch pit array with distinct chemical functionalities at the interior and top of the patterned surface. Figure 4.2 shows a typical SEM image of the patterned template used in this work, which was etched in 0.01% HF (aq) for 50 min followed by removing the coated block copolymer template PS-*b*-P4VP through ultrasonication in toluene for 5 min. The patterned template surface exhibits an array of pseudohexagonal nanopits with the square geometric shape due to the anisotropic etching on Si(100). The depth and width of the pits are ~40 nm and ~80 nm, respectively.

The interior surface of the freshly etched nanopit array was modified with undec-10-ene-1-thiol molecules via a thermally induced hydrosilylation reaction, shown in Figure 4.3a. The formation of a thiol terminated surface was confirmed by the presence of a S 2s peak in the X-ray photoelectron spectrum shown in Figure 4.3b.

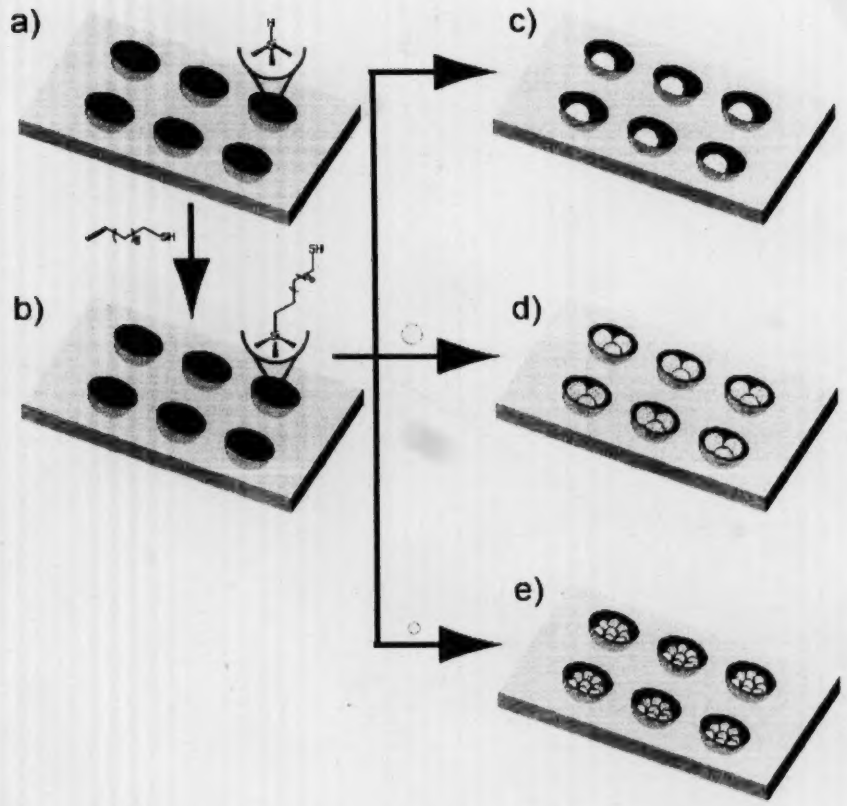

Figure 4.1. Schematic diagram for the fabrication of ordered array of nanoparticle aggregations from the nanopit array on silicon surface. (a) Fresh patterned etch pit array. (b) Thermal hydrosilylation of the fresh patterned surface with undec-10-ene-10-thiol. (c) Deposition of single particle per pit. (d) Deposition of several particles per pit. (e) Deposition of group of particles per pit.

Figure 4.2. An SEM image of etch pit array on a Si(100).

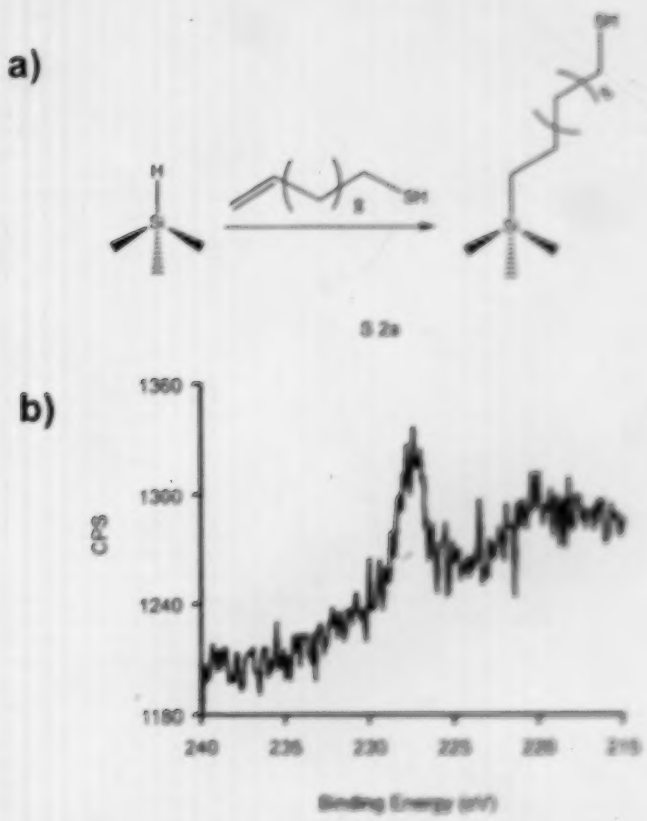

Figure 4.3. (a) Reaction of hydrogen-terminated silicon with mercapto-alkene to generate a thiol terminated surface. (b) High resolution X-ray photoelectron spectrum of a thiol terminated silicon surface showing a S 2s peak.

After reaction with undec-10-ene-1-thiol, the top flat surface of the nanopits is still covered by a native oxide layer, which acts as a resist to the selective deposition of the gold colloid. Immersion of the functionalized substrate into a solution of gold colloidal particles for 24 hours leads to deposition. After the samples are sonicated in water for 20 min, the physically adsorbed nanoparticles on the top flat surfaces of the nanopits array are removed, while the particles immobilized inside the nanopits remain.

As illustrated in Figures 4.1c-e, maintaining the size of the nanopits and varying the size of the gold colloid is expected to result in arrays consisting of a single particle, several particles and groups of particles per etch pit. The three sizes of gold colloids used in this work are 40 nm, 30 nm and 20 nm. (Note: The sizes of nanoparticles measured from SEM images were 40 ± 2 nm, 30 ± 2 nm, and 15 ± 2 nm.) The diameter of the patterned nanopits can be varied from several nm to 100 nm and the depth simultaneously tailored from 5 - 45 nm. Based on a series of experiments, the optimal etched nanopits for gold nanoparticle capture consist of a top-diameter of 80 nm and depth of 40 nm. Figures 4.4a-c show the formation of nanoparticle aggregates in chemically tailored etch pit arrays. Histograms of the number of nanoparticles per etch pit are shown in Figure 4.5. Very few nanoparticles were observed in the etch pits when 50 nm and larger gold colloids were used.

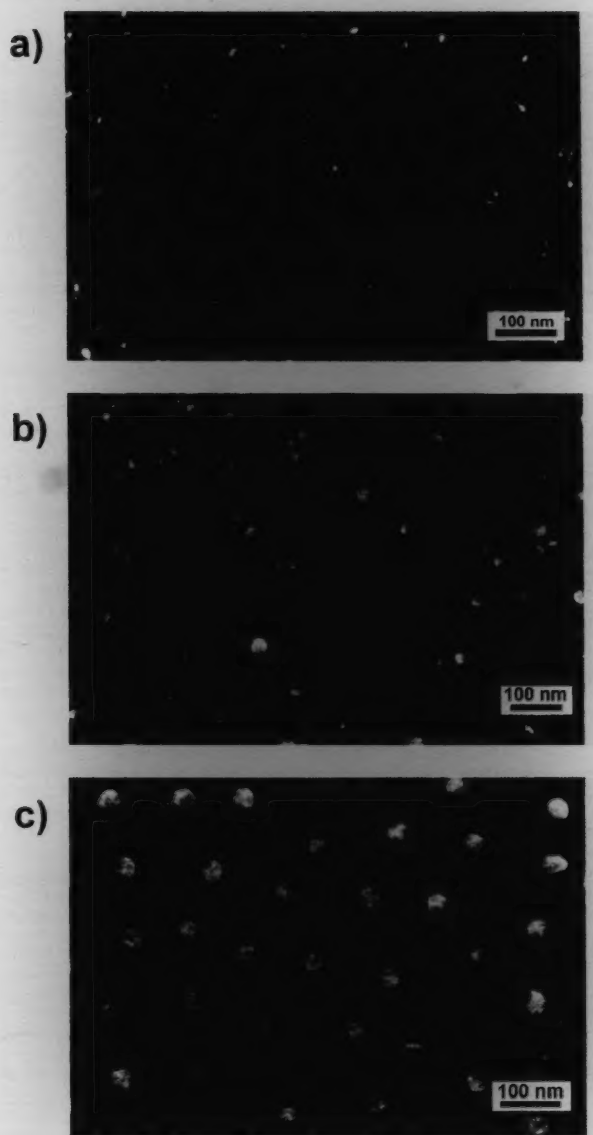

Figure 4.4. SEM images of the aggregations of different size gold colloidal nanoparticles in etch pit array. (a) 20 nm of gold nanoparticles. (b) 30 nm of gold nanoparticles. (c) 40 nm of gold nanoparticles.

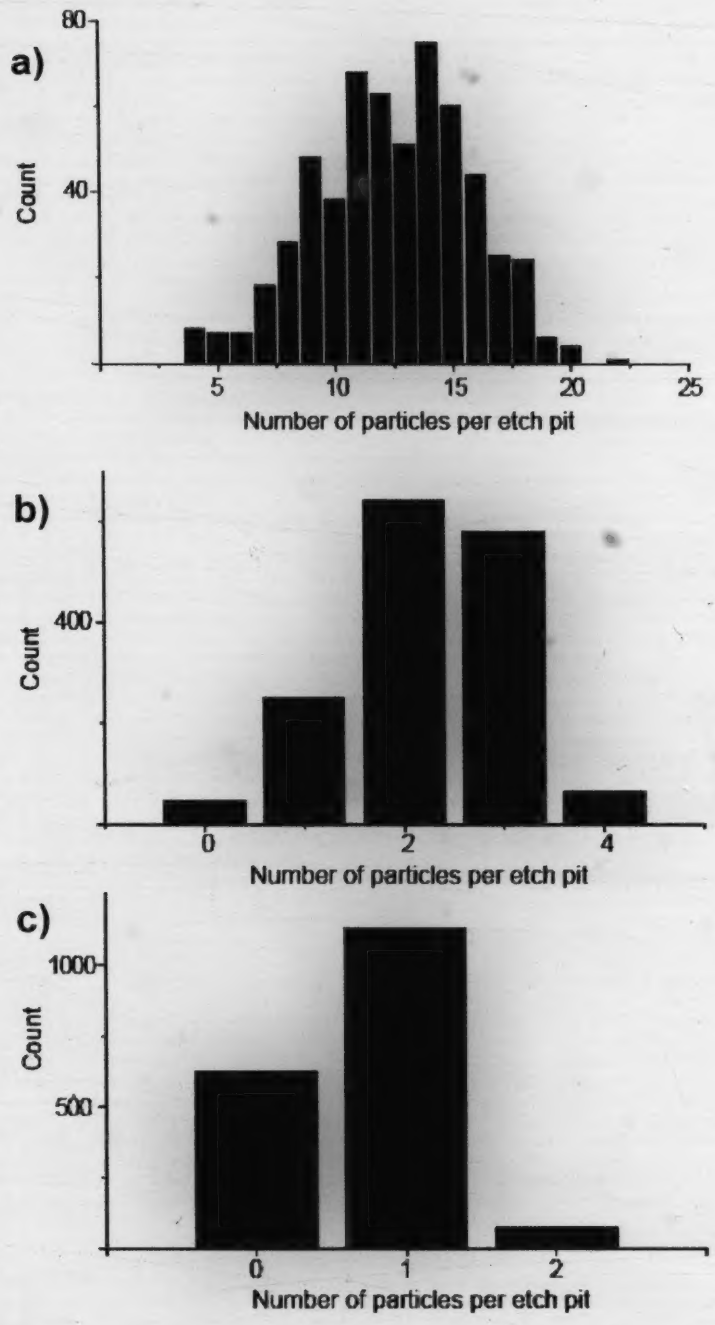

Figure 4.5. Histograms of the number of nanoparticles per etch pit. (a) 20 nm nanoparticles. (b) 30 nm nanoparticles. (c) 40 nm nanoparticles.

4.2.2 SERS Effect of Nanoparticle Arrays

There is intense interest in the fabrication of nanostructures of noble metal nanoparticles due to their unique optoelectronic properties and wide applications in analytical and biochemistry fields. For instance, isolated single noble metal particles and particles aggregates have shown SERS effects for molecules adsorbed on their surfaces, which has promising applications for the ultra-sensitive detection of chemical or biological molecules.[26] Nie and co-workers described a large Raman enhancement from an isolated single metal nanoparticle.[21] In contrast, Moskovits and Jeong reported that metal nanoparticle aggregation is responsible for the SERS effect.[27] Therefore, it is of fundamental interest to investigate the Raman enhancement effect on the patterned nanoparticle arrays with different aggregation behaviours.

To examine the SERS efficiency of the patterned gold particle arrays on the silicon substrate, 4-aminothiophenol (4-ATP) and 4-mercaptobenzoic acid (4-MBA) were used as probe molecules. The SERS spectra of 4-ATP adsorbed on patterned gold particle arrays are shown in Figure 4.6. The spectra were collected using 785 nm laser excitation. To facilitate the comparison of the spectra obtained from different substrates, the spectra were normalized against the 525 cm^{-1} ν(Si-O) vibration mode. Little SERS signal was obtained when using 532 nm laser because gold has less electromagnetic enhancement at 532 nm excitation.[28]

It was found that substrates consisting of 2-3 gold particles per etch pit (with the diameter of 30 nm) exhibited the strongest SERS signals. The spectra are similar to the reported results for 4-ATP on different substrates.[29,30,31,32] As a comparison, the Raman spectrum of 4-ATP in the solid state is shown in Figure 4.7a. The dominant bands

observed around 1080 and 1587 cm^{-1} in the spectra are assigned to C-S and C-C stretching vibrations (a1 vibrational modes), respectively.[29] In contrast to the normal Raman spectrum (Figure 4.7), frequency shift to lower wavenumbers and changes in relative intensity are observed, such as the ν(CS) band shifts from 1086 to 1080 cm^{-1} and the ν(CC) band shift from 1593 to 1587 cm^{-1} (see the band assignments in Table 4.1). The apparent enhancement of the bands around 1435, 1390 and 1143 cm^{-1} are attributed to b2 vibrational modes, which are closely related to thiol group vibrations. The enhancement of b2 mode can be attributed to charge transfer from the metal to the adsorbed molecules, which demonstrate that the 4-ATP molecules are attached to the gold nanoparticles through their sulfur atoms.[31]

Similar results are obtained when 4-MBA molecule was used as Raman probe. Figure 4.8 shows representative SERS spectra of 4-MBA molecules adsorbed on the arrays of gold nanoparticles with different diameters. Again, a nanoparticle array consisting of 2-3 gold particles per pit (with the diameter of 30 nm) shows the best enhancement effect. The dominant features in the spectra are the ν(CS) and ν(CC) ring-breathing modes at 1080 and 1591 cm^{-1}.[17,33] The weak band at 1710 cm^{-1} is from ν(C=O) vibration and indicates carboxylic acid group keeps neutral state when adsorbed on the surface.[34,35] The band assignment of 4-MBA in solid state (Figure 4.7b) and on the nanoparticle array is listed in Table 4.2.

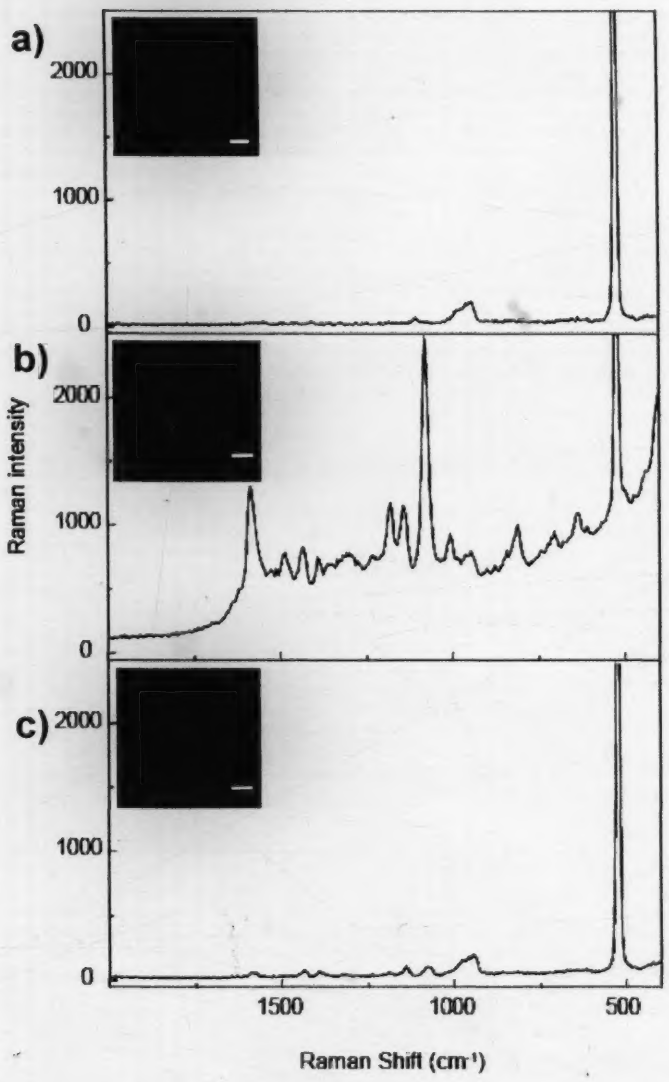

Figure 4.6. Raman spectra of 4-ATP collected on the gold nanoparticle arrays. (a) 20 nm, (b) 30 nm, (c) 40 nm. Inset shows the typical aggregation behaviours of gold nanoparticles in etch pit array. Scale bar is 20 nm.

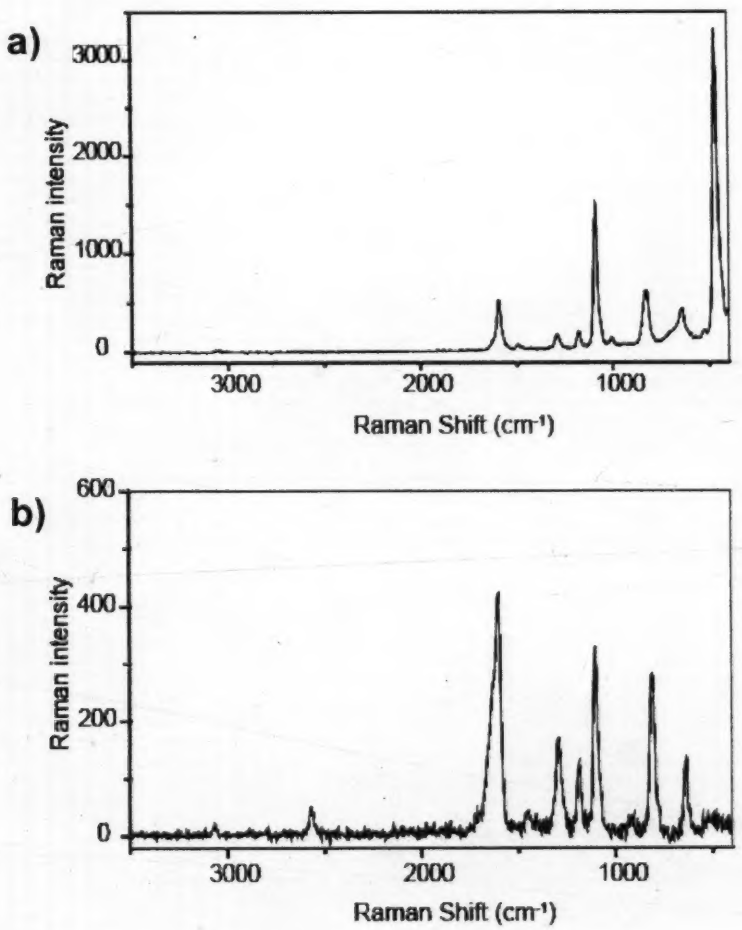

Figure 4.7. Raman spectra of 4-ATP (a) and 4-MBA (b) in solid state. The spectra are collected at 785 nm laser excitation.

Table 4.1. Assignment of Raman vibration modes of 4-ATP in the solid state and on the 30 nm Au nanoparticle array.

Raman shift (cm^{-1})		Assignments[29,30,31]
Solid	Au Nanoparticle	
1593	1587	ν(CC)
1495	1486	ν(CC)+ δ(CH)
1423	1434	ν(CC)+ δ(CH)
	1390	δ(CH)+ ν(CC)
	1307	ν(CC) + δ(CH)
1290		ν(CH)
1176	1180	δ(CH)
1126	1144	δ(CH)
1080	1080	ν(CS)
1005	1008	γ(CCC)+ γ(CC)
827	843	π(CH)
	812	π(CS)+π(CH)+π(CC)
640	638	γ(CCC)
523		γ(CCC)
463		γ(CCC)
391		δ(CS)

ν stretching; δ and γ bending; π wagging

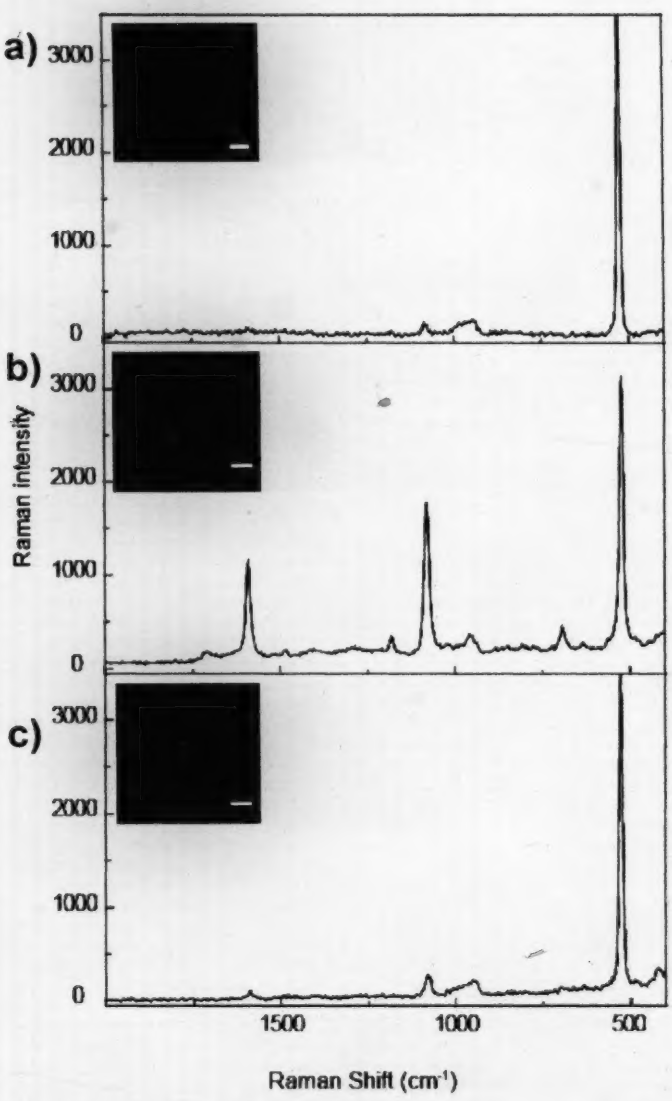

Figure 4.8. Raman spectra of 4-MBA collected on the gold nanoparticle arrays. (a) 20 nm, (b) 30 nm, (c) 40 nm. Inset shows the typical aggregation behaviours of gold nanoparticles in etch pit array. Scale bar is 20 nm.

Table 4.2. Assignment of Raman vibration modes of 4-MBA in the solid state and on the 30 nm Au nanoparticle array.

Raman shift (cm-1) solid	Au nanoparticle	Assignments[4,33]
1704	1708	ν(C=O)
1600	1591	ν(CC) aromatic
1450	1483	νs(COO-)
1292	1286	γ(CH)
1186	1180	δ(CH)
1099	1080	ν(CS)
	958	δ(CH)
812	808	δ(COO-)
	692	γ(CCC)
632	633	γ(CCC)

ν stretching; δ and γ bending; π wagging

When comparing the Raman signal from different nanoparticle arrays, we found that only the array consisting of groups of gold particles with a diameter of 30 nm gave strong SERS signals (see Figures 4.6 and 4.8). It is known from theory and experiment

that the Raman hot spots are located at the interparticle gaps between aggregated metal nanoparticles. A large SERS effect is observed if the interparticle spacing is very close but physically separated. It is widely accepted that the hot spots involving different gold particles distributed on each particles aggregate are responsible for the SERS activity.[9] The substrate consisting of 40 nm single gold particle arrays do not show obvious enhancement, since the single particles are separated too far apart to form effective hot spots. At a particle size of 30 nm, a nanoparticle aggregate is formed with 2-3 nanoparticles in each etch pit. Due to the size restriction effect, effective hot spots are formed in the aggregations, which are responsible for the large SERS enhancement effect. However, there is little SERS enhancement observed on the substrate decorated by groups of gold particles arrays with a diameter of 20 nm. The SEM images in Figure 4.4a show that there are more particles in each pit with 20 nm gold particles than the substrate with 30 nm gold colloids. The absence of enhancement in this substrate can be attributed to a size-dependent SERS enhancement factor. Experimental results obtained by Nie and co-workers reveal that single gold particles with a diameter of 60 nm show the most efficient SERS intensity.[21] They also discovered that if the original particle is not active and "hot" for SERS, then the corresponding aggregates of the particles are also not active for SERS. Our results are consistent with their observations.

To further probe the effect of controlled aggregation, we have done a series of control experiments. Planar SiO_x substrates are functionalized by 3-aminopropyltriethoxysilane molecules to form amino terminated substrate and then were dipped into different sizes of the gold colloid solutions for 40 min. The substrates were taken from the solutions, rinsed by copious amount of Milipore water, sonicated in water

for 20 min and dried by nitrogen. 4-ATP is used as a probe molecule. The SEM images of the substrates with different sizes of gold colloid are shown in Figure 4.9. Most of the gold colloids are isolated on the surfaces. It is noticeable that the nanoparticles are more separated on planar substrates than on patterned etch pit array. Without significant gold nanoparticle aggregation, it is expected that the SERS efficiency on these substrates will be weaker than on those patterned surfaces consisting of particle aggregate arrays.

SERS spectra were collected under the same experimental conditions as previously described, and are shown in Figure 4.10. We can see from the spectra that only the substrates consisting of 30 nm and 40 nm gold colloids show weak SERS signals, and the substrate with 20 nm gold particles has no obvious SERS signal. This indicates that the original isolated 20 nm gold particles are not active for SERS in spite of instances of aggregated gold particles. This supports the result that aggregates of the 20 nm of gold particles in the arrays of etched pits are not active for SERS activity. In comparison, the 30 nm particles exhibit SERS activity, confirming that the array of aggregates of these gold particles would also be SERS active. However, one can see from the weaker SERS spectra of these control substrates that the SERS efficiency on these isolated nanoparticles are much lower than for the aggregated nanoparticles. Finally, 40 nm nanoparticles show similar Raman enhancement on the planar surface and patterned surface because most of nanoparticles stay as isolated nanoparticles on both substrates.

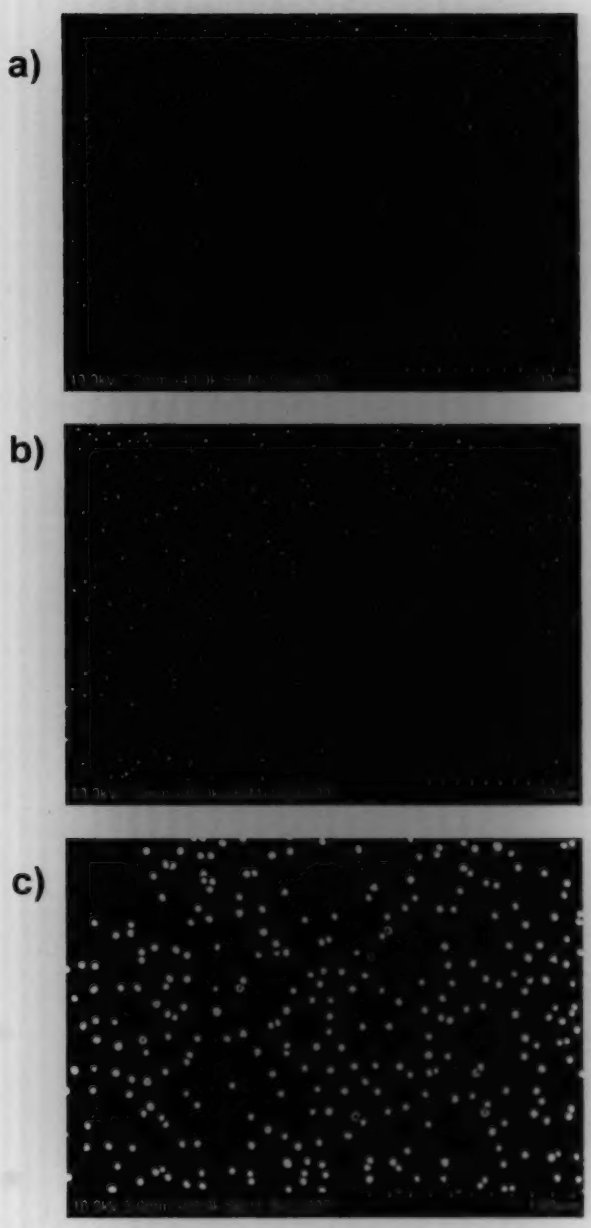

Figure 4.9. SEM images of nanoparticles on Si surfaces modified by 3-aminopropyltriethoxysilane. (a) 20 nm, (b) 30 nm, (c) 40 nm.

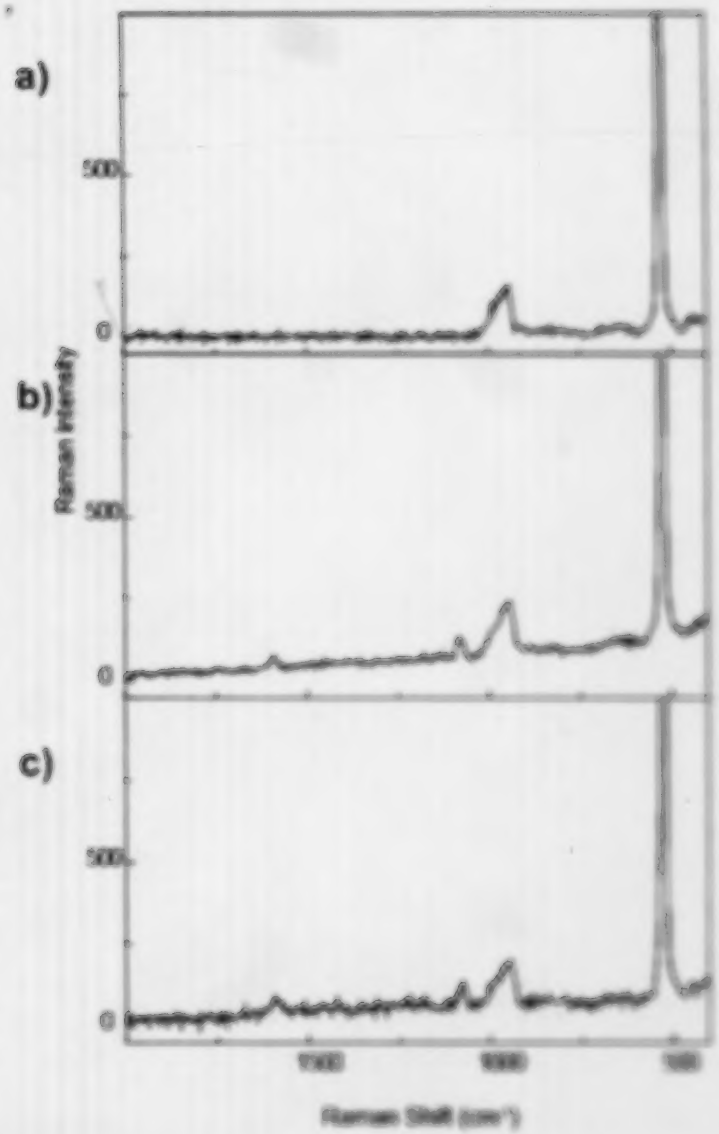

Figure 4.10. Raman spectra of 4-ATP on nanoparticles decorated Si surfaces in Figure 4.9. (a) 20 nm, (b) 30 nm, (c) 40 nm.

4.3 Conclusions

In this chapter, we have shown the fabrication of ordered nanoparticle arrays with different particle aggregations. The distinct surface chemistry of the surrounding walls of nanopits is used to "bind" the nanoparticles exclusively inside the nanopits. The steric restriction imposed by the topological feature of nanopits results in the formation of different aggregations of nanoparticles with different size. The ordered nanoparticle arrays with different particle aggregations exhibit interesting SERS effect. Strong Raman enhancement is observed on the nanoparticle array with 2-3 nanoparticles (with the diameter of 30 nm) in each nanopit, while little Raman enhancement is observed on the nanoparticle array with single particle (with the diameter of 40 nm) per nanopit. The generation of effective Raman hot spots attributed to the observed difference. On the other hand, when the nanoparticle is very small and not active and "hot" for SERS, the corresponding aggregation of the particles are also not active for SERS.

4.4 Experimental Section

Materials and instrumentation. All the gold colloid solutions were purchased from Ted Pella, Inc. and used as received. Mesitylene purchased from Aldrich was distilled under reduced pressure, brought into a nitrogen filled glove box and stored in over 4 Å molecular sieves. Undec-10-ene-1-thiol was synthesized according to the procedure reported in the literature[33] and stored in inert atmosphere. All water (18 MΩ·cm) was filtrated through Barnstead Nanopure water purification system. Hydrofluoric acid (HF, semiconductor grade) was purchased from J. T. Baker. Asymmetric diblock copolymers

of polystyrene-*block*-poly(4-vinylpyridine), denoted through the paper as PS-*b*-P4VP were purchased from Polymer Source Inc. (www.polymersource.com). All glass slides were obtained from Fisher Scientific. 4-Aminothiophenol, 4-mercaptobenzoic acid, 3-aminopropyltriethoxysilane, and 3-mercaptopropyltriethoxysilane were purchased from Sigma-Aldrich Chemical Co. and used as received. All other chemicals and reagents were purchased from Aldrich and used without further purification. All the vibrational experiments (Raman and SERS) were carried out on a Nicolet Almega XR Dispersive Raman Spectrometer (Thermo Fisher Scientific, Waltham, MA) equipped with a CCD detector and an optical microscope with 785 nm excitation laser line. Spectra from the selected area of the sample are recorded at normal incidence in backscattering geometry using a 100× microscope objective. The scattering areas are 1 μm^2. Scanning electron microscopy (SEM) was carried out on a Hitachi S-4800 FE-SEM. XPS was taken on a Kratos Axis 165 X-ray photoelectron spectrometer.

Synthesis of undec-10-ene-1-thiol. Undec-10-ene-1-thiol was synthesized following the literature procedure.[36] First, 0.025 mol of thiourea was dissolved in 100 mL of Ar-purged (40 min) ethanol. Then, 0.010 mol of the 10-undecene-1-bromide was added and the solution heated to reflux for 8-16 h. The reaction was allowed to cool down to room temperature under an Ar purge, and then 10 mL of an aqueous 10% solution (w/w) of NaOH was added. The solution was heated to reflux for approximately 4 h, cooled down to room temperature and then titrated with dilute HCl to pH 7. After extraction with 200 mL of diethyl ether, the organic phase was rinsed three times with Millipore water, dried over anhydrous magnesium sulfate, filtered, and then evaporated under vacuum to yield crude products. The crude liquid was passed through a minicolumn of silica gel to afford

an almost colorless product in 90% yield. ^{1}H-NMR (400 MHz, $CDCl_3$): δ 1.28-1.40 (12H), 1.60 (overlapping signals, 3H), 2.03 (m, 2H), 2.50 (m, 2H), 4.96 (m, 2H), 5.81 (m, 1H).

Silicon wafer preparation. Prime-grade 150 mm diameter p-type Si(100) (6.4-8.0 Ω•cm) wafers were diced by hand into 1 cm^2 square shards. The silicon shards were initially degreased with a common dish soap solution and then cleaned with piranha solution at 80 °C for 30 min (Piranha solution = H_2SO_4: H_2O_2=3:1, v/v. Note: *Piranha solution reacts violently with organics. Special precautions should be made when working with this mixture*). All silicon shards were thoroughly rinsed with Millipore water after each cleaning step and blown dry by a stream of nitrogen prior to use.

Thin films of diblock copolymers. PS-*b*-P4VP (M_n=128400-*b*-33500 g/mol) was dissolved in toluene (HPLC grade) and heated at 70 °C for 45 min to produce a 3 mg/mL solution, and allowed to stand for 24 h prior to use. Thin PS-*b*-P4VP films were prepared by spin-coating the prepared polymer solution, at room temperature, onto the as-cleaned silicon shards in a nitrogen-filled Vacuum Atmospheres glovebox at 2500-3500 rpm.

Fabrication of etch pit arrays. The typical synthetic procedure is as follows. As-prepared silicon shards coated with a monolayer of PS-*b*-P4VP were dipped into the 0.01% HF (aq) solution for the designated time. The shards were then removed from the HF (aq) solution and dried with a stream of nitrogen gas. The block copolymer was then removed by ultrasonication in neat toluene for 5 min, and the ordered etch pits were characterized by SEM.

Nanopatterned surface derivation through thermal hydrosilylation. Thermal hydrosilylation of undec-10-ene-1-thiol on the etched, patterned silicon surface was

carried out by immersing the freshly etched, patterned silicon substrate following polymer removal into a solution of undec-10-ene-1-thiol in mesitylene (v/v=1:3) and heated under argon atmosphere at 200°C for 3 h. The substrate was then removed from the reaction solution, cleaned thoroughly by rinsing with hexane and dichloromethane, and dried with a stream of nitrogen.

Construction of gold nanoparticle arrays with different sizes. In a typical procedure, the silicon shards with the thiol alkane termination inside the etch pits (following thermal hydrosilylation) were immersed into vials of gold colloidal solutions for overnight, in which 10 μL of ethanol was added to increase the wettability of the silicon wafer, separately. The wafers were then removed from the solutions, rinsed thoroughly with Millipore water and ethanol, and then sonicated for 20 min in water to remove the physically adsorbed gold particles from the patterned surface.

Preparation of substrates for control experiments. The control experiment was carried out in the following way. The cleaned substrates were transferred into a desiccator, in which a vial filled with 10 μL of 3-mercaptopropyltriethoxysilane or 3-aminopropyltriethoxysilane was placed. After 40 min, the substrate was removed, rinsed by dichloromethane to remove unbound molecules, and dried by a stream of nitrogen gas. And then they were immersed into gold colloidal solutions for designated time as prescribed in the previous section. The substrates are stored in dichloromethane until needed for analysis.

SERS studies. First, 5 μL ethanolic solutions of 4-ATP or 4-MBA were drop coated onto the substrate surface (1×1 cm^2) decorated with gold colloid arrays and allowed to evaporate in air. Then the substrate was mounted onto a glass slide via double-sided tape.

The Raman spectra were collected on a Nicolet Almega XR Dispersive Raman Spectrometer (Thermo Fisher Scientific, Waltham, MA) equipped with a CCD detector and an optical microscope with 785 nm excitation laser line.

References

1 Alivisatos, A. P. *Science* **1996**, *271*, 933. (a) Brus, L. E. *Appl. Phys. A* **1991**, *53*, 465. (b) Brus L. E. *J. Chem. Phys.* **1983**, *79*, 5566. (c) Weller, H. *Angew. Chem., Int. Ed. Engl.* **1993**, *32*, 41-53. (d) Stucky, G. D.; MacDougall, J. E. *Science* **1990**, *247*, 669. (e) Schmid, G. *Chem. Rev.* **1992**, *92*, 1709. (e) Murphy, C. J.; Sau, T. K.; Gole, A. M.; Orendorff, C. J.; Gao, J.; Gou, L.; Hunyadi, S. E.; Li, T. *J. Phys. Chem. B* **2005**, *109*, 13857.

2 (a) Kagan, C. R.; Murray, C. B.; Nirmal, M; Bawendi, M. G. *Phys. Rev. Lett.* **1996**, *76*, 1517. (b) Magruder, R. H.; Yang, L.; Haglund, R. F. Jr. *Appl. Phys. Lett.* **1993**, *62*, 1730.

3 (a) Elghanian, R.; Storhoff, J. J.; Mucic, R. C.; Letsinger, R. L.; Mirkin, C. A. *Science*, **1997**, *277*, 1078. (b) Storhoff, J. J.; Elghanian, R.; Mucic, R. C.; Mirkin, C. A.; Letsinger, R. L. *J. Am. Chem. Soc.*, **1998**, *120*, 1959.

4 (a) Zheng, J.; Zhu, A.; Chen, H.; Liu, Z. *Langmuir* **2000**, *16*, 4409. (b) Brown, L. O.; Hutchison, J. E. *J. Phys. Chem. B* **2001**, *105*, 8911. (c) Stoeva, S.; Klabunde, K.L.; Sorensen, C. M.; Dragieva, I. *J. Am, Chem. Soc.* **2002**, *124*, 2305-2311.

5 (a) Tien, J.; Terfort, A.; Whitesides, G. M. *Langmuir* **1997**, *13*, 5349-5355. (b) Yonezawa, T.; Onoue, S.; Kunitake, T. *Chem. Lett.* **1998**, 689.

6 Kim, B.; Tripp, S. L.; Wei, A. *J. Am. Chem. Soc.* **2001**, *123*, 7955-7956

7 Yeh, S. R.; Michael, S.; Boris, I. S. *Nature* **1997**, *386*, 57

8 Fan, F.; Stebe, K. J. *Langmuir* **2004**, *20*, 3062

9 Moskovits, M. *J. Raman Spectrosc.* **2005**, *36*, 485.

10 Tian, Z.-Q.; Ren, B.; Wu, D.-Y. *J. Phys. Chem. B.* 2002, *106*, 9463.

11 Nie, S.; Emory, S. R. *Science* **1997**, *275*, 1102.

12 Fleischmann, M.; Hendra, P. J.; McQuillan, A. J. *Chem. Phys. Lett.* **1974**, *26*, 163.

13 Jeanmaire, D. L.; van Duyne, R. P. *J. Electroanal. Chem.* **1977**, *84*, 1.

14 Albrecht, M. G.; Creighton, J. A. *J. Am. Chem. Soc.* **1977**, *99*, 5215.

15 Campion, A.; Kambhampati, P. *Chem. Soc. Rev.* **1998**, *27*, 241.

16 Freeman, R. G.; Grabar, K. C.; Allison, K. J.; Bright, R. M.; Davis, J. A.; Guthrie, A. P.; Hommer, M. B.; Jackson, M. A.; Smith, P. C.; Walter, D. G.; Natan, M. J. *Science*, **1995**, *267*, 1629.

17 Orendorff, C. J.; Gole, A.; Sau, T. K.; Murphy, C. J. *Anal. Chem.* **2005**, *77*, 3261.

18 Jeong, D. H.; Zhang, Y. X.; Moskovits, M. *J. Phys. Chem. B* **2004**, *108*, 12724.

19 Wang,Y.; Chen, H.; Dong, S.; Wang E. *J. Chem. Phys.* **2006**, *125*, 044710.

20 Krug, J. T., II; Wang, G. D.; Emory, S. R.; Nie, S. *J. Am. Chem. Soc.* **1999**, *121*, 9208.

21 (a) Emory, S. R.; Haskins, W. E.; Nie, S. *J. Am. Chem. Soc.* **1998**, *120*, 8009. (b) Nie, S.; Emory, S. R. *Science* **1997**, *275*, 1102.

22 (a) McFarland, A. D.; Young,M. A.; Dieringer, J. A.; Van Duyne, R. P. *J. Phys. Chem. B.*, **2005**, *109*, 11279. (b)Haes, A. J.; Haynes, C. L.; McFarland, A. D.; Zou, S.; Schatz, G. C.; Van Duyne, R. P. *MRS Bulletin*, **2005**, *30*, 368.

23 Mahajan, S.; Abdelsalam, M.; Suguwara, Y.; Cintra, S.; Russell, A.; Baumberg, J.; Bartlett, P. *Phys. Chem. Chem. Phys.*, **2007**, *9*, 104.

24 Qin, L.; Zou, S.; Xue, C.; Atkinson, A.; Schatz, G. C.; Mirkin, C. A. *Proc. Natl. Acad. Sci.* **2006**, *103*, 13300.

25 (a) Jeong, D. H.; Zhang, Y. X.; Moskovits, M. *J. Phys. Chem. B* **2004**, *108*, 12724. (b) Braun, G.; Pavel, I.; Morrill, A. R.; Seferos, D. S.; Bazan, G. C.; Reich, N. O.; Moskovits, M. *J. Am. Chem. Soc.* **2007**, *129*, 7760.

26 Kneipp, K.; Kneipp, H.; Itzkan, I.; Dasari, R. R.; Feld, M. S. *J. Phys: Condens. Matter* **2002**, *14*, R597.

27 Moskovits, M.; Jeong, D. H. *Chem. Phys. Lett.* **2004**, **397**, 91

28 Zeman, E. J.; Schatz, G. C. *J. Phys. Chem.* **1987**, *91*, 634

29 (a) Kim, K.; Yoon, J. K. *J. Phys. Chem. B* **2005**, *109*, 20731. (b) Kim K.; Lee, H. S. *J. Phys. Chem. B* **2005**, *109*, 18929.

30 (a) Zheng, J. W.; Li, X. W.; Ji, Y.; Gu, R. A.; Lu, T. H. *J. Phys. Chem. B* **2002**, *106*, 1019. (b) Zheng, J. W.; Zhou, Y. G.; Li, X. W.; Ji, Y.; Lu, T. H.; Gu, R. A. *Langmuir* **2003**, *19*, 632.

31 Osawa, M.; Matsuda, N.; Yoshi, K.; Uchida, I. *J. Phys. Chem.* 1994, *98*, 12702.

32 Zhu, Z.; Zhu, T.; Liu, Z. *Nanotechnology* **2004**, *15*, 357.

33 Michota, A.; Bukowska, J. *J. Raman Spectrosc.* **2003**, *34*, 21.

34 Talley, C. E.; Jusinski, L.; Hollars, C. W.; Lane, S. M.; Huser, T. *Anal. Chem.* **2004**, *76*, 7064.

35 Schwartzberg, A. M.; Oshiro, T. Y.; Zhang, J. Z.; Huser, T.; Talley, C. E. *Anal. Chem.* **2006**, *78*, 4732.

36 Peanasky, J. S.; McCarley, R. L. *Langmuir* **1998**, *14*, 113.

Chapter 5

Conclusions and Future Work

Fabrication of sub-100 nm pattern on surfaces is an emerging challenge in the development of nanotechnology. Among many newly-developed techniques such as e-beam lithography and scanning probe nanolithography, block copolymer nanolithography stands out as a promising method due to its unique advantages, including compatibility with the existing semiconductor processing techniques, versatile chemical properties, low-cost, and potential for scale up to high throughput production. In this thesis, I have demonstrated a block copolymer-directed silicon surface etching process to produce ordered etch pit arrays on silicon surfaces using a simple aqueous fluoride-based chemical etchant approach. Through modulation of the etching conditions (time, fluoride concentration, silicon wafer orientation, etc.), the shape, size, and morphology of the resulting etch pits can be controlled. Because fluoride etching of silicon results in hydride termination, the etch pit interiors are chemically distinct from the top face of the silicon wafer, rendering it possible to construct functionalized three-dimensional nanostructures on the wafer. As one of many possibilities, the gold nanoparticle array with different aggregation behaviour is built up by tailoring the chemical functionality of etch pit array. The gold nanoparticle aggregates show interesting Raman enhancement effects and can be used for chemical analysis based on surface enhanced Raman scattering (SERS) effects. The main conclusions are listed below.

In Chapter 2, block copolymer self-assembly templated nanoscale etching of silicon is demonstrated to produce three-dimensional nanoscale features with controllable

shapes, sizes, average spacing, and chemical functionalization. The self-assembled PS-*b*-P4VP copolymer micelle array is used as a template. The distinct chemical properties of the two blocks are used to direct the standard fluoride based etchant to etch the silicon surface and produce ordered etch pit arrays. The block copolymers serve to direct the silicon surface chemistry by controlling both the spatial location of the reaction as well as the concentration of reagents. Anisotropic etching is observed on silicon wafers with different crystallographic orientations and is attributed to protonated polyvinylpridinium fluoride as the active etchant. It has also been shown that block copolymer templated etching is applicable to non-planar surfaces as long as the copolymer template can conformally coat the surface.

In Chapter 3, the chemical functionalities of etch pit arrays are characterized. Fluoride etching of silicon results in hydride termination at the interiors of the etch pits, which are chemically distinct from the top face of the silicon wafer. The different chemical functionalities of the interior and exterior of the etch pits are established by galvanic displacement and silicon surface hydrosilylation reactions. The controllable placement of gold nanoparticles at the interior and/or exterior of etch pits is achieved. By employing proper surface chemistry, the fabrication of metal nanocrystal arrays by direct growth from the etch pits or by capturing Ag nanoprisms within functionalized etch pits is demonstrated.

In Chapter 4, gold nanoparticle arrays with controlled aggregations are fabricated by utilizing the topological and chemical characteristics of the etch pit arrays obtained by the block copolymer templated etching process. By selectively functionalizing the interiors of the etch pits with organic monolayers, the nanoparticles can be selectively

captured within the etch pits. The nanoparticles form different aggregations depending on the particle size and etch pit diameter due to the size restriction effect. The different nanoparticle aggregations exhibit interesting surface Raman enhancement effects. The highest enhancement factor is observed for the 30 nm nanoparticle aggregations with 2-3 nanoparticles per etch pit, which could be explained by the formation of effective Raman "hot-spots". The controlled nanoparticle aggregation arrays provide new routes for designing SERS substrate for chemical analysis application.

Block copolymer nanolithography has grown rapidly in the past decade. The ability to interface this method with conventional semiconductor processing techniques makes it promising in terms of incorporation into future device fabrication procedures. The fabrication of important semiconductor device units such as capacitors and field effect transistors using block copolymer nanolithography has been demonstrated.[1,2,3] In 2003, IBM announced its intention to utilize self-assembled block copolymers that form quasi-hexagonal close-packed templates for the manufacture of floating silicon gates for flash memory. One typical process in block copolymer nanolithography is using ordered copolymer assemblies as physical masks to produce surface patterns. For example, one of the components in block copolymers can be selectively removed or doped with heavy elements to improve the contrast for the subsequent dry etching step to transfer the pattern into underlying substrate. An alternative approach is to take advantage of the difference in chemical properties of the components in block copolymers to induce localized chemical adsorption or reaction to fabricate surface patterns. For example, metal oxide nanoparticles arrays and metal nanoparticle arrays have been fabricated on the basis of the local chemical reaction of one component of the block copolymer

assembly.[4,5] In the present work, we have used the chemical affinity of poly(4-vinylprydine) to HF etchant to deliver this chemical etching agent to Si surfaces, to form ordered etch pit arrays. This copolymer assembly directed surface chemistry has been previously demonstrated by our group for the fabrication of a variety of metal nanoparticles on semiconductors surfaces.[6] The interface of block copolymer nanolithography with well-established surface chemistries provides great opportunity for the development of sub-100 nm surface patterning techniques. For example, it is of great interest to develop a suitable block copolymer template able to mask the self-assembly of organic molecules on surfaces. The development of block copolymer templated surface chemistry nanolithography is expected to provide high resolution, close to that of scanning probe nanolithography, and high throughput, as in soft lithography.

The formation of ordered copolymer assemblies is a prerequisite for block copolymer nanolithography studies. In many cases the rich information provided by solid state copolymer phase diagrams is informative for achieving the desired patterns. On the other hand, copolymers can self-assemble into a variety of structures in solution, and these structures can be transferred onto substrates to provide the template for nanolithography. In the present study, self-assembled micellar arrays with quasi-hexagonal patterns formed from the solution phase are used as templates for etching processes. We have also attempted to extend the same patterning processes to other copolymer patterns. Figure 5.1 shows an etched surface pattern using polystyrene-*block*-poly(2-vinylpyridine)-*block*-poly(ethylene oxide) (PS-*b*-P2VP-*b*-PEO) triblock copolymer assembly. The core-shell-corona micelle of PS-*b*-P2VP-*b*-PEO triblock copolymer in water is formed by the crew-cut method.[7,8] After dipping the Si wafer

coated with triblock copolymer film into 1% HF (aq) for 10 min, the worm-like structures mirroring that of triblock polymer rod micelles are obtained. By tuning the morphology of block copolymer assemblies, other surface pattern structures are accessible. As demonstrated in the present work, HF etchant can pass through the hydrophilic P4VP core of the PS-*b*-P4VP assemblies to produce etch pit arrays. On the other hand, nanopillar arrays would be expected if a copolymer assembly with a hydrophilic corona and a hydrophobic core were used as template to direct the etching process. Furthermore, interfacing block copolymer assemblies with top-down lithography techniques to improve the orderliness of copolymer patterns is also of great interest for future investigation.

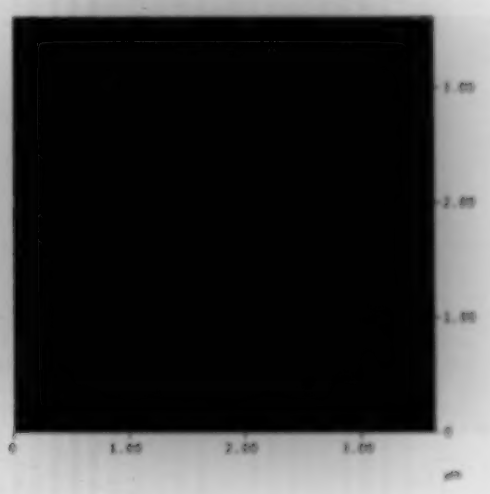

Figure 5.1. Block copolymer templated etching on Si using self-assembled PS-*b*-P2VP-*b*-PEO as a template.

Although we used silicon as a substrate in the present work, block copolymer templated etching could almost certainly be extended to other substrates. The ordered etch pit arrays have been successfully obtained on GaAs substrates using HCl as an

etchant (Figure 5.2). The formation of textured patterns on alternative substrates would be of interest for field emission devices, photovoltaic devices, and light emitting diode applications. In addition, it is possible to develop new patterned structures using properly designed substrates. For example, by employing silicon on insulator (SOI) wafers, perforated membranes can be fabricated using the block copolymer templated etching process, as schematically shown in Figure 5.3. First, polystyrene-block-poly(4-vinylpyridine) (PS-b-P4VP) micelle arrays are spin-coated on the SOI substrate. After dipping the polymer coated wafer into HF solution, fluoride etchant is expected to pass through the P4VP part of the copolymer film, and selectively etch away Si to form an etch pit array. When HF breaks through silicon layer, it will quickly etch away the SiO_2 insulator layer, forming a free-standing perforated Si membrane.

Figure 5.2. Formation of etch pit array on GaAs using block copolymer templated etching. Scan size: 2 μm ×2 μm (Left) and 1 μm ×1 μm (Right).

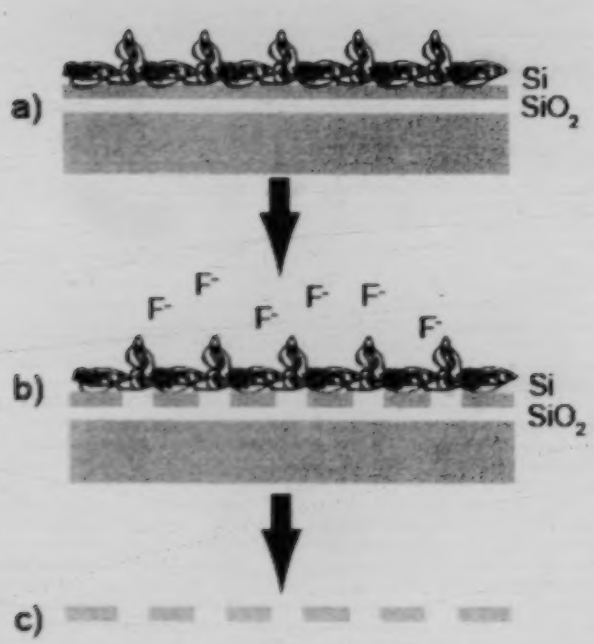

Figure 5.3. Proposed procedure for the fabrication of a free-standing Si membrane using block copolymer templated etching on silicon-on-insulator (SOI) wafer. (a) Block copolymer PS-*b*-P4VP coated SOI wafer. (b) Dipping the wafer into HF solution. (c) The formation of a perforated Si membrane.

One of the unique features of the etch pit array obtained by block copolymer templated etching is the difference in chemical functionality at the interior and exterior of etch pits. The interior walls of the etch pits are hydride-terminated due to the HF etching, while the flat top surface of exteriors remains covered by native oxide. This difference in chemical functionality allows orthogonal chemistry on the patterned surface for the construction of sophisticated nanostructures. We have demonstrated the ability to control the position of nanoparticle inside and/or outside of etch pits by tailoring the surface chemistry of the arrays in Chapter 3. In addition, by taking advantage of the chemical functionality and topological feature of the etch pits, we have successfully fabricated

nanoparticle arrays with controllable aggregation behaviours for SERS application in Chapter 4. Ordered etch pits arrays are predicted to function as isolated nanoreactors for many applications such as biological analysis, catalysis, and electronic devices.

Another interesting subject to explore will be the use of different aggregations of the metal nanoparticles to investigate SERS effect. In chapter 4, we demonstrated that different sizes of gold nanoparticle arrays with controlled aggregations exhibit interesting surface Raman enhancement effects. The substrates consisting of a single particle (40 nm), several particles (30 nm) and groups of particles (20 nm) per etch pit show apparently different SERS effects. The substrate decorated by 30 nm gold particles had the strongest SERS signal, which was attributed to the formation of the effective aggregation in the etch pits. To exclude the effect of the particle size on the SERS enhancement factor and further investigate the different aggregation behaviours on SERS effect, we propose here to study the SERS effect of the arrays of the same size of gold nanoparticles with different aggregation behaviours. If we could fabricate the substrates consisting of a single particle, several particles and groups of particles per pit from the same size of gold nanoparticles, it would clearly prove the effect of hot-spots existed between the aggregated nanoparticles on SERS effects.

The formation of arrays of different aggregation gold nanoparticles on patterned etch pit substrates was determined by the particle size and etch pit diameter due to the size restriction effect. By maintaining size of gold particles and changing the size of the etch pits, it might be feasible to fabricate the arrays of the same size of gold nanoparticles with different aggregation behaviours. The challenge for this approach is to control the size of the etch pits so that it can match well with that of gold nanoparticles. Based on

the results shown in Chapter 2, the size of the etch pits and their inter-distance can be controlled by adjusting the etching time and the copolymer molecular weight, respectively. In addition, the filling efficiency of nanoparticles in the etch pits is expected to be improved by tailoring the surface functionalities inside the etch pits and that on the nanoparticle protecting ligands.

In summary, we have demonstrated a simple process to obtain sub-100 nm etch pit arrays using block copolymer templated etching. The unique chemical functionality of these etch pit arrays is both established and utilized for the fabrication of metal nanoparticle array exhibiting interesting Raman enhancement effects. This combination of block copolymer nanolithography and surface chemistry could provide new opportunity to design and fabricate nanopatterns with novel properties and structures.

References

1 Black, C. T. *Appl. Phys. Lett.* **2005**, *87*, 163116.

2 Black, C. T.; Guarini, K. W.; Milkove, K. R.; Baker, S. M.; Russell, T. P.; Tuominen, M. T. *Appl. Phys. Lett.* **2001**, *79*, 409.

3 Guarini, K. W.; Black, C. T.; Zhang, Y.; Kim, H.; Sikorski, E. M.; Babich, I. V. *J. Vac. Sci. Technol. B* **2002**, *20*, 2788.

4 Glass, R.; Moller, M.; Spatz, J. P. *Nanotechnology* **2003**, *14*, 1153.

5 Kim, D. H.; Kim, S. H.; Lavery, K.; Russell, T. P. *Nano Lett.* **2004**, *4*, 1841

6 Aizawa, M.; Buriak, J. M. *J. Am. Chem. Soc.* **2005**, *127*, 8932. (b) Aizawa, M.; Buriak, J. M. *Chem. Mater.* **2007**, *19*, 5090.

7 Aizawa, M.; Buriak, J. M. *J. Am. Chem. Soc.* **2006**, *128*, 5877.

8 Lei, L.; Gohy, J.-F.; Willet, N.; Zhang, J.-X.; Varshney, S.; Jerome, R. *Macromolecules* **2004**, *37*, 1089.